INVESTIGATION OF ELECTRONIC PROPERTIES OF HIGH PURITY SYNTHETIC SINGLE CRYSTAL TYPE IIA DIAMOND FOR ELECTRONIC APPLICATIONS

By

A.M.O.D da Costa

A thesis submitted to the Faculty of Science, University of the Witwatersrand, Johannesburg, in fulfilment of the requirements for the degree of Doctor of Philosophy

Declaration

I declare that this thesis is my own unaided work. It is being submitted for the degree of Doctor of Philosophy in the University of the Witwatersrand, Johannesburg. It has not been submitted before for any degree or examination in any other University.

_____

(Signature of candidate)

_____day of_____2007____

Abstract

A range of different high-quality single crystal diamonds synthesized under high pressure and high temperature (HPHT) conditions have been studied in view of their potential as candidates for specialized electronic devices with emphasis on particle detectors. The studies incorporated a long range of spectroscopic and electronic characterization techniques.

Special attention was given to electronic properties and device performance related to the electrical contacts applied, the type and the concentration of impurities and the crystallographic defects present. The electronic response of a diamond detector as far as impurities are concerned is predominantly determined by the single substitutional nitrogen (SSN) and boron acceptors. Different techniques were used to assess the role of such impurities in the diamond crystals studied, as well as to study the dynamics due to the interaction of such impurities with each other (compensation). Hence, *the electron spin resonance* (ESR) and the *current-deep level transient spectroscopy* (I-DLTS) techniques were used in this respect to extract the information concerning activation energies, nitrogen-boron dynamics, and the nitrogen and boron concentrations.

It was found that the SSN content was below 10^{13} cm^{-3} with this result giving the approximate concentration of boron acceptors, being the same value as of that of the SSN, or slightly above. Maximum activation energies of boron acceptors were extracted from three different regions in the bulk of the diamond. The values were approximately 0.311 eV $\pm$ 0.0027 eV in the center region, 0.308 eV $\pm$ 0.007 eV in the intermediate region and 0.29 eV $\pm$ 0.007 eV at the edge region, respectively. The maximum activation energy when boron is fully compensated is about 0.37 eV.

Properties of ohmic and Schottky contacts as a function of concentration of SSN and boron acceptors were investigated using Current-Voltage characteristic and photo-current measurements. Different surface treatment conditions and different types of diamonds (IIa, IIb and Ib) were used.

Electronic properties as a function of contacts were assessed for high purity synthetic type IIa diamond detector, incorporating a time of flight (TOF) UV laser set-up. The maximum hole collection distance at room temperature was found to be 91.00 cm, the maximum transient time for holes was about 1.00 ms and the efficiency was approximately 41%, with contacts made of Ti/Pt/Au-Ru. When Ru-Ru contacts are applied, the maximum hole mobility and the velocity were extracted at room temperature to be about 17963.44 $cm^2V^{-1}s^{-1}$ and 5.02 $\times 10^7$ cms^{-1}, respectively, and the efficiency of the device is about 30%. The maximum applied external electric fields with Ru-Ru contacts were increased to about 1.32 times that at low temperature and to about 1.84 times that at room temperature.

Large signals generated by α-particles from ^{228}Th were obtained without using amplification. However, a full analysis of the pulse was not possible due to the narrow bandwidth of the electronic probes used.

In a detector made of type Ib diamond, with SSN concentrations of about 50 ppm, it was found that regions in the bulk exhibiting better charge collection properties contained small concentrations of uncompensated boron impurity. On the other hand, the difference in the concentrations of SSN between the two type Ib diamonds, with about 50 ppm and about 200 ppm of SSN concentrations, respectively, resulted in approximately 70 ps difference in the transit time between two detectors made of these diamonds.

Keywords:

Synthetic diamond, detector, HPHT, type Ib, type IIa, single substitutional nitrogen, SSN, ESR, ARP, I-DLTS, metallization, uncompensated boron impurity, crystallographic defects, rise and decay times, charge carrier life time, charge carrier mobility, carrier mean free path , charge collection distance, carrier Schubweg.

To my parents and to my sisters

Acknowledgements

I am highly indebted to my mentor the late Professor J.P.F. Sellschop who proposed the project and also provided the necessary diamond used in this research program. He supported the project with extraordinary enthusiasm and energy. His last recommendation when he provided the ultra pure HPHT diamond was; "Get the best of it!".

I would also like to thank the Faculty of Science, specially to the Dean of the Faculty of Science Professor R. Bharuth-Ram for removing all obstacles encountered during the work. To the School of Physics of the University of Witwatersrand for their financial and moral support, to the National Research Foundation (NRF) for their generous support. In addition, I am very grateful to the Jülich Funding Institution and the German government for having provided the financial support towards the living costs during my visit to GSI Laboratory.

I am indebted to the Head of School of Physics Professor J. Rodrigues, to the Deputy Head of the school, Professor J. Carter, and to Professor B. Cole the Former Head of School of Physics for their relentless support particularly during the most difficult and trying times of my studies.

I am grateful to my supervisor, Professor E. Sideras-Haddad, for making it possible to bring the work to the end and for his relentless support.

To the academic team of the Department of Physics of the University of Pretoria, Professor D. F. Auret, Professor M. Hayes and Dr. W. E. Mayer for having provided critical scientific guidance and contribution towards solving crucial technological and semiconductor physics problems, without their involvement this study would not have been completed.

To Professor P. Kienle the founding member of the German-SA collaboration (2001-2004).

To iThemba LABS National Facility for allowing me to use the facilities, especially to Dr. I. Machi who took the responsibility for the completion of the vacuum

chamber, an essential component of the research and for providing transportation for experiments outside Johannesburg. Many thanks to Professor J. Sharpey-Schafer (then Director of iThemba LABS), Professor K. Bharuth-Ram Dr. J. Lawrie, Dr. S. Förtsch, for providing very important support and accommodating experiments. To the staff members of iThemba Labs Gauteng especially to Doris Monyamane and to Sam Masala, to the Electronic Lab and to the Mechanical Workshop for moral support, to Christine Thinane from of School of physics and to all collegues I met during the research.

To the National Laser center at CSIR in Pretoria, for allowing the use of facilities and assisting with the experiments. Special thanks to T. Duplooy, Dr. A. Forbes and Dr. H. Human.

I had the pleasure to meet Dr. Helmuth Spieler at LBNL and I value his support and invitation to work with the ATLAS group for three months at the Lawrence Berkeley National Laboratory in the U.S.A., in 2001.

I would like to thank Dr. C. E. Nebel, for having shared his knowledge in the research area, during my short visit to his laboratory in the Technical University of München, in 2002.

A special thank to the late Dr. H. J. Sann, from GSI laboratory, who provided his personal electronic module that helped to generate the best signals from the diamond detector, and for introducing me to the "Meca" of physics, the CERN Laboratory, in 2002.

To the one of the best electronic engineers I have met, Mercea Cioubanu, from GSI Laboratory in Germany, for having provided the best operating electronic conditions and for been opened to valuable didactic discussions, and to all whom I have worked with at GSI Laboratory, from 2002 up to 2004.

To the Mellon Foundation for providing me with a scholarship since 2002 up to 2006.

To N. Makau and G. Amolo for all the help and moral support.

Last but not least, I feel indebted to my parents and sisters for being there at all times and for their uncritical support.

Johannesburg, South Africa — Ana Maria Odete Dabula da Costa
September, 2007

Contents

List of Figures

List of Tables

Chapter 1

Introduction

Diamond is a wide band gap material with exceptional and extreme properties such as high thermal conductivity, large Debye temperature, large Moh scale of hardness, large atomic density and high refractive index. The properties of this material are exploited in the development of heat sink products, cutting tools and are applied on the perforators, employed in the mining and oil industries. Due to its refractive index, the highest compared to the other materials, diamond has enjoyed extreme appreciation in the jewellery industry.

Diamond is transparent to electromagnetic radiation over a large spectral range (from 180 nm in the UV to 100 μm in the far infrared). It has an exceptional role to play in optical technology [1]. It could be applied in windows for IR thermal imaging for 'dual band' (Visible/IR) systems. It can be used in applications such as optical windows or mirrors for high-power lasers, free-electron lasers and for X-ray synchrotron radiation. Single crystal diamond of high purity with high integrity of crystalline structure and a small amount of crystallographic defects has been investigated as excellent candidate as monochromator in X-ray optics [2].

Diamond contains other excellent properties that renders it an excellent candidate for electronic applications. These properties are the wide band gap, very low dielectric constant, small atomic number, high resistivity, radiation hardness and long radiation length of about 121 mm. The wide band gap in diamond is responsible for the high break down field and low intrinsic carrier concentration, about $1e\ \mathrm{km}^{-3}$, at room temperatures [3, 4]. On the other hand, low dielectric constant in diamond is responsible for low capacitance, resulting in a very short rise time for electronic devices made of this material. High thermal conductivity in diamond results from fast relaxation times of acoustic phonons, which leads to a low power dissipation during the operation of an electronic device made of this material [5]. Fast relaxation times of acoustic phonons also implies fast injection of charge carriers generated when the crystal interacts with a strong electromagnetic wave.

There are certain advantages using diamond, a material with wide band gap, as a semiconductor compared to other semiconducting materials such as silicon with a small band gap. An electronic device made of diamond operates at high fields and temperatures whereas silicon based devices experience crystal damage when operated above room temperature due to increased diffusion of impurities in the crystal. The large dielectric constant and consequently large capacitance of silicon-based devices, in contrast to diamond, increase the time response of such electronic device. However, the charge collection properties are several times higher in silicon compared to diamond.

Table 1.1: Properties of diamond [6]

Properties	Units	Silicon	Type IIa natural diamond
Atomic mass		28	12
Atomic number		14	6
Inter-atomic distance	Å	2.2	1.54
Lattice constant	Å	5.4	3.56
Mass density	[g cm^{-3}]	2.32	3.52
Material hardness	[Moh scale]		10
Refractive index			2.419
Melting point			4363
Debye temperature	[K]	645	1860
Dielectric constant		12	5.7
Band gap	[eV]	1.12	5.46
Frequency	[Hz]	10^{14}	10^{15}
Wave length transmittance lower cut-off	[nm]	107	220
Resistivity	[Ωcm]	$20{,}5\times10^{3}$	$\geq10^{15}$
Breakdown field	[V cm^{-1}]	3×10^{5}	1.0×10^{7}
Electron mobility	$cm^2V^{-1}s^{-1}$]	1450	1500,2400
Hole mobility	[$cm^2V^{-1}s^{-1}$]	450	1000,2100
Electron saturation velocity	[cm s^{-1}]	1.0×10^{7}	2.0×10^{7}
Hole saturation velocity	[cm s^{-1}]	9.0×10^{6}	10^{7}
Thermal conductivity	[W$cm^{-1}K^{-1}$]	1.4	20...23
Energy to create an electron-hole pair	[eV]	3.6	13
Radiation length	[cm]	9.4	12.4
Specific ionization loss	[MeV cm^{-1}]	3.9	6.2
Number of e-h pair/mip	[pairsμm^{-1}]	90	36
Radiation hardness	[particles cm^{-2}]	10^{15}	10^{15}

Diamond is classified as type Ia, Ib, IIa and IIb according to the type of impurities and their concentrations in the material [3, 4, 7]. The most important impurities, present in all types of diamonds, are the single substitutional nitrogen (SSN) donors and the boron acceptors, due to high percentages found in the environment, compared to other impurities. The above classification is related to the proportion in the concentrations of these two major impurities in relation to each other or to other impurities. In addition the classification of types Ib, IIb and IIa diamonds depends also in the compensation factor of SSN and boron impurities.

In general, the concept of compensation in diamond refers to the suppression of effect of boron acceptors, which occurs only if the concentration of SSN donor is slightly above the concentration of boron acceptors. This form of compensation is most effective, especially for particle detector applications using diamond. Other known forms of compensation of boron acceptors are achieved by implanting hydrogen or by electron irradiation.

A type Ia diamond contains a high percentage of nitrogen in aggregate form, and is characterized by absorption of UV and IR light. This type of diamond exhibits a light yellow colour [1, 8].

A type Ib diamond is a highly resistive material and contains considerable concentrations of SSN in a non compensated form. This material absorbs IR and UV light. The presence of SSN is responsible for the yellow colour of the diamond [1, 8].

A type IIb diamond is a semi-conducting material due to the presence of considerable

concentrations of boron acceptors in non compensated form. Boron impurity is responsible for the bluish colour of this type of material [1, 8].

A type IIa diamond contains extremely low concentrations of boron acceptors and SSN, being both compensated. The compensation of both impurities, at very low concentrations, is responsible for the transparent nature of the diamond. This type of diamond shows a high coefficient of transmittance of UV light compared to other types of diamond [1, 8].

The good performance of an electronic device made of diamond, such as a particle detectors and dosimeters, depends mainly on a very low concentration of impurities and perfect crystallographic structure. Such electronic devices made of this material have been investigated over the last 30 years using natural diamonds [3]. However, these efforts did not produce satisfactory results. The reason lies on the fact that even the best natural diamonds contain a high density of impurity and defects, which are the main cause of poor performance of such devices.

A review article in reference [9] illustrates the progress in development of synthetic diamonds. Synthetic diamonds for electronic applications, with controlled concentrations of impurities and density of crystallographic defects, have been synthesized over the past 50 years, starting successfully with high pressure and high temperature (HPHT) processes. This has been achieved by several companies mainly in Japan, Europe and U.S.A [9]. Synthetic diamonds have found applications as heat sinks in the electronic industry. Another method of synthesizing diamond is based on the

chemical vapour deposition (CVD) technique developed by Union Carbide Corporation in 1950 [9] and improved greatly over the past twenty years. Investigations on the electronic applications of natural and synthetic diamonds have been reported by several authors [4, 10, 11].

Until recently, however, artificial diamonds synthesized using the CVD method were of polycrystalline nature. The quality of the materials for electronic applications were improved by producing synthetic CVD diamonds, in which the crystalline grains are of unidirectional orientation [12]. Due to the improved electronic properties of these materials, particle detectors and tracking devices made of these materials were investigated using charged particles with energies up to several GeV's [11, 13].

Recent developments in the synthesis technology using CVD and HPHT methods by Sumitomo and De Beers have achieved a production of high-quality synthetic single crystal type IIa diamond. The crystals developed by both methods are characterized by highly reduced concentrations of the most important impurities such as the SSN and boron acceptors. These impurities constitute a challenging problem in the synthesis technology due to their presence in the synthesis environment.

The crystals synthesized by both methods are also of highly reduced crystallographic defects compared to natural single crystal type IIa diamond [14, 15]. Several authors have presented satisfactory results of electronic applications of these materials, such as in particle detection application and the first results were presented in Refs. [2, 14, 16]. Recent developments in CVD and HPHT synthesis methods produced synthetic type IIa diamonds with extremely small concentrations of SSN and boron

impurities. In such specimens both type of impurities are not compensated, which result in an increment in the conductivity of these materials. Specimens synthesized recently using an improved HPHT method, contain even smaller concentrations of both impurities and the SSN is found to be below 10 parts per billion (ppb). Therefore, in the type IIa specimens synthesised using the HPHT method there is many times more conductivity compared to the type IIa specimen synthesised using CVD method. The increment in the conductivity in type IIa HPHT diamond results from much lower compensating factor between the SSN impurity and boron acceptors. It is known that SSN and born impurities compensates only when the concentration of SSN is above that of boron impurity as detailed in Ref. [17]. This means that even if both impurities are found below 10 ppb the diamond will remain conductive.

It is known from silicon-based electronic devices, that 10^{12} atoms of boron per cm^3 of silicon, which represents $1/10^{10}$ atoms per cm^3 in the lattice of silicon, will increase the conductivity of this material [18]. Carbon belongs to the same chemical group as that of silicon and the diamond form of carbon contain more atoms per cm^3 in the lattice compared to silicon. Therefore, the same value of boron in diamond, as in the case of silicon, will also increase the conductivity of diamond. Such diamond can be classified as weak p-type semiconducting material.

The present work investigates the spectroscopic and electronic properties of synthetic single crystals type IIa HPHT diamond. In this material the real concentration of SSN and boron acceptors are below the detectable sensitivity of any spectroscopy

available. However, as explained above the material is conductive.

The relationship between time and charge collection properties with concentrations of SSN is also investigated using type Ib synthetic diamonds with different concentrations of SSN.

The challenge in this work lies on the improvement of the electronic response of detectors made of synthetic type IIa HPHT diamond, which exhibits weak p-type semiconductivity [20]. The difficulties in this investigation concerns the fact that although the concentrations of the impurities are exceptionally low, the conductivity of the diamond is relatively considerable. The parameters to be improved are the applied external electric field in a detector made of this material, charge carrier mobility, charge collection properties, time response and pulse height. By reducing the effects of leakage current, it will result in improvement of some of the above properties. In this respect, improved contact technology plays an important role in facilitating diamond-based particle detector and special attention was given in this regard in the present study.

Passivation of the surface or of the near surface region, using hydrogen plasma, in order to increase the resistivity of the device the properties of the contacts were investigated using a semiconducting diamond with very high concentrations of boron impurity. The properties of contacts made in this way were investigated by measuring the Current-Voltage (I-V) characteristic and the effect of radiation in the Current-Voltage characteristic. On the other hand, the properties of an inert metal with a high work function and its combination with other metals in the performance

of a detector device were explored.

Ultraviolet photons with an energy just above the band gap of the diamond were used in order to characterize the electronic properties of the contacts applied. The results extracted from this characterization were the charge carrier density, the resistivity and the saturation region of the applied external electric fields on the contacts applied on the diamond. Further results regarding the charge collection properties, mobilities, velocities, mean free path, life times and transient times as a function of contacts and applied external electric fields are also presented.

An influence of boron impurity in the electronic properties of a type Ib diamond with concentration of SSN of about 50 ppm was also investigated. Two distinct regions of the diamond were probed with minimum ionizing particles obtained from a ^{90}Y source.

Timing properties, as a function of concentration of SSN, was also investigated in two type Ib diamonds with differences in the concentrations of SSN of about 165 ppm. This particular investigation was performed using α-particles.

1.1 Layout of the thesis

The thesis consists by an abstract, acknowledgments, six chapters briefly described in this layout, an appendix and the bibliography.

Chapter one

In this chapter a description is given of the properties of diamond that makes it attractive to various applications, particularly for the electronic device application, its classification according to the type of impurities present in the bulk, a brief history of diamond electronics over the past 50 years, recent developments and the goal of the present work.

Chapter two

This chapter contains the supportive theoretical background and literature review for the present work. In addition, the important concepts such as the compensation factor between the single substitutional nitrogen (SSN) and boron impurities in diamond, the effect of presence of uncompensated boron impurity in the conduction properties of the material, the role of impurities in the properties of contacts, the timing properties of an electronic device depending on the type of contacts, are introduced.

Chapter three

Describes the synthesis processes of a diamond in the high pressure and high temperature (HPHT) environment, the preparation of a diamond before the construction of an electronic device, the preparation and characterization of the surface of a diamond prior to metal evaporation to form contacts, the presence of crystallographic defects on the samples investigated, the type of impurities and their concentrations in the bulk of the samples investigated. Several spectroscopic techniques were

such as *X-ray photoelectron spectroscopy* (XPS), to characterize the chemical composition of the surface, the *scanning electron microscopy* (SEM) to evaluate the morphology of the surfaces, the *birefringence* and *X-ray white beam topographies*, the *Raman scattering*, *cathodoluminescence topography*, and *electron spin resonance* (ESR). The most relevant characterization results were obtained from synthetic type IIa ultra-pure diamonds, and are related to the value of concentration SSN, which is approximately 10^{13} cm^{-3} and the presence of boron impurity observed as a blue luminescence emitted from the bulk.

Chapter four

In this chapter, results from the electronic characterisation of the samples investigated are presented. The results include current-voltage characteristics as a function of type of contacts and impurities in the bulk, fluctuation in timing properties of a diamond electronic device for different applied external electric field as a function of type of contacts. The most relevant results presented in this chapter were obtained from a type IIa ultra-pure diamond, describing the variation of energy levels of boron impurity acceptors throughout the bulk of the diamond the electronic properties of the material, namely, the current density, the charge collection properties, the mobility, velocity, the transit and the life times of charge carries generated by the incident photon with energy just above the band gap. The results were obtained at low and at room temperatures with two different types and quality of contacts.

Chapter five

In this chapter, results are presented in connection with the charge collection and the timing properties with respect to different concentrations of SSN in different regions of a type Ib diamond. Memory behaviour was also observed in this material after irradiating with α-particles.

Chapter six

This chapter provides a summary of the most relevant results regarding concentrations of SSN and boron impurities and the variation of energy levels introduced by boron impurity throughout the bulk of a synthetic type IIa HPHT ultra-pure diamond is presented. The chapter concludes comparing results from electronic characterizations obtained using synthetic type IIa HPHT ultra-pure diamond by exploring two different types of contacts.

Appendix

The chapter constitutes an appendix, in which preliminary and supportive experiments performed in different types of diamonds are presented.

Bibliography

Contains literature used as a supportive tool of the overall work.

Chapter 2

Theoretical Background

2.1 Introduction

This chapter reviews the most relevant theories and experimental results, concerning electronic properties of diamond, as a supportive tool for the present work. It includes the description of effects of impurities and crystallographic defects on the electronic properties of diamond and the electric contacts. A brief description of interactions of charged particles with matter, principle of particle detection and timing properties of the material is given. In this work, we also investigate electronic properties of diamond specimens of exceptional high purity, meaning highly reduced concentrations of SSN. This is important since it has been observed that some synthetic type IIa single crystal HPHT diamonds, with reduced concentrations of SSN, are weak p-type semiconducting material. Therefore, the most relevant theories and results obtained from p-type semiconducting diamond, investigated by previous authors, are also introduced in this chapter, as a guide to the interpretation of the experimental results obtained in this work.

2.1.1 The lattice structure of diamond

The cell structure of diamond is face centered cubic (fcc) lattice with bases of two atoms at [21, 22] 000; $\frac{1}{4}, \frac{1}{4}, \frac{1}{4}$. This is illustrated in Fig. 2.1. The position of one atom is described by coordinate at the origin, $\overrightarrow{0}$, and the orthogonal coordinate system composed by unit vectors $\{\overrightarrow{e_1}, \overrightarrow{e_2}, \overrightarrow{e_3}\}$. The position of the second atom in the primitive cell is given by

$$\frac{a(\overrightarrow{e_1} + \overrightarrow{e_2} + \overrightarrow{e_3})}{4}, \tag{2.1.1}$$

where a is the point base. The distance between the two atoms using the coordinate systems is given by [21, 22]

$$\left\{\overrightarrow{d}_1, \overrightarrow{d_2}\right\} = \left\{\overrightarrow{0}, (\overrightarrow{e_1} + \overrightarrow{e_2} + \overrightarrow{e_3})\frac{a}{4}\right\}. \tag{2.1.2}$$

The numeric value of the distance between the two atoms in the primitive cell is $|\overrightarrow{d_2}| = a\frac{\sqrt{3}}{4} = 1.54$ Å. The volume of the unit cell is given by the three point basis [21, 23]

$$V = \frac{a^3}{4} = \overrightarrow{a}_1 \circ (\overrightarrow{a}_2 \times \overrightarrow{a}_3), \tag{2.1.3}$$

and the fcc lattice is described by four point basis

$$\{\overrightarrow{0}, \frac{a}{2}(\overrightarrow{e}_1 + \overrightarrow{e}_2), \frac{a}{2}(\overrightarrow{e}_2 + \overrightarrow{e}_3), \frac{a}{2}(\overrightarrow{e}_1 + \overrightarrow{e}_3)\}. \tag{2.1.4}$$

Equation (2.1.2) is simplified as $\{\overrightarrow{0}, \overrightarrow{a}_1, \overrightarrow{a}_2, \overrightarrow{a}_3\}$. The point bases defines the electrical properties of diamond trough the reciprocal lattice bases $\overrightarrow{b_i}$, defined as

$\overrightarrow{b}_i \equiv (\pi/V)\varepsilon_{ijk}\overrightarrow{a}_j \times \overrightarrow{a}_k$, where i, j, k ={1, 2, 3}. Its linear combination is given by [21, 22],

$$\overrightarrow{G} = n_i \overrightarrow{b}_i, \tag{2.1.5}$$

where n_i is the Miller indices.

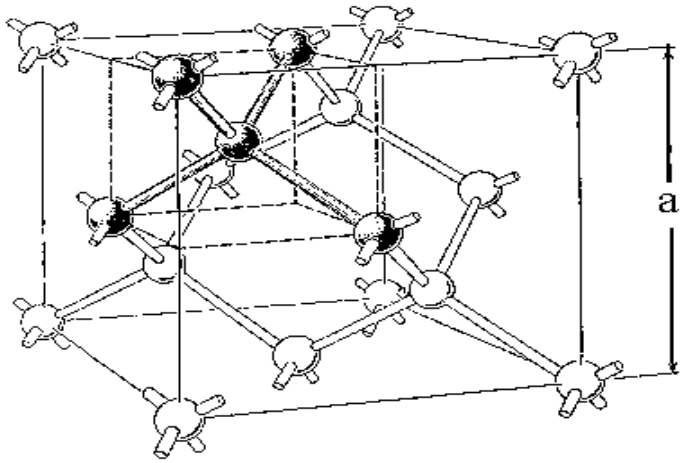

Figure 2.1: The unit cell of the diamond with the cubic lattice structure. (a) is the lattice dimensions which is about 3.6 Å. The interatomic distance in diamond is about 1.54 Å[18].

2.2 Electronic band structure of diamond

Energy band structure of diamond originates from a superposition of wave functions of electrons in primitive cell. The point of maximum energy in the valence band touches the wave vector, at k_0, near the band edge. The valence band is three fold degenerated in absence of spin orbit split. The ground state of electrons in the tetrahedral structure of carbon corresponding to diamond is in the sp^3 structure. The conduction band has a spherical energy surface orientated along a <100> crystal

axis, with symmetry point at X_1, if the valence band lies at center zone [21, 24, 25]. In Fig. 2.2, **k** represents the wave vector, L, Γ, and X are the coordinates of the

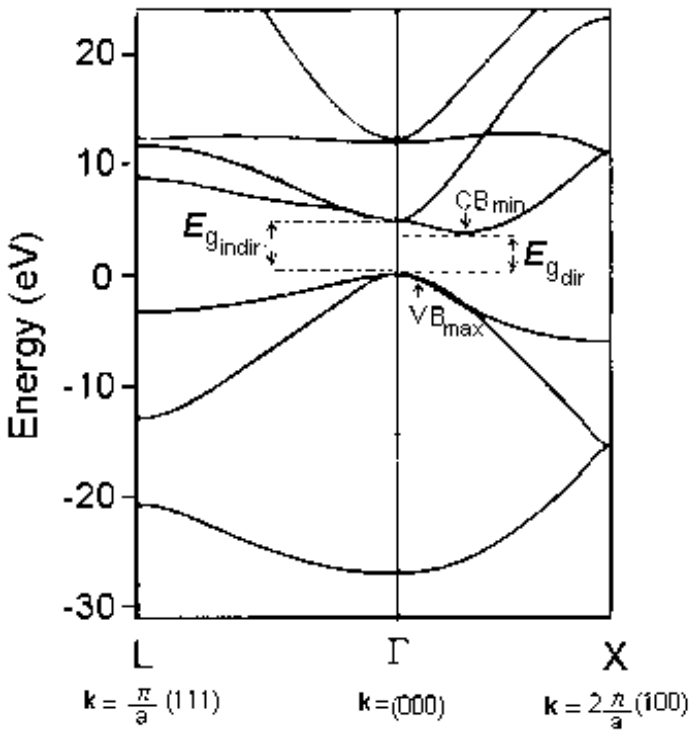

Figure 2.2: Energy band structure of diamond along < 100 > and < 111 > axis of the Brillouin zone [23]. L, Γ and and X.

valence and the conduction bands. These coordinates represent the center of the Brillouin zone, a region of high symmetry. In Fig. 2.2, VB_{max} is the valence band maxima and CB_{min} is the conduction band minima, and the difference between these two parameters, corresponds to the indirect energy band gap ($E_{g_{indir}}$). The value of the indirect band gap in diamond is approximately 5.470 ± 0.005 eV [24].

The energy band structure of diamond also shows a direct band gap, which results from the difference between the minimum of the upper most valley and the maximum of the valence band, both aligned at k_0. The corresponding value of the direct band

gap ($E_{g_{dir}}$) is approximately 7.02 ± 0.02 eV [24].

The energy of band gap can be measured through continuous optical absorption at a certain corresponding frequency, such that $E_g = \hbar\nu_g$, where $\hbar\nu_g$ is the absorbed photon energy. Such absorption creates ionization by removing an electron from the valence to the conduction band, in a process called direct transition. On the other hand, the transfer of an electron from the valence to the conduction band can be a phonon-assisted process, where a charged particle is involved. This means that the energy of a charged particle is divided between the excitation and ionization processes. The final state of an electron excited into the gap requires a momentum transfer to the conduction band. This process is designated an indirect transition, which result from the fact that CB_{min} and the VB_{max}, as shown in Fig. 2.2, are not aligned at k_0.

The energy of an electron in valence band maxima is given by [21, 22]

$$E(\overrightarrow{K}) = E_v - \frac{\hbar^2 \overrightarrow{K}^2}{2}\Big(\frac{1}{m_{hh}} + \frac{1}{m_{lh}}\Big), \tag{2.2.1}$$

where $\overrightarrow{K}$ is the wave vector near the band edge and E_v is the energy of the valence band and is given by

$$E_v = -\frac{\hbar^2 \overrightarrow{k}^2}{2}\Big(\frac{1}{m_{hh}} + \frac{1}{m_{lh}}\Big), \tag{2.2.2}$$

where $\hbar$ is Planck's constant, $\overrightarrow{k}$ is the wave vector of holes in valence band, m_{hh} is the mass of heavy holes and m_{lh} is the mass of light holes. In Eqs. (2.2.1) and (2.2.2) the mass of holes in spin-orbit splitting (m_{so}), of about 0.15 m_e [26] is not

included due to its negligible value. In natural type IIa diamond, $m_{hh} = 1.1\ m_e$ and $m_{lh} = 0.3\ m_e$, and m_e is the rest mass of a free electron [26].

The energy of an electron in the conduction band minima is given by

$$E(\overrightarrow{K}) = E_c + \Big(\frac{\hbar^2 \overrightarrow{K}^2}{2m_e}\Big), \tag{2.2.3}$$

where E_c is the energy in the conduction band, which is spherical along the <100> axis, with

$$E_c = E_g + \frac{\hbar^2 k^2}{2m_e}, \tag{2.2.4}$$

where E_g is the energy of the band gap, $\overrightarrow{k}$ is the wave vector of electrons in the conduction band.

The density of states in the valence band maxima (VB_{max}) for intrinsic semiconductor is given by [21]

$$D_h(E(\overrightarrow{K})) = \frac{1}{2\pi}\Big(\frac{2m_h}{\hbar^2}\Big)^{3/2}(E_v - E(\overrightarrow{k}))^{1/2}. \tag{2.2.5}$$

Hence, the concentration of holes becomes

$$n_h = 2\Big(\frac{m_h k_B T}{2\pi\hbar^2}\Big)^{3/2} \exp[(E_v - E_F)/k_B T], \tag{2.2.6}$$

where E_F is the Fermi-level, k_B is Boltzman's constant and T is the absolute temperature [21, 22].

The density of states in the conduction band minima (CB_{min}) is given by

$$D_n(E(\overrightarrow{K})) = \frac{1}{2\pi}\left(\frac{2m_e}{\hbar^2}\right)^{3/2}(E(\overrightarrow{k}) - E_c)^{1/2}. \tag{2.2.7}$$

The concentration of electrons in the conduction band is given by

$$n_e = 2\left(\frac{m_e k_B T}{2\pi\hbar^2}\right)^{3/2}\exp[(E_c - E_F)/k_B T]. \tag{2.2.8}$$

In the case of ideal diamond, $E_c - E_F = 2.5$ eV. The intrinsic charge carrier is given by square root of a product of Eqs. (2.2.6) and (2.2.8), such that

$$n_i = \sqrt{n_e n_h} = 4\left(\frac{m_e k_B T}{2\pi\hbar^2}\right)^{3/2}(m_e m_h)^{3/4}\exp(-E_g/k_B T). \tag{2.2.9}$$

2.2.1 Transport properties in ideal single crystal diamond

Ideal single crystal is characterised by a periodic array of potential wells with discrete levels. In the absence of an external perturbation the periodicity in a single crystalline structure is described by the following Schrödinger equation [27, 28]:

$$H\psi(\overrightarrow{k}, \overrightarrow{r}) + R_i = E\psi(\overrightarrow{k}, \overrightarrow{r}) + R_i, \tag{2.2.10}$$

where R_i is the crystal periodicity and $\psi(\overrightarrow{k}, \overrightarrow{r})$ is the wave function of an electron in a periodic and unperturbed crystal potential, given by Bloch's Theorem [27, 28]:

$$\psi(\overrightarrow{k}, \overrightarrow{r}) = e_{\mathrm{i}}^{\mathrm{ik.R}} U_{\overrightarrow{\mathrm{k}}, \overrightarrow{\mathrm{r}}}, \tag{2.2.11}$$

where $U_{\overrightarrow{\mathrm{k}}, \overrightarrow{\mathrm{r}}}$ is the potential in the cell periodic function, which can be written in following way [27, 28]:

$$U(\overrightarrow{r}) = U(\overrightarrow{r} + \overrightarrow{R}). \tag{2.2.12}$$

According to Bloch's Theorem, for an unperturbed periodic single crystal, the wave vector and the vector of reciprocal lattice remain unchanged, $\overrightarrow{\mathrm{K}} = \overrightarrow{\mathrm{G}}$.

When a crystal is under the influence of an external perturbation, Bloch's Theorem is expanded into a set of Bloch's functions for a time dependent wave packet. The periodicity in a crystal is not conserved, as it is replaced by a set of discrete steps due to motion of charge carriers. Interaction of an electromagnetic field with a perfect crystal, which sets a weak field in the bulk, can generate weakly bound states of charge carriers with long life times and very sharp energy pulses. This process is described by a time dependent wave packet and is expanded into Bloch's functions [28, 29]:

$$\Psi(\overrightarrow{r,t}) = \sum_{\mathrm{n}} \int \mathrm{d}^3\mathrm{k} \Phi_{\mathrm{n}}(\overrightarrow{k,t}) \psi_{\mathrm{n}}(\overrightarrow{k}, \overrightarrow{r}), \tag{2.2.13}$$

where $\phi_{\mathrm{n}}(\overrightarrow{k,t})$ satisfies the Schrödinger equation for a time-dependent wave packet in a crystal momentum representation. When the crystal is under the influence of a strong electric field, the ordinary localized bound state of charge carriers will vanish. Therefore, electrons will have a finite probability of tunneling from left to the right of the square well potential.

The simplified equation of motion for an electron in an intrinsic material, under the influence of a strong electric field is given by:

$$\hbar\partial_{\mathrm{t}}\overrightarrow{\mathrm{k}} = -\mathrm{e}\overrightarrow{\mathrm{E}}(\overrightarrow{r},\mathrm{t}), \tag{2.2.14}$$

where $\overrightarrow{E}(\overrightarrow{r,t})$ is the time-dependent electric field, which results from the motion of charge carriers.

The velocity of electrons and holes in the conduction and in valence bands is given by [21, 30]

$$\overrightarrow{v}_{\mathrm{c}} \equiv \frac{\partial E_{\mathrm{c}}(\overrightarrow{k})}{\hbar\partial\overrightarrow{\mathrm{k}}} \quad , \quad \overrightarrow{v}_{\mathrm{v}} \equiv \frac{\partial E_{\mathrm{v}}(\overrightarrow{k})}{\hbar\partial\overrightarrow{\mathrm{k}}}, \tag{2.2.15}$$

where $E_{\mathrm{c}}(\overrightarrow{k})$ and $E_{\mathrm{v}}(\overrightarrow{k})$ are the energies of electrons in the conduction and valence bands, respectively. The velocity in the band edge as a function of wave vector is given by

$$\upsilon_{\mathrm{g}} = \frac{1}{\hbar}\frac{\partial E(\overrightarrow{K})}{\partial\overrightarrow{K}}, \tag{2.2.16}$$

where υ_{g} is also known as the group velocity and $E(\overrightarrow{K})$, given in Eqs. (2.2.1) and (2.2.3), is also known as the dispersion relation. Differentiating υ_{g} with respect to time, it is possible to determine the effective mass in the band gap using Newton's second law [21, 22]:

$$\frac{\mathrm{d}\upsilon_{\mathrm{g}}}{dt} = \frac{1}{\hbar^2}\frac{\mathrm{d}^2E(\overrightarrow{K})}{\mathrm{d}\overrightarrow{K}^2}F, \tag{2.2.17}$$

where F is the force applied to the charge carrier and is given by [21]:

$$\frac{1}{\hbar^2}\frac{\mathrm{d}^2 E(\overrightarrow{K})}{\mathrm{d}\overrightarrow{K}^2} = \frac{1}{\mathrm{m}^*}, \tag{2.2.18}$$

where m^* corresponds to the effective mass in conduction or in valence band. The mobility of intrinsic charge carriers in the semiconductor is given by

$$\mu = \mathrm{e}\Big(\frac{\tau_\mathrm{c}}{\mathrm{m}_\mathrm{c}^*} + \frac{\tau_\mathrm{v}}{\mathrm{m}_\mathrm{v}^*}\Big), \tag{2.2.19}$$

where e is the charge of electron, τ_c and τ_v are charge carrier life-times in the conduction and valence bands.

The intrinsic conductivity in the material is given by [30]:

$$\frac{1}{\rho} = \mathrm{en_i}(\mu_\mathrm{c} + \mu_\mathrm{v}). \tag{2.2.20}$$

This parameter is a function of absolute temperature T, contained in the exponential factor in $\mathrm{n_i}$ given in Eq. (2.2.9). This implies a participation of phonons, responsible for scattering charges from the valence to the conduction band. The product of conductivity and the applied steady external electric field $\overrightarrow{\mathrm{E}}$, gives the current density that can be written similar to Ohm's law:

$$\overrightarrow{j} = \frac{1}{\rho}\overrightarrow{\mathrm{E}}. \tag{2.2.21}$$

Equation (2.2.21) shows that the current density will increase as a function of applied external electric field. The saturation of this parameter at high-applied external electric fields is determined by the temperature dependency of the intrinsic conductivity.

At high temperature, there will be an increase in thermal velocity, which saturates the amount of field applied to the material.

2.2.2 Impurities and energy levels

Impurities introduced in a semiconductor crystal are usually classified according to their charge configuration in the energy gap. If an impurity acquires a positive or neutral charge configuration it is classified as a donor center, while if it acquires a negative charge configuration it is classified as an acceptor center.

The energy states introduced by impurities within the band gap are classified according to the type of transition that take place. Electronic transitions from the valence or conduction bands to a particular impurity state within the energy gap results in trapping and such an impurity state is classified as deep level. The energy level, E_{T}, introduced by a trapping center is obtained through the following equation [31, 32]:

$$E_{\mathrm{T}} = \mathrm{k_B T} \ln(\nu_0 \tau), \tag{2.2.22}$$

where $\mathrm{k_B}$ is Boltzman's constant, T is absolute temperature, ν_0 is the phonon induced escape frequency and τ is the time needed to establish thermodynamic equilibrium. The density of occupied traps in a given transient time is given by [33]

$$N(t) = N(T) \exp(-e_{\mathrm{n}} t), \tag{2.2.23}$$

where t is the transient time of the charge carriers being thermally emitted from the traps, e_{n} is the thermal emission rate of electrons from the traps, N_{T} is the total density of traps. At $t = t_0$ all traps are occupied and therefore $N(t) - N_{\mathrm{T}} = 0$, and

$$N_{\mathrm{T}} = \frac{1}{\tau \upsilon_{\mathrm{th}} \sigma}, \tag{2.2.24}$$

where υ_{th} is the thermal velocity, σ is the pre-factor capture cross section, τ is the life time of the charge carrier in the trap. The capture-cross section is given by [33]

$$\sigma = \sigma_{\infty} \exp\Big(- \frac{\Delta E_{\sigma}}{\mathrm{k_B} T}\Big), \tag{2.2.25}$$

where ΔE_{σ} is the thermal activation energy of the capture cross section. The emission rate parameter, allows extraction of the effective density of states and the activation energies of trapping centers given by the following equation [31, 33]:

$$e_{\mathrm{n,p}} = \frac{\sigma_{\mathrm{n,p}} \langle \upsilon_{\mathrm{n,p}} \rangle N_{\mathrm{c}}}{\mathrm{g}} \exp\Big(- \frac{E_{\mathrm{T}} + \Delta E_{\sigma}}{\mathrm{k_B} T}\Big), \tag{2.2.26}$$

where E_{T} is the energy of the defect level below the conduction band minimum, N_{c} is the effective density of states in conduction band, g is the degeneracy factor of the defect level, T is the absolute temperature and $\sigma_{\mathrm{n,p}}$ is the apparent capture cross section for electrons (holes), which is temperature dependent due to multiphonon emission produced by lattice relaxation. The thermal activation energy for emission of an electron to the conduction band is given by

$$\Delta E_{\mathrm{a}} = E_{\mathrm{T}} + \Delta E_{\sigma}. \tag{2.2.27}$$

In order to reach the conduction band, a charge carrier should acquire a frequency above the trapping frequency [31, 32]:

$$\nu(E_{\mathrm{T}}) = \nu_0 \exp\Big(-\frac{E_{\mathrm{T}}}{\mathrm{k_B T}}\Big). \tag{2.2.28}$$

In diamond the thermal emission of charge carriers, trapped in a deep energy level, introduced by SSN as a function of temperature, occurs only at temperatures greater than 600 K, which corresponds to an activation energy of approximately $E_{\mathrm{T}} = 1.7$ eV [34].

If the transition probabilities to both energy bands are appreciable then the states introduced are classified as recombination and generation centers. These energy levels are classified as shallow donors or acceptors. The probability of equilibrium occupation for shallow donors is given by [35]:

$$\mathrm{P_D^0} = \Big[1 + \frac{1}{2}\exp\Big(\frac{E_{\mathrm{D}} - E_{\mathrm{F}}}{\mathrm{k_B T}}\Big)\Big]^{-1}, \tag{2.2.29}$$

where E_{D} is the activation energy of donors, E_{F} is the Fermi-level, $\mathrm{k_B}$. For ionized shallow donors and acceptors the probabilities are simply written as [35]

$$P_{\mathrm{D}}^{+} = 1 - P_{\mathrm{D}}^{0} \tag{2.2.30}$$

and

$$P_{\mathrm{A}}^{-} = \Big[1 + 2\exp\Big(-\frac{E_{\mathrm{F}} - E_{\mathrm{A}}}{\mathrm{k_B} T}\Big)\Big]^{-1}, \tag{2.2.31}$$

where E_{A} is the ionizing energy level of acceptors, which is a fraction of the total concentration of the impurity [35]:

$$P_{\mathrm{A}}^{-1} = 1 - P_{\mathrm{A}}^{0}. \tag{2.2.32}$$

2.2.3 Charging effects due to crystallographic defects

High concentration of impurities in diamond introduces crystallographic imperfections due to stress induced on the residence lattice site. Such defects are generated, for example, by the SSN center where nitrogen replaces the carbon atom causing strain fields and lattice dislocations. A defect may be filled with electrons or holes and in that case becomes charged and surrounded by space charge cylinders. These charged cylinders are then transformed into impenetrable polarized sites due to a variation in the internal electric fields. The potential energy in a polarized site is given by [30]:

$$V(r) = (\mathrm{Q}/2\pi\epsilon\epsilon_0)\overrightarrow{K}_0(\mathrm{r}/\lambda_{\mathrm{D}}), \tag{2.2.33}$$

where λ_{D} is the Debye length, ϵ is the dielectric constant of the medium, ϵ_0 is the permittivity of the free space and $\overrightarrow{K}_0$ in this equation represents the coefficient of expansion [30]. For example, the charge created around the dislocation per unit line in a semiconductor material at a steady applied external electric field $|\overrightarrow{E}|$ is given by [30]

$$\mathrm{Q} = \int_0^{\infty} [r^{-1} d(rE)/dr] 2\pi r dr, \tag{2.2.34}$$

where r is the length of the dislocation [30], E is the electric field around the dislocation, which is a function of the steady external applied electric field. The solution of the integral is about 2πA if the value of the electric field is about $\mathrm{A}\,\overrightarrow{K}_1/\lambda_{\mathrm{D}}$, where A = r*E. Equations (2.2.33) and (2.2.34) imply that the pulse height of a particle detector, implemented with such a crystal, depends on the amount of charge trapped around the defect.

2.3 P-type Semiconducting Diamond

The presence of boron acceptors in diamond introduces hyperfine structures as referred to in [36]. The energy band structure of a diamond doped with boron comprises of the ground state of boron with 1s ($\mathrm{p}_{3/2}$) and its spin-orbit-split of 1s ($\mathrm{p}_{1/2}$). A set of Lyman transitions, extending down to the third band spin-orbit-split $\mathrm{p}_{1/2}$ of the valence band, are observed under an applied external magnetic field [36]. The presence of these energy levels influences the conductivity of a p-type semiconducting diamond. The theoretical activation energy of an acceptor in diamond is obtained using the following equation [37]:

$$E_{\mathrm{A}} = \left(\mathrm{m}_{\mathrm{h}}^{*}/\mathrm{m}_{\mathrm{e}}\right).(1\varepsilon_{\mathrm{r}})^2.\mathrm{R}_{\mathrm{y}}, \tag{2.3.1}$$

where $\mathrm{m}_{\mathrm{h}}^{*}$ is the effective mass of holes, $\approx \mathrm{m}_{\mathrm{e}}$, which is the rest mass of a free electron, R_{y} is the Rydberg constant (about 13.6 eV) and $\varepsilon_{\mathrm{r}} = 5.7$ is the dielectric permittivity

of diamond. The theoretical result of about 0.41 eV [37] for the ground state is very close to the experimentally obtained value of about 0.37 eV. The activation energies introduced by the impurity states in diamond define the type of conduction regime of the material as a function of temperature and concentration of the boron acceptor. The conduction regimes are classified as band, hopping and metallic conductions. The conductivity in the presence of boron acceptors is given by the following equation [38, 70]:

$$\sigma(T) = \sigma_1^{-\epsilon_1/\mathrm{k_B}T} + \sigma_2^{-\epsilon_2/\mathrm{k_B}T} + \sigma_3^{-\epsilon_3/\mathrm{k_B}T}, \tag{2.3.2}$$

where ϵ_1 is the activation energy in the band conduction regime, ϵ_2 is the activation energy in a regime between band and hopping conductions, ϵ_3 is the activation energy in hopping conduction regime [38, 70].

The band conduction describes the conductivity in the valence band and the hopping conduction is of two types, namely, the nearest-neighbor-hopping (NNH) and the variable-range-hopping (VRH).

The conduction through NNH is characterized by a transition of an electron to a nearest unoccupied level, whereas the conduction through VRH occurs between levels separated by a hopping distance (R), such that ($2\alpha\mathrm{R} - E_{\mathrm{dsp}}/\mathrm{k_B T}$) is a minimum. The probability of occurrence of hopping conduction is given by [70]

$$\mathrm{P} = \nu_{\mathrm{ph}} \exp(-2\alpha R - E_{\mathrm{dsp}}/\mathrm{k_B}T), \tag{2.3.3}$$

where ν_{ph} is phonon frequency, $2\alpha R$ is a term related to the overlap of the wave function, α^{-1} characterizes the extension in space of a wave function, and E_{dsp} is the dispersion in energy.

The metallic conduction regime is achieved at concentrations $\gg 1{\times}10^{20}$ cm^{-3} which is the above the Mott transition limit [38]. The concentration of holes in the valence band, due to presence of boron, is given by [70]

$$\mathrm{p}\frac{N_{\mathrm{D}}+\mathrm{p}}{N_{\mathrm{A}}-N_{\mathrm{D}}-\mathrm{p}} = \Big(\frac{2\pi \mathrm{m}^{*}\mathrm{k_B T}}{\mathrm{h}^2}\Big)^{3/2}\exp\Big(-\frac{E_{\mathrm{A}}}{\mathrm{k_B}T}\Big), \tag{2.3.4}$$

where p is the concentration of holes, N_{A} is the density of acceptors, N_{D} is the density of compensating donor, E_{A} is the activation energy of the acceptor center, m^{*} is the effective mass of holes and h is the Planck's constant. Figures. 2.3 and 2.4 illustrate the conductivity of a boron-doped diamond as a function of temperature and the resistivity as a function of concentration of boron acceptors, respectively.

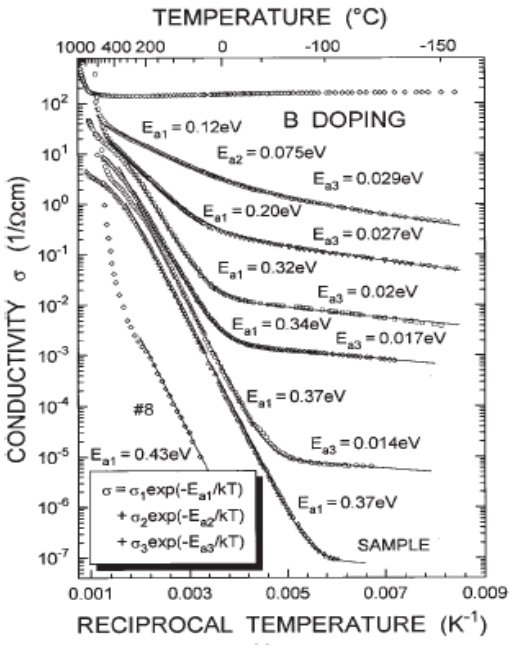

Figure 2.3: Conductivity in p-type diamond as a function of energy levels of boron acceptors and temperatures [70].

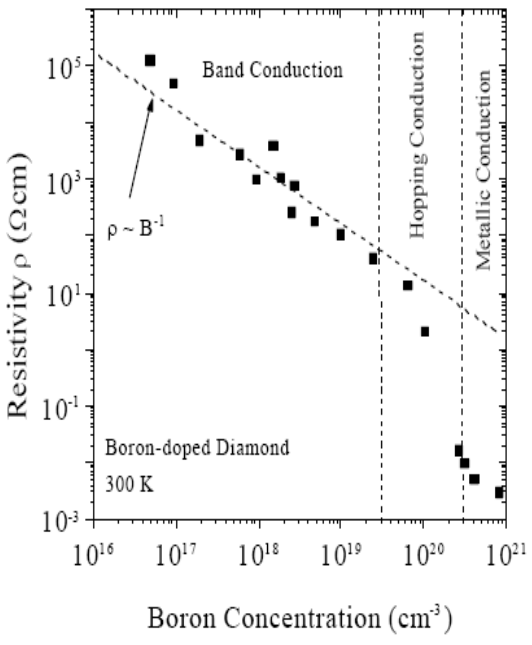

Figure 2.4: Resistivity and type of conduction vs concentration of boron acceptors at room temperatures [40].

2.3.1 Position of the Fermi-level in diamond as a function of concentration of impurities

Unlike other semiconductors such as germanium and silicon, in a diamond the position of the Fermi-level is a function of concentration of SSN impurity relatively to an acceptor center such as boron [17]. This impurity is known to increase the conductivity of the diamond, which is not desirable for particle detection application. To eliminate the effect of boron acceptors, a certain concentration of SSN above the concentration of boron acceptors is introduced in order to compensate for this impurity [41]. The Fermi-level takes only two positions, as described in reference [17], as shown in Fig.2.5. One corresponds to the activation energy of

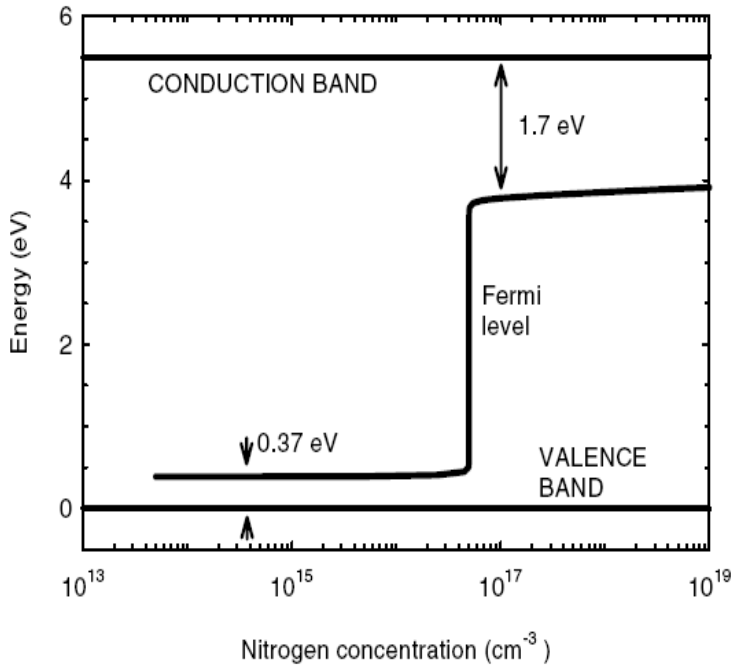

Figure 2.5: Position of the Fermi-level as a function of nitrogen donor concentration for a diamond containing 5 $\times 10^{16}$ cm^{-3} of boron acceptors [17].

the SSN, if all boron acceptors are compensated. The second position corresponds

to the activation energy of uncompensated boron acceptors, which occurs whenever the concentrations of both impurities are the same or if the concentration of the SSN is lower. This results from the fact that the SSN is hardly ionized at room temperatures, which leads to a lower compensating factor of impurities compared to other semiconductors [17, 42]. In this case, if boron is not fully compensated, the Fermi-level estimated in the carrier freeze-out region, is given by the following equation [17]:

$$E_{\mathrm{F}} = E_{\mathrm{A}} - \mathrm{k_B}T \ln\Big(\frac{N_{\mathrm{a}} - N_{\mathrm{d}}}{2N_{\mathrm{d}}}\Big), \tag{2.3.5}$$

where E_{A} is the activation energy of the acceptors levels, and N_{a} and N_{d} are the density of acceptors and donors, respectively, and the Fermi-level is about 0.37 eV.

Due to reasons already described, the position of Fermi-level is never at equilibrium between two energy states introduced by the SSN and boron impurity. Therefore, the resistivity of the diamond will be high when the Fermi-level is about 1.7 eV and low when the Fermi-level is about 0.37 eV, as seen in Fig. 2.5. On the other hand, when the concentration of uncompensated boron acceptors increases the resistivity will decrease drastically [3, 43]. Below the Mott transition limit at the concentration of boron acceptors, of about $\times 10^{14}$ cm^{-3}, the resistivity of the diamond can vary between TΩcm and GΩcm. Near the Mott transition limit the resistivity can vary between MΩcm and Ωcm. When the concentration reaches values of $\geq 10^{20}$ cm^{-3} the resistivity values are of the order of 1 Ωcm and below.

2.4 Energy loss of charged particles in matter and ionization processes

A charged particle during its passage through a material interacts with the electrons and the nuclei resulting in electronic and nuclear energy loss. The energy loss due to interactions with nucleus is negligible, however, a slight deflection of incident charged particle might occur. The electronic energy loss is due to interactions between the incident charged particle and the atomic electrons in which the incoming charged particle transfers a portion of its energy to the electrons, causing electronic excitations and ionization [44]. The mean rate of energy loss in matter for an incident charged particle of very low mass, with the velocity βc larger than the orbital electrons is given by the Bethe-Bloch equation [45, 46]:

$$-\frac{\overline{dE}}{dx} = 4\pi \mathrm{N_A r_e^2 m c^2} \frac{Z}{A} \varrho \frac{1}{2\beta^2} \mathrm{z^2} \Big[\ln\Big(\frac{2m_\mathrm{e} c^2 \eta^2 T_{\max}}{I^2(Z)} \Big) - 2\beta^2 \Big], \tag{2.4.1}$$

where the $\mathrm{N_A}$ is Avogadro's number, r_e=$\alpha/\mathrm{m_e}$ is the classical electron radius, being α=1/137 for (c=1), ϱ is the mass density, A is the mass number, I is the ionizing potential of the medium, η=$\beta\gamma$, $T_{\max}$ is the maximum kinetic energy, which is imparted to a free electron in a single collision and is given by [29]

$$T_{\max} = \frac{2m\mathrm{c}^2\eta^2}{1 + m2E/M^2c^2 + m^2/M^2}, \tag{2.4.2}$$

where M is the mass of the ion and m is the atomic mass of the target. In collisions, in which the mass of the incident ion is equal to the mass of the atom of the target, $T_{\max}$=$(\gamma-1)\ mc^2$.

At high relativistic velocities there will be saturation of energy loss which is mainly observed in gaseous and thin solid-state detectors. This is due to the production of delta electrons that removes the energy from the point of interaction. The calculation of the mean rate of energy loss is performed by subtracting the density correction δ from the square brackets in the Eq. (2.4.1).

2.4.1 Electron energy loss

On the other hand, the energy loss of electrons is slightly different from heavy ions. This results from electromagnetic interactions with the atomic electrons and nuclei. Electrons do not travel in a straight line in the bulk, due to repulsive interactions with core electrons and attractive interactions with atomic nuclei. The energy loss by electrons in matter is given by [44, 47]:

$$-\frac{dE}{dx} = \frac{4\pi \mathrm{e}^4 \Pi}{\mathrm{m}c^2}\Big(\log\frac{\mathrm{m}_e}{\upsilon^2 2I} - \frac{1}{2}\log 2 + \frac{1}{2}\Big). \tag{2.4.3}$$

Electrons have additional energy loss when subjected to violent deceleration during the collisions. This generated electromagnetic radiation is known as Bremsstrahlung. In the medium Bremsstrahlung depends on the radiation length parameter, which depends on the atomic number Z and on the mass density ϱ of the material.

The radiation length is defined as the distance traveled by highly relativistic electrons in matter before they lose 1/e or $\sim$67% of its energy by Bremsstrahlung. The radiation length is a characteristic property of a material and is given by [44, 47]:

$$X_0 = \frac{716.4\mathrm{g/cm^2}A}{\varrho Z\Big(Z+1\Big)\ln\Big(287/\sqrt{Z}\Big)}. \tag{2.4.4}$$

Diamond is a material with a very small average Z of about 6 and a mass density of about 3.52 $\mathrm{gcm^{-3}}$. This gives a large value for the radiation length as compared to other materials, being about 121 mm. The larger this parameter is then the lower the probability of production of Bremsstrahlung radiation.

2.5 Design of a diamond based electronic device

A particle detector is easily implemented by depositing electrodes on the surfaces of a semiconducting crystal in parallel-plate geometry. The operation of such a device is described by the Schokley-Ramo Theorem as detailed in Refs. [48, 49, 50]. The total current induced in one of the electrodes, is given by

$$i = \frac{1}{V_0}\int_{\mathrm{vol}} \overrightarrow{E}.\overrightarrow{J}_{\mathrm{T}}\mathrm{dx}, \tag{2.5.1}$$

where V_0 and $\overrightarrow{j}_{\mathrm{T}}$ are the initial potential and the total current density on the electrode, respectively, and $\overrightarrow{E}$ is the applied external electric field on the device. The total current density in the device is the sum of the current density due to the motion of the free carriers in the bulk and the displacement current, due to variation of electric fields as a function of time [48, 49, 50]:

$$j_{\mathrm{T}} = j + \varepsilon\Big(\frac{\partial}{\partial t}\Big)\sum_{\mathrm{i}=1}^{3}\overrightarrow{E}_{\mathrm{i}}, \tag{2.5.2}$$

where $\overrightarrow{E}_{\mathrm{i}}$ is the electric field in regions i = (1,2,3...) of the device.

In a steady applied electric field the second term, described by the current density due to displacement, is equal to zero and the current induced at the electrodes by the movement of carriers in the depletion region is given by [48]:

$$i(t) = \frac{1}{\left(A_{\text{plate 1}} - A_{\text{plate2}}\right)} \int_{Plate_1}^{Plate_2} j(x,t)dx, \tag{2.5.3}$$

here $A_{(\text{plate (1,2)})}$ refers to the areas of contacts on opposite surfaces, x is the path length of the charge carrier and t is the collection time of the charge carriers in one of the metal plates. The current density at the electrodes can also be written as

$$j = \mathrm{e}[n\mu_{\mathrm{e}} + p\mu_{\mathrm{h}}] \mid \overrightarrow{E} \mid, \tag{2.5.4}$$

where e is the elementary charge, $\mu_{(\mathrm{h,e})}$ is the mobility of holes and electrons, n and p correspond to the density of electrons and holes, respectively, and $\mid \overrightarrow{E} \mid$ is the applied external electric field in the device. The resistivity of the electrodes is given by the ratio between the applied electric field and the current density at the electrodes,

$$\rho = \left(\frac{\partial J}{\partial v}\right)_V^{-1} = 0. \tag{2.5.5}$$

The conduction properties of a device made of intrinsic semiconducting material are determined by the Schottky barrier height at the interface junction. This parameter is dependent on the type of impurity donor or acceptor present in the semiconductor

and on the density of states introduced on the surface. The presence of impurities in the crystal changes the conductivity parameters resulting in formation of a barrier height, as in the case of a p-type semiconducting diamond, and special care has to be taken in order to reduce the leakage current.

The barrier height in a p-type material results from a difference between the valence band edge and the Fermi-level in the metal. The theoretical value of this parameter for a p-type boron semiconducting diamond according to references [51, 52] was estimated to be about of 1.8 eV. However, several values obtained experimentally for the <111> surface of a p-type diamond were below this value [51]. The Schottky-barrier height for p-type diamond is given by [53]:

$$\phi_{\mathrm{Bp}} = S_{\phi}\Big[E_{\mathrm{g}} - \Big(\Phi_{\mathrm{m}} - \chi_{\mathrm{Diam}})\Big)\Big] + \Big(1 - S_{\phi}\Big)\Phi_0, \tag{2.5.6}$$

where ϕ_0 is the neutral level, which is estimated to be about 1.4 eV above the valence band [53], ϕ_{m} is the work function of the metal, χ_{Diam} is the electron affinity on the surface of the semiconductor (for a diamond with <100> orientation, according to references [51, 54], is about 2.3 eV), $\mathrm{E_g}$ is the diamond band gap and S_{ϕ} is the interface index, which in p-type diamond has the value of about 0.4 [55]. Similarly, the barrier height in n-type diamond is given by

$$\phi_{\mathrm{Bn}} = S_{\phi}\Big[\Big(\Phi_{\mathrm{m}} - \chi_{\mathrm{Diam}})\Big)\Big] + \Big(1 - S_{\phi}\Big)\Phi_0. \tag{2.5.7}$$

For n-type diamond ϕ_{Bn} was experimentally measured and the value was found to be about 1.77 eV [56]. When conduction is performed through thermionic emission

the specific resistivity of the electrodes is a function of the barrier height and is given by [51]:

$$\rho = \propto \exp\Big(\frac{\mathrm{q}\phi_{\mathrm{B}}}{\mathrm{k_B T}}\Big). \tag{2.5.8}$$

This effect is very significant at high temperatures and low concentrations of impurities.

2.5.1 Schottky contacts

Schottky contacts are characterized by a wide barrier height at the interface junction, in which conduction is performed through transport over the barrier. When an external electric field is applied an image force $\Delta\phi_{\mathrm{B}}$ is induced which lowers the potential of the charge carriers emitted. The minimum energy for an electron to escape into the vacuum, by thermionic emission, from its initial energy at the Fermi level is equivalent to the metal work function ϕ_{m}. In the Schottky regime the charge carriers generated are blocked from the metal contact towards the bulk. The charge rejected will build up a depletion region at the interface junction with the density of charge carries in the depletion region given by [30]:

$$j = \varepsilon n_{\mathrm{s}} \sqrt{\mathrm{k_B}T/2\pi m}\, \exp[(\mid \varepsilon \mid \Delta\phi_{\mathrm{B}}/\mathrm{k_B}T) - 1], \tag{2.5.9}$$

where n_{s} is the concentration of the charges on the surface at zero applied external electric field. The work region of the device is defined by the saturation current density, in one electrode, at high applied external electric field in the device [30]:

$$j_{\mathrm{s}} = \mu_{\mathrm{s}} \mathrm{ne} \mid \overrightarrow{\mathrm{E}} \mid, \tag{2.5.10}$$

where E is the electric field strength on the surface, μ_{s} is the saturation mobility of the charge carrier generated in the bulk, n is the number of charge carriers generated and e is the charge of the electron.

The increment in the concentration of impurities decreases the depletion width more rapidly than the image force lowering the potential, $\phi_{\mathrm{B}} \propto \mathrm{N}^{1/4}$ of the Schottky barrier height [51]. Also given in Ref. [51], is the limiting case of Schottky barrier height, which often describes electronic devices made of p-type diamonds. In addition, the Schottky barrier height is determined by the chemical properties of the surfaces of the semiconductors. The presence of oxygen on the surface increases the barrier height when the metals of high ϕ_{m} are implemented as electrodes, as shown in Fig. 2.6.

2.5.2 Ohmic contacts

Ohmic contact is a depletion contact characterized by a very thin barrier at the junction interface. The conduction is performed by emission over a thin barrier height or by quantum tunnelling through the depletion layer (W) that is proportional to the square root of the impurity concentration, $\mathrm{W} \propto \mathrm{N}^{-1/2}$ [51]. In the quantum tunnelling regime the specific resistivity of the contacts is given by Eq. (2.5.5). The density of a tunnelling current in ohmic regime is integrated over the transverse direction and is given by [30]:

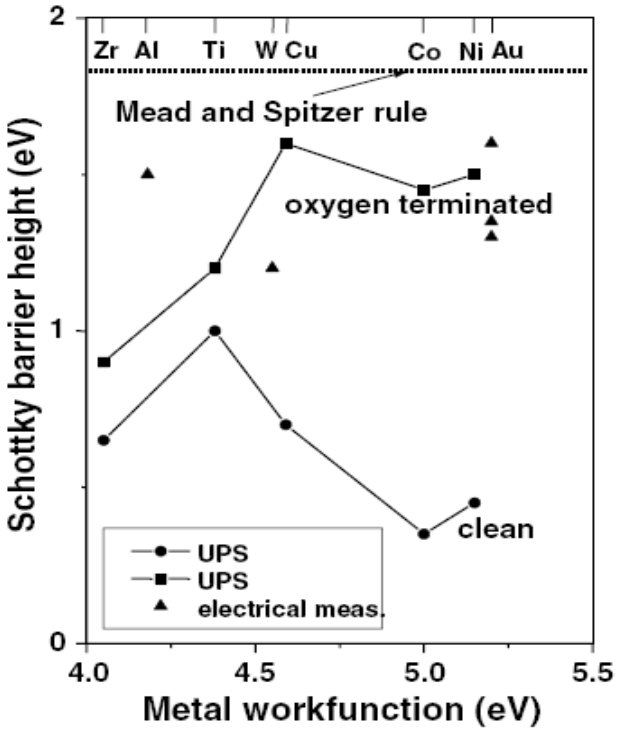

Figure 2.6: Variation of barrier height as a function of metal work function and surface termination, where UPS is the abbreviation of UV-photoemission spectroscopy, [51].

$$j = \frac{em\mathrm{k_B}T}{2\pi^2\hbar^3}\int_0^\infty \mid T_\mathrm{t} \mid^2 ln\frac{1+\exp[(E_\mathrm{F}-\varepsilon)/\mathrm{k_B}T]}{1+\exp[(E_\mathrm{F}-\varepsilon-eV)/\mathrm{k_B}T]}\mathrm{d}\varepsilon, \tag{2.5.11}$$

where $\mid T_\mathrm{t} \mid^2$ is the transmission coefficient, which is a function of time t, E_F is the Fermi energy and ε is the particle energy in the longitudinal direction, e is the charge of the electron, V is the potential in the depletion region, $\mathrm{k_B}$ is Boltzmann's constant and $\hbar$ is Planck's constant divided by 2π, ε is the characteristic tunnelling energy that describes the tunnelling probability. This parameter is dependent on the density of states at the interface and is given by the following relation [30, 51]:

$$\varepsilon = \frac{\mathrm{qh}}{4\pi}\sqrt{\frac{N}{m^*\epsilon_0\epsilon}}, \tag{2.5.12}$$

where ϵ_0 is the dielectric constant in free space, ϵ the dielectric constant of the material, m^* is the effective mass of charges, N is density of states at the interface, q is the charge and h is Planck's constant.

The conduction property in a particle detector, implemented with type Ib diamond or type IIa natural diamond, is often affected by the space-charge effect, as shown in Fig. 2.7. This results from the presence of defects responsible for the generation of polarized clusters [57] near the contact region and in the bulk during the detection process as already referred in Subsection 2.2.2.

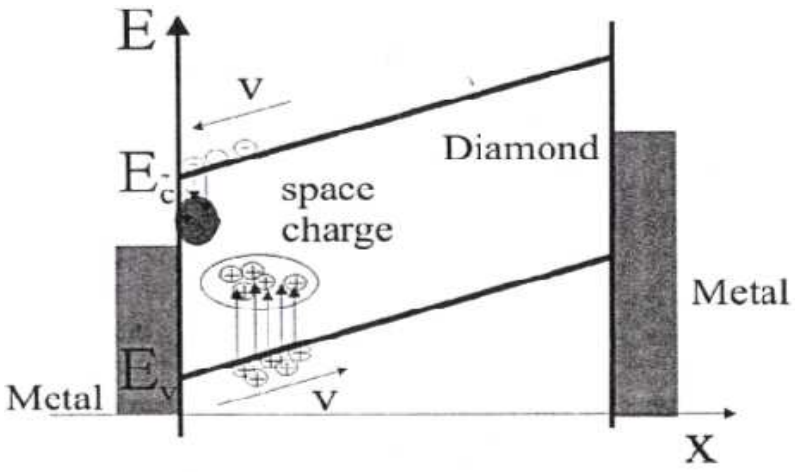

Figure 2.7: A schematic diagram of space charge effect in a detector made of diamond. The depletion region is additionally influenced by localized fields generated by clusters of charge carriers around the defects [32].

2.5.3 Pulse height distributions for a diamond detector

Ionization of a medium occurs when a charged particle deposits sufficient energy to transfer an electron from the valence band maximum to the conduction band minimum. The valence band becomes ionized with a hole and the conduction band

minima become ionized with an electron. A high field is imposed across the device from the front electrode to the back and the generated electrons and holes migrate contributing to the conductivity [58]. The total energy deposited in a detector is estimated using the following equation:

$$E_{\mathrm{T}} = -D\Big(\frac{\overline{dE}}{dx}\Big), \tag{2.5.13}$$

where D is the thickness of the detector and $\overline{dE}/dx$ is the energy loss per unit length, given by the Bethe-Bloch equation, see Subsection 2.4.1. The ionization energy to produce one electron-hole (e-h) pair in diamond is about 13 eV. This value has been determined theoretically by Alig *et al.*, [59] using the scattering rate assumption and the two level approximation. Canali *et al.*, obtained a similar value experimentally [60] by measuring the ratio between pulse heights from a type IIa natural single-crystal diamond and from a silicon surface-barrier detector using α and β particles. The minimum ionizing energy-loss in diamond is about 469 eVμm^{-1} generating about 36 e-h pairs μm^{-1} and is given by:

$$N_{\mathrm{gen}} = D\frac{1}{E_{\mathrm{T}}}\Big(\frac{\overline{dE}}{dx}\Big), \tag{2.5.14}$$

where D is the thickness of the diamond. By applying an external external electric field on the detector, the pair of charge carriers is separated and accelerated in opposite direction towards the electrodes. The total charge induced on the electrodes, N_{ind}, is a fraction of total charge generated in the bulk:

$$N_{\text{ind}} = N_{\text{gen}} \frac{\mu \tau E}{D}, \tag{2.5.15}$$

where μ is the charge carrier mobility, τ is the charge carrier lifetime and E is the steady applied external electric field. It should be noted that N_{ind} is proportional to the product $\mu\tau$ that defines the diffusion length $L_{\text{df}} = (\mu\tau \text{k}_\text{B} T/q)^{1/2}$ and the drift length $L_{\text{dr}} = \mu\tau E$ [61].

The efficiency of the device, η, is given by the ratio of charge induced at the electrodes and the charge generated in the device:

$$\eta = \frac{N_{\text{ind}}}{N_{\text{gen}}}. \tag{2.5.16}$$

Also, the resolution R and the pulse height distribution functions are determined by the quality of the particle detector and the amount of energy loss in the material. This parameter is given by [62]:

$$R = \frac{\sigma}{\langle E \rangle}, \tag{2.5.17}$$

where $\langle E \rangle$ is the mean energy loss or the most probable value of the pulse height of the detector and σ is the variance, which is given by [62]:

$$\sigma = \sqrt{\int_{\text{a}}^{\text{b}} (E - \langle E \rangle)^2 p(E) dE}, \tag{2.5.18}$$

where *p(*E*)* is the probability density function, defined in the interval between a $\leq E \leq$ b.

Minardi *et al.* [62] extended the method of minimum pulse height selection (MPHSM) to test five analytical forms of pulse height distribution functions, namely the Landau, Tube (positive skewness), Gaussian, Pearson and Tube (negative skewness) distribution functions. The Tube distribution function, was named by Minardi *et al.* [62], due to its similarity with the X-ray tube distribution function.

A pulse generated by low-energy heavy ions that stops completely in the medium produces in a silicon surface-barrier detector a pulse height with a Gaussian or Lorentzian distribution function. However, the pulse height distribution function of a detector made of good quality type IIa natural and synthetic type IIa HPHT diamond is asymmetric, as illustrated in Figs. 2.8 and 2.9, and can be described by the tested Pearson's or Tube (negative skewness) distribution functions shown in Ref. [62].

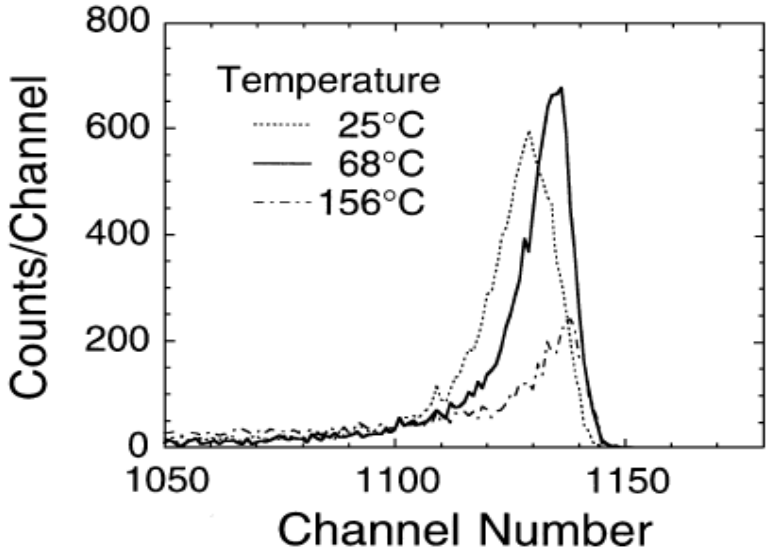

Figure 2.8: Pulse height spectra generated by α-particles with energy of 4.582 MeV. The applied external electric field was of the order of 500 V [20].

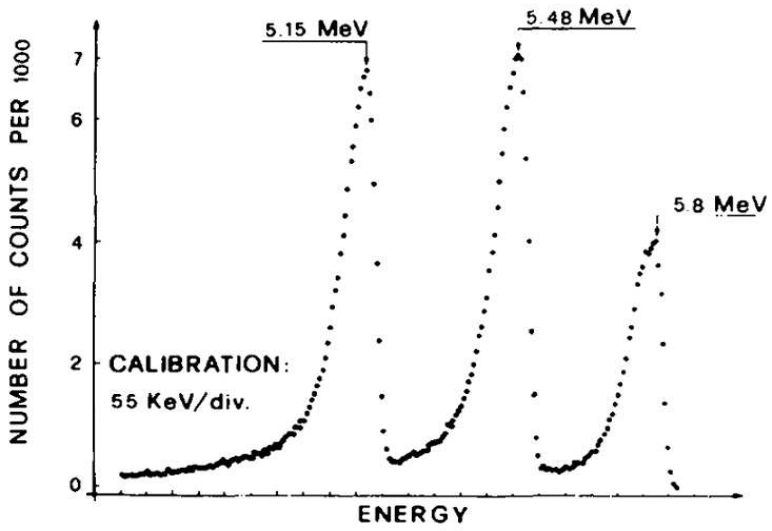

Figure 2.9: Pulse height spectra s generated by α-particles from three mixed nuclide source, in a diamond detector made of a good quality single crystal type IIa natural diamond, [60].

For particle detectors made of single crystal diamond with significant concentrations of trapping impurities, such as the type Ib and poor quality natural type IIa diamonds, the pulse height spectra can be described by the tested Tube (positive skewness) distribution functions. The tested Tube (positive skewness) distribution is given by [62]:

$$P(E) = \mathrm{A}\Big(\frac{E_{\max}}{E} - 1\Big)\exp\Big(-\frac{\beta}{E}\Big), \tag{2.5.19}$$

where A is the normalization constant and β is the variance parameter for this distribution.

2.5.4 Time properties of semiconducting detector

Time properties of a semiconducting detector comprise of the diffusion time, τ, of minority carriers and the dielectric relaxation time, τ_{r}, of the device. In an intrinsic semiconducting material, where $\tau > \tau_{\mathrm{r}}$, the injection of minority carriers into the semiconductor will result in a change of quasi-Fermi level [28, 61, 63]. Thus holes, the majority carriers, will rapidly respond to neutralize the minority carriers so that the equilibrium of the device is restored. The characteristic time for this process is the relaxation time τ_{r} and is given by [28]:

$$\tau_{\mathrm{r}} = \epsilon \frac{1}{\sigma} = \rho\epsilon, \tag{2.5.20}$$

where σ is the conductivity, ϵ is the dielectric constant of the medium and ρ is the resistivity of the material. The above relation is also obtained through the time constant RC of the semiconducting device, where τ_{r} is defined as the rise time of the semiconductor.

After equilibrium is attained the recombination process between electrons and holes will proceed until the law of mass action is restored. The characteristic time for the last process is known as the charge carrier lifetime τ. Using the Hecht function one can extract the life time of the minority carriers as a function of the conduction process in the device. For a device in which the conduction is performed through tunnelling the charge carrier life time is given by [61, 63]:

$$\tau = \frac{\eta_{\mathrm{coll}} d}{\nu_{\mathrm{e}} + \nu_{\mathrm{h}}}, \tag{2.5.21}$$

where $\nu_{\mathrm{e,h}}$ is the electron or hole drift velocity, respectively, η_{coll} is the charge collection efficiency and d is the thickness of the device.

When the conduction is performed through thermionic emission, the charge carrier life time can be extracted from the following equation [61, 63]:

$$\eta_{\mathrm{coll}} = \frac{\nu_{(e,h)}\tau_{(e,h)}}{d}\left(1 - \mathrm{e}^{\frac{-\mathrm{d}}{\nu_{(e,h)}\tau_{(e,h)}}}\right)\ \tanh\left(\frac{V}{2\mathrm{n}V_{\mathrm{T}}}\right) \tag{2.5.22}$$

where V is the steady applied bias voltage on the device, V_{T} is the thermal voltage due to motion of the charge carriers and n is the quality factor of the device. The drift velocity, $\nu_{(\mathrm{e,p})}$, is also expressed in terms of the charge carrier mobility [61]:

$$\nu_{(e,h)} = \frac{\mu_{(e,h)}E}{1 + \frac{\mu_{(e,h)}E}{\nu^{\mathrm{sat}}_{(e,h)}}}, \tag{2.5.23}$$

where $\mu_{(e,h)}$ is the mobility of electrons and holes, respectively, E is steady the applied external electric field, $\nu^{\mathrm{sat}}_{(e,h)}$ is the saturation velocity for electrons and holes, respectively. The ratio $\mu_{(e,h)}E/\nu^{\mathrm{sat}}_{(e,h)}$ is dependent on the value of E, concentration of impurities and on the density of defects.

The relationship between the life time of the minority carriers and the concentration of impurities is obtained using the following equation [61]:

$$\frac{1}{\tau} = \sigma_{\mathrm{e}}\nu_{\mathrm{th}}N_{\mathrm{gap}}, \tag{2.5.24}$$

where σ_{e} is the trap capture cross-section, ν_{th} is the thermal drift velocity and N_{gap} is the midgap carrier concentration.

Chapter 3

Spectroscopic Characterisation of Diamond

3.1 Introduction

The quality of natural and synthetic diamonds was assessed with respect to the presence of defects and impurities, and their concentrations and features. For this, several spectroscopic techniques such as birefringence topography, micro-Raman scattering, X-ray white beam topography, electron spin resonance (ESR), scanning electron microscopy (SEM) and the UV-cathodoluminescence topography have been employed. It should be noted that different types of defects and impurities are introduced during the synthesis process. A brief description, therefore, of the HPHT synthesis method is given, as to provide an insight into the solid state chemistry present during the diamond growth.

3.1.1 Growth process of synthetic diamonds

The high pressure and high temperature (HPHT) conditions required for synthesis of diamond are defined by a linear expression [2]:

$$P_{\text{equilibrium}} = 1.26 + 0.0025\,T\ (\text{GPa}). \tag{3.1.1}$$

This expression is applicable at temperatures above 1500 K and pressures of about 5 GPa. The synthesis process of diamond in HPHT environment, as detailed in Ref. [2], can be performed using two methods; the phase difference method, shown in Fig. 3.1 and the temperature gradient method, shown in Fig. 3.2. Growth of crystals of better quality is achieved using the second method. The temperature gradient

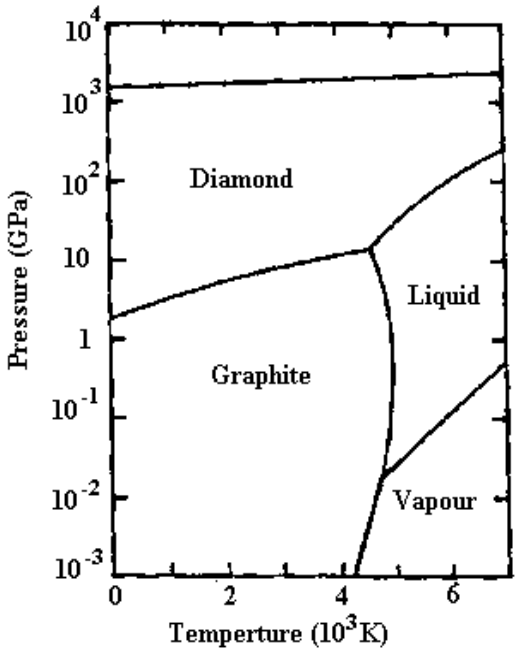

Figure 3.1: Pressure-temperature phase diagram of carbon [64]

method, given by the slope of the line of the solubility of carbon versus temperature ($\Delta C(\Delta^{-1}T)^{-1}$) as shown in Fig. 3.2, offers more stability during the synthesis process. The required supersaturation is maintained, resulting in an uniform growth rate of diamond. Three components are used in the synthesis of diamond in HPHT environment; the diamond seed, the carbon powder and the solvent/catalyst, which

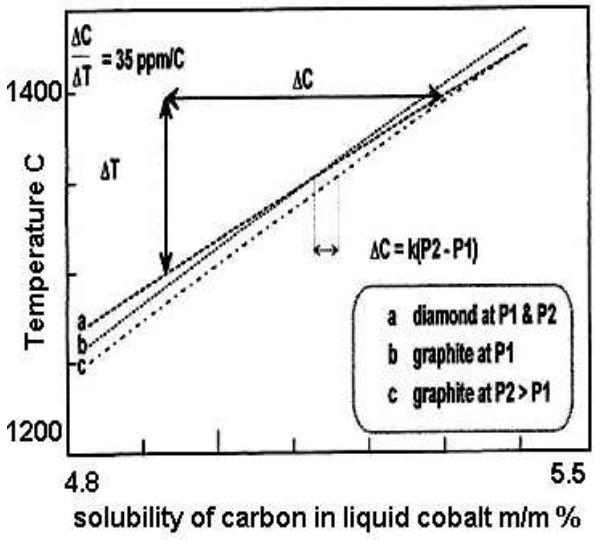

Figure 3.2: The solubility of carbon in solvent/catalyst at high pressures for two solid phases, diamond and graphite [2].

corresponds to the liquid cobalt in the temperature gradient method. During the temperature-gradient syntheses process [2] the source of carbon is placed on the upper end of the liquid cobalt pool at higher temperature and the seed crystal is placed on the lower end, at low temperature. The heating envelope is modified to ensure that the differences in temperature between the upper and the lower end is maintained at values between 20°C and 50°C. Carbon diffuses through the liquid cobalt pool and its dissolution generates temperature fields and a density change. These processes inhibit the formation of convection flows in the molten cobalt. The supersaturation is maintained constant when carbon is in the hotter source zone, at the values of temperature field required for the flux of carbon to be converted at growth rate of 2 to 6 mg/h/seed on the lower seed pad. The growth system is shown in Fig. 3.3 [2].

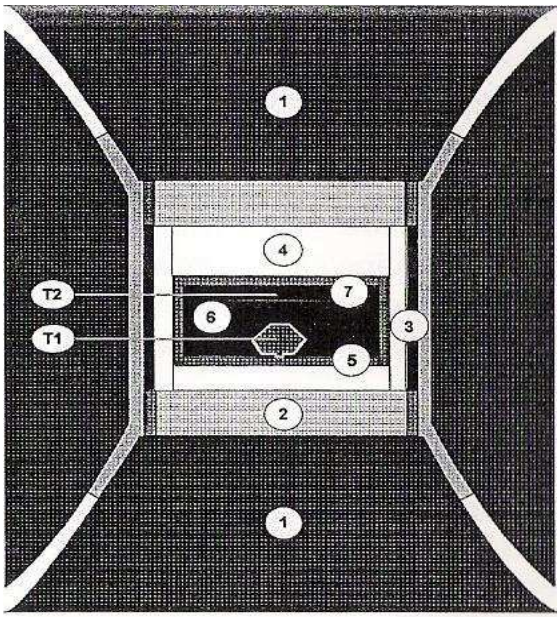

Figure 3.3: Schematic diagram of the HPHT growth system [2]. In the figure (1) being the pressuring anvil, (2) and (4) are the refractory insulators, (3) is the heating envelop, (5) is the seed carrier made of ceramic, (6) is the solvent catalyst volume and (7) the carbon source, T2 and T1 are the temperatures at two height datums T2 exceeds T1 by 20°C- 50°C.

3.2 Birefringence topography

Preliminary evaluation of the crystallographic quality of diamonds is done using birefringence topography. An ideal diamond shows a completely dark image due to almost, or a total transmission of the incident polarized wavelength. If defects are present the image reveals bright areas due to reflection and refraction of the incident wavelength [4].

The characterisation of the bulk was performed using 90° polarized white light, with an angle of incidence normal to the surface of the diamond. Transmission through the bulk depends on the degree of alignment of the crystallographic planes. Thus,

in the ideal case of perfect alignment no reflection or refractive effects of incident wavelength are observed and the image obtained is dark. If misalignments are present, the topographic image will show a mixture of refracted and reflected incident polarized light. The misalignment of crystallographic planes induces different indices of refraction, resulting in a split of the incident wave into two or more waves with different phase velocity.

The intensity of the reflected and refracted waves depends on the density of crystallographic defects. These defects are introduced through the synthesis process, which involves high temperatures, where the subsequent cooling is not uniform throughout the bulk. Topographic images were acquired by using an optical microscope with a lens of 3× magnification and a camera. Three synthetic high-purity type IIa diamonds, samples D2, D3 and D4, grown using the HPHT method, were investigated.

In all samples investigated the topographic images show the presence of strain fields. The contrast due to reflections and refraction shown in Figs. 3.4**a** for sample D2, and 3.4**c** for sample D4, reveals the existence of growth sectors. Figure 3.4**b** for sample D3, shows fractures on the edges that might result from a possible discontinuity in the crystal. The reflected light in this sample also shows the presence of strain fields, which result from misalignment in the entire volume.

One of many different configurations of strains in bulk is shown in the schematic diagram of Fig. 3.5, this configuration being known as growth sectors. The diagram shows schematically the distribution of defects in the bulk of samples D2 and D4.

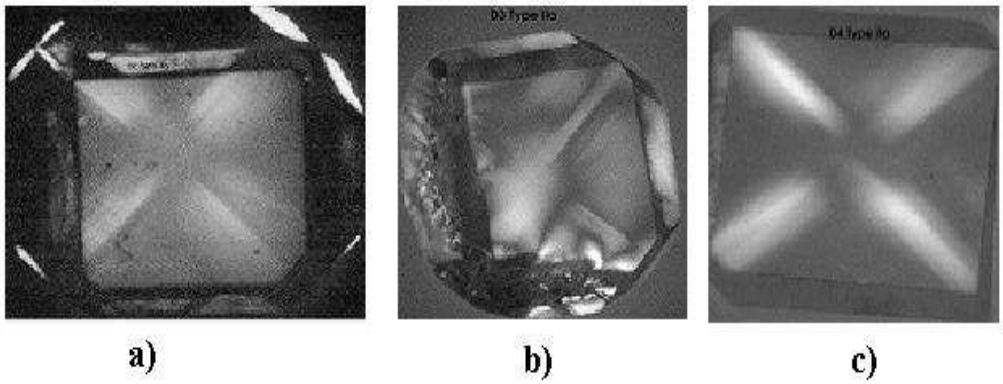

Figure 3.4: In a) and c), samples D2 and D4, strain fields in the form of growth sectors are observed. In b), sample D3, fractures at the edges and strain fields in the center are observed.

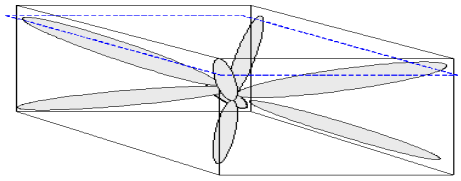

Figure 3.5: One of the possible configuration of strains in a diamond, also known as growth sectors.

In the above configuration, a defect free regime is depicted above the one with growth sectors. This can be sliced and used as a detector grade material. The configuration of strain fields in diamond vary according to the growth conditions and the orientation of the crystal. By selecting a large area of a diamond with good crystallographic quality, one can improve the electronic properties of the material. The improvement is guaranteed if no other defects such as lattice dislocations, stacking faults and platelets are present.

In all type IIa synthetic HPHT diamonds analysed there are strain fields and in two samples the strains have the configuration of growth sectors. The variation in

the intensity of the refracted incident polarized light is probably a result of other crystallographic defects that could not be resolved with the technique applied. The images obtained show that it is possible to obtain sections of diamond of good crystallographic quality where the intensity of the refracted light is weak (see sample D2). It should be noted that the birefringence topography technique used could only resolve the strain fields.

3.3 X-ray topography

X-ray topography is an analytical imaging technique for crystallographic defects by means of X-ray diffraction [66]. For this type of analysis the sample under investigation is separated in two parts; the surface and the bulk. The surface is characterized using reflection (Bragg) geometry, whereas the bulk is characterized using transmission (Laue) geometry. In order to produce topographic images, the X-rays illuminating a crystal diffract in different directions and the image is formed from wave fields interfering with one another. The resolution of the image obtained is determined by the product of the diffraction vector and the average local displacement [67].

When transmission Laue geometry is applied for bulk characterization regarding the crystallographic quality of samples, the waves diffracted are observed on a position sensitive detector as spots, also known as Laue diffraction spots. The intensity and shape of these spots are dependent on the quality of the crystal under investigation. Thus, in a perfect crystal, diffracted waves will produce Laue diffraction spots of

uniform intensity. The position of Laue diffraction spots is given by the Bragg equation

$$\frac{\mathrm{hc}}{E} = \lambda = 2d \sin \Theta_{\mathrm{B}}, \tag{3.3.1}$$

where Θ_{B} is the Bragg angle, d is the spacing of the crystal planes, h is Planck's constant, c is the velocity of light and E is the energy of the incident X-ray beam.

When crystallographic defects are incorporated the incident waves will decouple at defect site, creating new wave fields. This will change the appearance of the diffracted image. Each Laue spot represents a spatial distribution of diffracted intensity due to the variation in lattice spacing, Δd. Using this technique, crystallographic defects such as dislocations, platelets, growth sectors and staking faults can be observed [67].

The source of X-rays used to characterise the diamonds under investigation was provided by the insertion devices of a third-generation synchrotron storage ring, which stores electron energies up to 6 GeV, at the European Synchrotron Radiation Facility (ESRF). The X-ray polychromatic beam, with energies ranging from 6 keV up to 50 keV, is generated by synchrotron radiation in an undulator and bunched into a narrow (1%) fundamental band and its harmonics. The samples, oriented to satisfy the Bragg condition, were tested with a collimated white synchrotron X-ray beam in the topography beam line ID-19 of the ESRF. The image produced by a diffracted beam was recorded in a detector (photographic film) oriented at a scattering angle of 2Θ.

For this experiment three type IIa ultra-pure synthetic single crystal HPHT diamonds were investigated. The transmission topographs of all samples investigated exhibit defects such as dislocations, strain fields, staking faults and platelets. These are shown for samples D2, D3, D4 in Figs. 3.6, 3.7 and 3.8. The topographic image

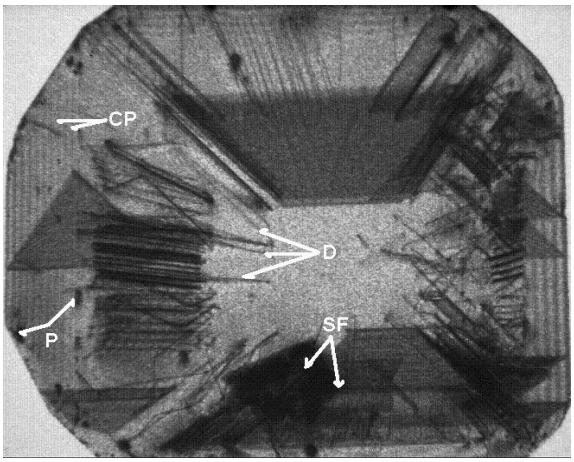

Figure 3.6: The topographic image of sample D2, shows crystallographic defects such as staking faults (SF), dislocations (D), platelets (P) and crystallographic planes (CP). The center of the diamond is a region with less crystallographic defects.

of the sample D2 shown in Fig. 3.6 exhibits a lower density of crystallographic defects and is, therefore, a good candidate for electronic characterisation. The top part of the sample shows evidence of better crystallographic integrity and therefore could be sliced off and used as a prototype for further analysis of its electronic properties with respect to applications.

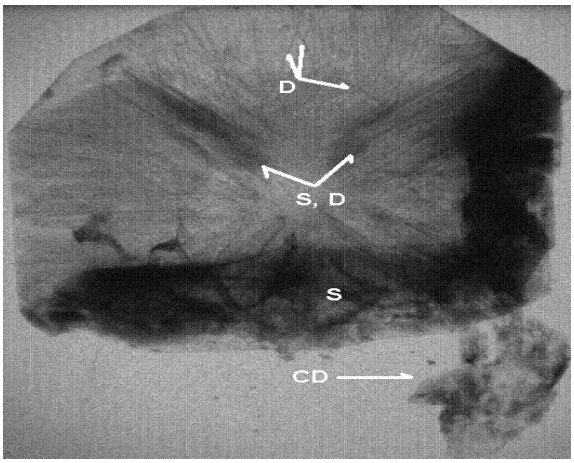

Figure 3.7: The bulk of the sample D3 is characterized by the dislocations (D) and strains (S) in form of growth sectors. At edge there are strains and this region contains fractures, due to crystallographic discontinuity (CD).

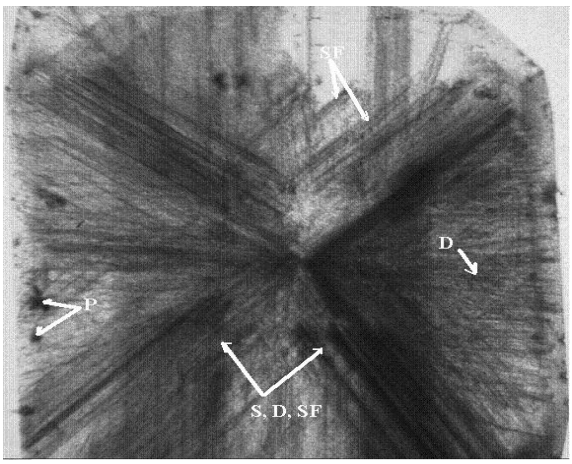

Figure 3.8: The sample D4 is characterized by dislocations (D), stacking faults (SF), platelets (P) and strains (S).

3.4 SEM and XPS surface characterisation

The surfaces of different diamonds used were investigated using scanning electron microscope (SEM) and the X-ray photoelectron spectroscopy (XPS). Characterisation was aimed at assessing the morphology in terms of roughness and type of surface chemical composition, after cleavage, polishing and cleaning procedures. The roughness of the surface after treatment in a hydrogen plasma was also investigated. A smooth surface ensures better quality of metallic contacts applied, reducing in this way the effect of space charge and/or leakage current.

3.4.1 Sample preparation and cleaning

After the synthesis process, diamonds are shaped and the preparation of the surface takes place. This involves cleavage, polishing, acid etching and ultrasound cleaning procedures. Cleavage is performed with a blade coated with a diamond paste or by using a laser ablation [68]. Diamond is sliced along a plane vertical to the growth direction of the material. If crystallographic defects are present in the bulk of the crystal they will propagate and extend to the surface [68, 69]. Cleavage is followed by the polishing process using diamond powder. The polishing powder used consisted of grains with size ≤ 0.1 μm. The use of a diamond powder with fine grains ensures a smooth and uniform surface, with approximate roughness of $\ll 1$ μm and even ≤ 0.1 μm. Fine polishing of a cleaved surface is also dependent on the crystallographic orientation of the material [68, 69].

A smooth surface is of great importance for a perfect and uniform metallic deposition. On rough and damaged surface the recombination velocity of charge carriers is high and exhibits carrier injection resulting in reasonable ohmic contacts, Ref. [70]. This will increase the tunneling probability, a non desirable effect as it leads to an increase in the leakage current at high applied external electric fields. During the polishing and cleavage procedures graphite is formed on the surface which is removed by cleaning the samples for one hour in a mixture of three strong inorganic acids, namely, perchloric ($HClO_4$), sulphuric (H_2SO_4) and nitric (HNO_3) acids in a ratio of about 1:4:3 [71]. After this cleaning procedure the samples are rinsed in deionised water to eliminate any remaining acid. The final procedure is the cleaning of the samples in ultrasound bath of isopropanol, of 99.9% purity, for 10 min to remove any remaining debris [71].

3.4.2 Chemical analysis of the surface

To determine the chemical composition of a polished surface of a diamond [72, 73], the X-ray photoelectron spectroscopy (XPS) technique was applied. X-rays were selected to interact in the surface or in the near surface regions. During the interaction atoms on the surface are ionized. Photoelectrons are generated from the core level and move through the surface and near the surface of the assessed material. The interaction between the photon X-ray and the atom on the surface or near surface region is given by the energy conservation relation

$$E_{\mathrm{ph}} + E_{\mathrm{atom}} = E_{\mathrm{iatom}} + E_{\mathrm{k_e}}, \tag{3.4.1}$$

where E_{ph} is the energy of the incident photon, E_{atom} is the energy of the neutral atom, E_{iatom} is the energy of the ionized atom and $E_{\mathrm{k_e}}$ is the kinetic energy of the photoelectron released.

The identification of chemical composition is done by measuring the energy of the photoelectron released, which is equivalent to the difference between the initial and the final states of the atom on the surface. This energy is known as the binding energy and is a property of the particular element. The injection of electrons as a function of depth is given by [74]:

$$\lambda(E_{\mathrm{AX}})\cos\theta, \tag{3.4.2}$$

where $\lambda(E_{\mathrm{AX}})$ is the inelastic mean free path of the characteristic XPS electrons, with energy $\mathrm{E_{AX}}$ from level X of element A. For such experiments the energies of X-rays were varied between 0.10 keV up to 1.00 keV.

The first peak on the XPS spectrum of a polished sample occurs at 231 eV and results from contamination from the sample holder during the assessment. The second peak occurs between the graphite region, about 284.2 eV [75], and the diamond region, about 285.2 eV [75], which implies that the peak is a mixture of graphite and diamond. The presence of graphite on the surface results from contamination in the measuring system used in this assessment.

Further analyses prove that the graphite, present in the peak, is not a native impurity. The current-voltage characteristic of this surface shows a rectifying behaviour

when contacts made of Ti are deposited in a vacuum of about 10^{-7} mbar, and not annealed. This is a very reactive material in presence of a graphite a layer. When titanium carbide forms the current-voltage characteristics shows ohmic behaviour. The occurrence of an oxygen peak at about 531 eV [72] is also shown in Fig. 3.9. Chemical treatment after polishing has introduced a significant degree of oxygen surface termination (of the dangling bonds) as seen from the XPS spectrum.

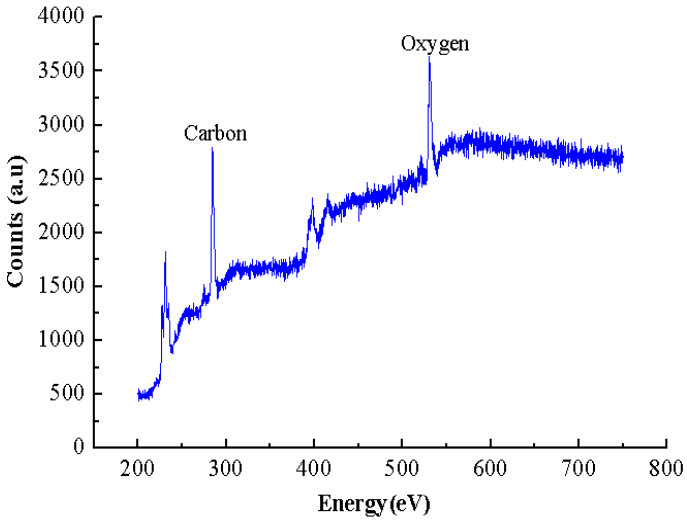

Figure 3.9: The XPS spectral line of a newly polished surface of a diamond. In the spectrum the carbon peak on the surface is 281.80 eV and the oxygen peak is 531.00 eV.

3.4.3 Surface morphology

In an electron microscope an accelerated electron beam is focussed and rastered over the sample by means of an acceleration voltage of several tens of kV, focussing optical elements (Einzel lenses) and scanning electrostatic plates accordingly. The position of the electron beam, determined by the voltage on the scanning plates, is registered

via computer control. The interaction between the electrons and the surface of the sample results in the production of backscattered and secondary electrons. Electron and X-ray detectors detect the backscattered X-rays and secondary electrons. The correlation with respect to the registered beam position is established. In this manner imaging of the rastered area is achieved. The following relation determines the spatial resolution of the microscope:

$$d = 0.61\frac{\lambda}{\sin\alpha_0}, \tag{3.4.3}$$

where λ is the de Broglie wavelength for the electrons and α_0 is the aperture angle of the slits, about 0.34°, yielding d which can be as small as $\sim$ 1 nm.

Two different types of surfaces were analyzed; a conventionally polished diamond, using a scaif and fine powder grit, and a polished surface subsequently etched in a hydrogen plasma. The treatment with a hydrogen plasma was performed under a pressure of about 10^{-5} mbar at temperatures ranging from 400 K up to about 900 K. The exposure time of the samples was varied between 5 min and 30 min. SEM was used in order to assess the surface morphology of the different samples as well as to assess the degree of hydrogen termination for metallization of the surfaces treated in hydrogen plasma. The samples were coated with graphite paste to enhance the conductivity. For this analysis an electron microscope, model Jeol JSM-5600, was used. The energy of the electron beam used for the analysis was 20 keV and the magnification ranged from $\times$3000 up to $\times$30000.

The roughness of a polished surface was found to be $\leq$ 0.1 μm, as shown in Fig.

3.10. Samples treated in H-plasma show roughness $\gg 1$ μm, as shown in Fig. 3.11. Following the treatment in the H-plasma, the surfaces were etched and cleaved lines were exposed. For times longer than 5 min formation of grains start taking place, in which the density and the sizes depend on the exposure time and temperature, as shown in Fig. 3.12. With low magnification it is possible to observe clearly the cleaved planes separated by lines oriented in a parallel direction, as shown in Fig. 3.13. There are fissures with sizes larger than 10 μm and as deep as ≥ 1 μm. Such surface defects/features are detrimental to the quality of surface metallization when applying electrical contacts for electronic applications.

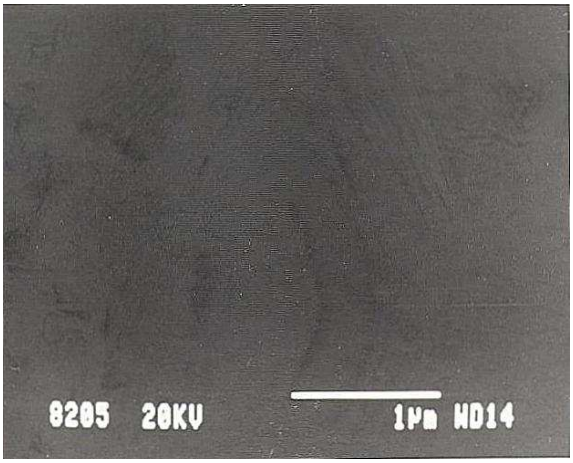

Figure 3.10: SEM image of a surface of a polished diamond, which shows almost no defects.

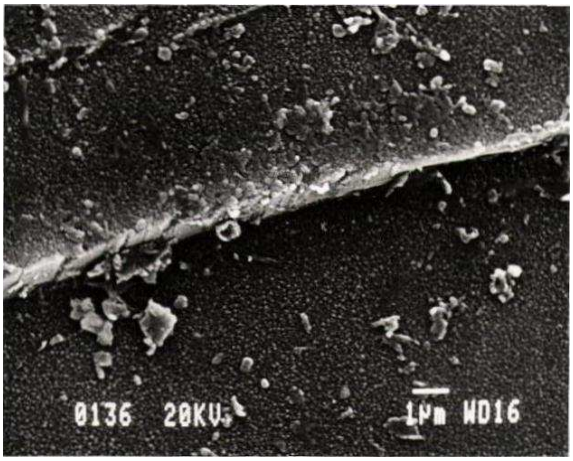

Figure 3.11: Surface of a diamond showing blistering, small granulations and a cleaved line, after being exposed in hydrogen plasma.

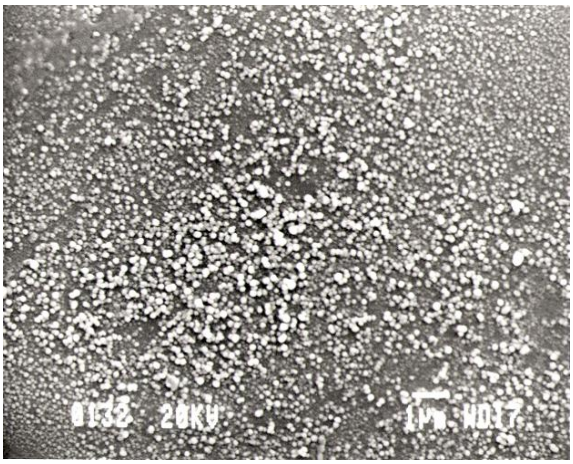

Figure 3.12: SEM image of a diamond surface after having been exposed in hydrogen plasma for a time longer than 5 min. The size of each grain on the surface is ≤ 1 μm.

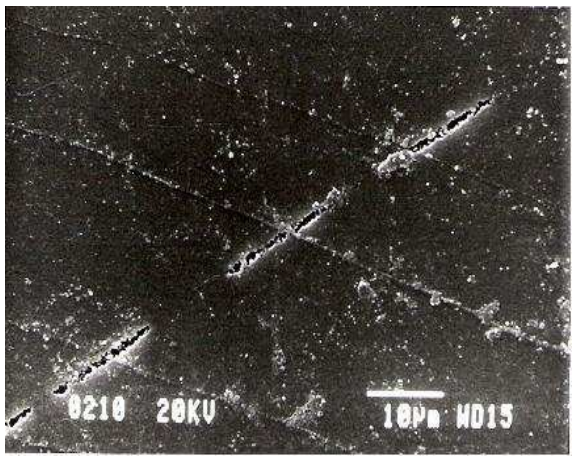

Figure 3.13: With low magnification it is possible to see clearly the direction of cleaved marks with some large fissures in between. These fissures are probably caused by large grains in the polishing powder.

3.5 Raman spectroscopy technique

Raman spectroscopy is a technique applied to investigate the defects in the crystalline structure of the high purity synthetic single-crystal type IIa diamonds investigated in this work. Such defects are characterised by the presence of graphite and amorphous carbon [76]. Of particular importance for the material under investigation was the observation of the role of boron impurity in the Raman signal. Boron is unavoidably introduced in the diamond during the growth process. In a diamond containing boron acceptors with concentrations near and above the Mott transition density the Raman spectrum shows weak signals around 610, 925, 1045, 1375 and 1470 cm^{-1} and a downshift zone-bond center in the Raman peak at wave numbers of 500, 1225, 1230, 1320 cm^{-1} and 1332 cm^{-1} [37, 77]. In a perfect diamond crystal with sp^3 covalent bond structure only the Raman peak is observed at a wave number of 1332.7 cm^{-1} [1].

The interaction of an incident photon with the crystal lattice may result in an outgoing photon with the same incident energy. This elastic scattering interaction is of the Rayleigh-Jeans type, a process frequently observed in nature. Inelastic scattering processes will result from interactions between the incident photon and the crystal lattice, in which longitudinal and acoustic modes maybe involved. This implies that the process takes place with absorption of energy by one of the interacting components. The interaction is said to be inelastic and the following relation gives the selection rule [27]:

$$\overrightarrow{k} = \overrightarrow{k}' \pm \overrightarrow{K}, \tag{3.5.1}$$

where $\pm \overrightarrow{K}$ is the creation or annihilation operator of the phonon modes, and $\overrightarrow{k}$ and $\overrightarrow{k}'$ are the operators of the wave vectors of the incident and scattered photons, respectively. The creation or annihilation of a phonon is also given by [27]:

$$\hbar\omega - \hbar\omega' = \pm\hbar\Omega, \tag{3.5.2}$$

where $\hbar\omega$ and $\hbar\omega'$ are the energies of the incident and the scattered photons and $\pm\hbar\Omega$ is the energy of the phonon created or annihilated. The incident photon may be scattered to a shorter or longer wavelength depending in the direction of the absorbed energy.

The scattering of the incident photon to a shorter or to a longer wavelength gives rise to the anti-Stokes or to the Stokes line, respectively. The difference between

the incident and the scattered photon is the Raman shift, for which the following relation gives the intensity [27]:

$$I \propto \frac{1}{\frac{(2\hbar\sum_{\mathrm{k}}\frac{1}{\tau_{\mathrm{k}}})^2}{4} + (\hbar\omega' - \hbar\omega \pm \hbar\Omega)^2}, \tag{3.5.3}$$

where $2\hbar\sum_{\mathrm{k}}\frac{1}{\tau_{\mathrm{k}}}$ is the width of the Raman line and τ_{k} is the life time of the phonon.

3.5.1 Experimental procedures and results

The Raman facility used employs a laser model Jobin Yvon T6400D. Here, the setup illustrated in Fig. 3.14 is composed of a microscope with a lens of 20× magnification to increase the amplitude of the signals, a charge coupled device (CCD) for detection of single photons, a source of electromagnetic waves and an Argon Dye Laser (Model 375). The laser wavelength used was $\lambda_{\mathrm{Ar}} = 514.5$ nm, with corresponding energies of about 200 mW and 400 mW. A mercury lamp with wavelengths $\lambda_{\mathrm{Hg}_1} = 546.0735$ nm and $\lambda_{\mathrm{Hg}_2} = 576.969$ nm was used for calibration. The calibration lines used in the experiment, obtained from a spectrometer, come from the difference between the λ_{Ar} line and the $\lambda_{\mathrm{Hg}_{1,2}}$ lines.

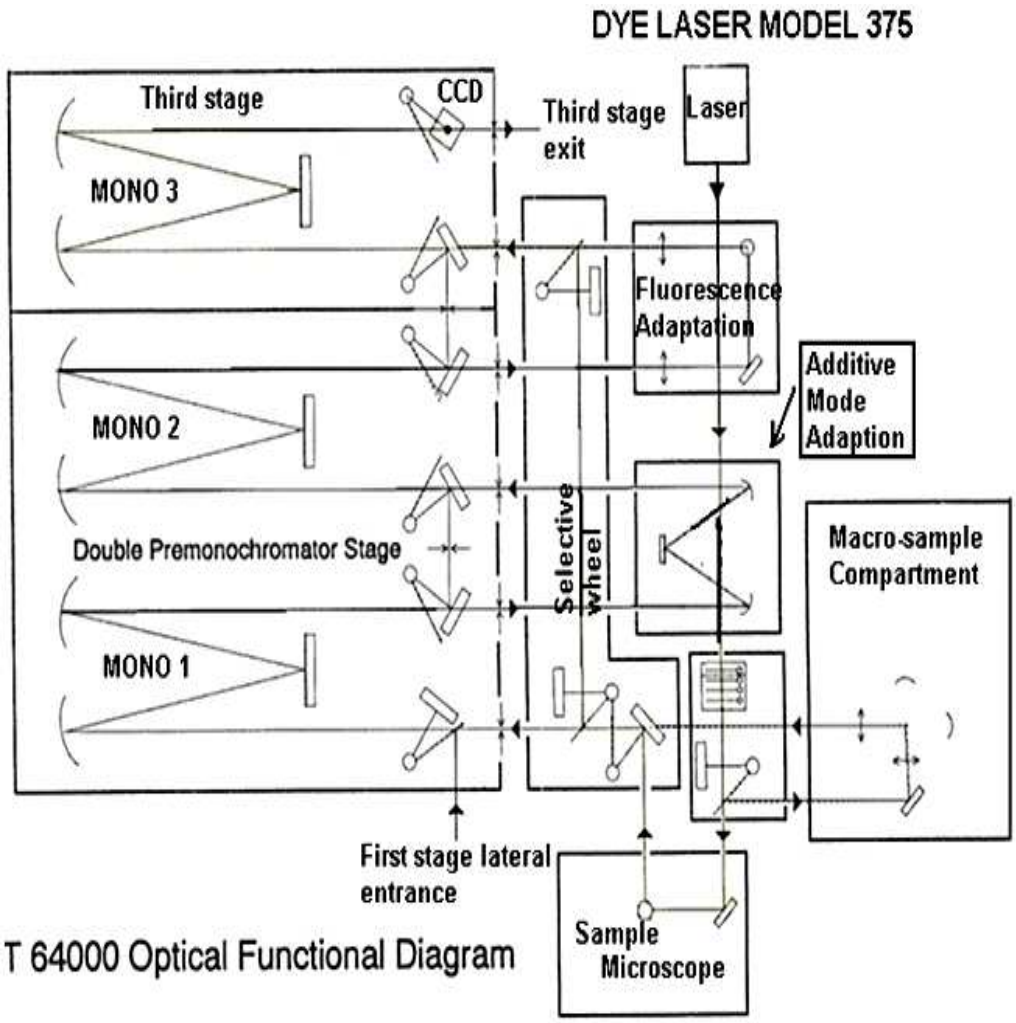

Figure 3.14: Raman measurement setup used in this experiment.

The Raman scattering signal from all ultra pure HPHT synthetic single-crystal type IIa diamonds is a narrow Lorentzian line. The peak position of the line shift in each diamond was 1332.72 cm^{-1} in sample D2, 1332.73 cm^{-1} in sample D3 and 1332.76 cm^{-1} in sample D4. The average full width at half maximum (FWHM), taking into account the errors of the shift and the slits apertures, was 1.91 cm^{-1}. Theoretically, the Raman shift in a diamond occurs at 1332.7 cm^{-1} with a FWHM ranging from 1.5 cm^{-1} to 4.0 cm^{-1}. Sample D2 showed slightly higher peak intensity, while samples

D4 and D3 showed smaller intensity as depicted in Figs. 3.15, 3.16 and 3.17. There is a variation in the peak intensity, regarding sample D3 due to morphological structure of the surface at the edge region and the near surface regions.

Table 3.1: Raman scattering results

Sample	Raman Shift (cm^{-1})	FWHM (cm^{-1})
IIa Synthetic (D2)	1332.72	1.94
IIa Synthetic (D3)	1332.73	1.84
IIa Synthetic (D4)	1332.76	1.95

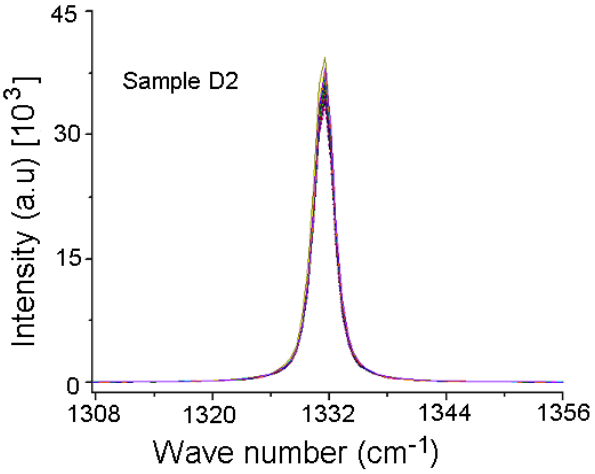

Figure 3.15: The intensities of Raman line in all regions of the surface scanned on the sample D2 do not show any significant variations.

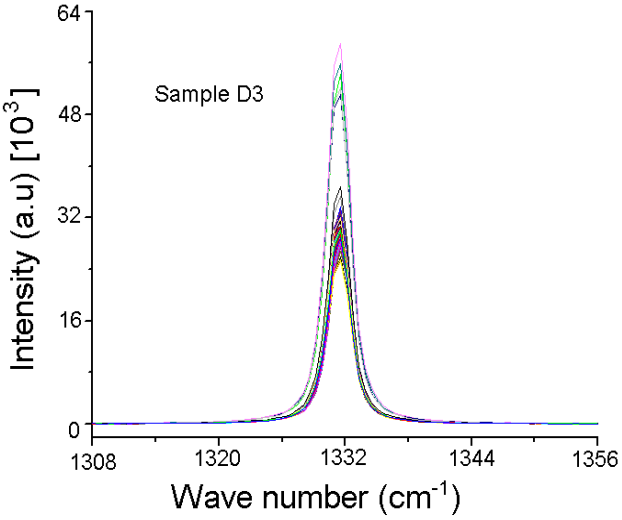

Figure 3.16: The variation of the intensity for sample D3 is due to the crystal discontinuity that affects mainly the edge region of the diamond.

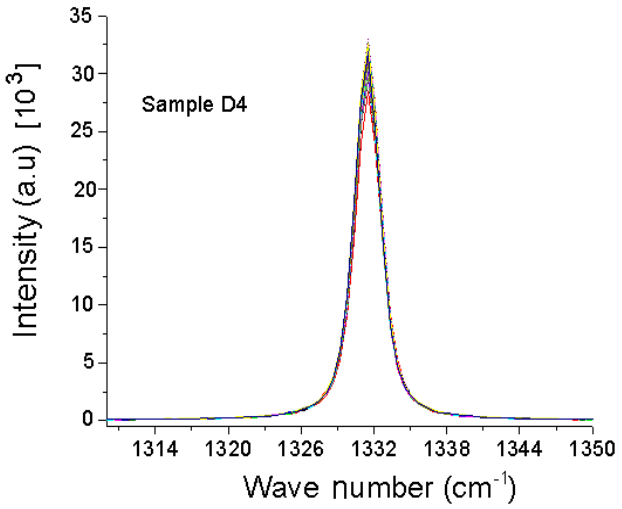

Figure 3.17: All regions scanned with photons in the sample D4 are almost of the same intensity.

In summary, the Raman lines obtained from the three ultra-pure synthetic HPHT diamonds and the corresponding values at full widths at half maximum are given in Table 3.1, and fall within the known values in the literature (e.g.) Ref. [1]. Additional lines due to presence of boron impurity are not observed as seen in the appendix Fig. A6 which means that the concentration of this impurity is negligible.

3.6 UV cathodoluminescence topography

Using this technique the type of impurities and defects are classified by the wavelengths emitted during the de-excitation of excited centers introduced by the impurities and defects in the bulk [78, 79, 80]. When a non-relativistic beam of electrons, of about 20 keV, is incident on a diamond electron-hole (e-h) bound states known as excitons will be generated. These can be classified as a tightly bound state (Frankel exciton) and a loose bound state (Warnnier exciton) [27]. The tightly bound state occurs mainly in a pure crystal with no concentration of impurities and with the linear combination of a perfect lattice [27]. The de-excitation of a tightly bound exciton occurs in the region of the lattice near the conduction band minima and above the valence band maxima in which a photon is released. During the de-excitation of a tightly bound exciton a lattice vibration mode may occur [56].

If small concentrations of impurities are present an electron may be bound with the hole of the impurity. In this case, the radius of this bound state is larger than the lattice parameter of the crystal [56]. The de-excitation occurs with an emission of a

photon and is always accompanied by vibrational modes. During the de-excitation the intensity of photons emitted is a function of frequency of the excited center and is given by [56]:

$$I(T) = \int_0^\infty \psi_{\mathrm{T}}(\nu)\mathrm{d}\nu, \tag{3.6.1}$$

where ψ_{T} defines the luminescence spectrum, ν is the frequency of photons emitted and T is the temperature of the medium.

Identification of defects and impurities is also done by analyzing the topographic image of the sample during the de-excitation. The wavelength emitted is a signature of each impurity and defect [81]. In the presence of a high density of defects and impurities the de-excitation releases a photon is in the infrared region. For a high purity diamond the emitted photon is in the UV-region and the topographic image of the sample is dark.

The most important impurities considered in this work were the SSN and boron acceptors. These yield for the presence of SSN concentrations an emission of a yellow luminescence [1] and for boron acceptors an emission of blue luminescence [1]. However, if the compensation of these two impurities in bulk occurs the topographic image of the diamond is dark.

3.6.1 Experimental procedure and results

An electron beam of about 25 keV is generated in a cathode. The electrons are then accelerated at different applied potentials inside an evacuated anode and interact

with the samples. In order to produce topographic images, a microscope with a camera to record the luminescence of the sample was used. Four samples were selected for this investigation, sample D2a sliced from the top of sample D2, a natural type IIa diamond and two single-crystal diamonds of type Ib with 46 ppm and 215 ppm of SSN, respectively. The natural type IIa diamond and the type Ib diamonds are characterized for control purposes.

The type IIa ultra-pure HPHT diamond sample D2a is a transparent material, the natural type IIa diamond, used in this work, has a slightly brown transparent colour and it belongs to a very rare type of natural diamonds. The two single crystals of type Ib diamonds with different concentrations of SSN, both have a yellow colour with different intensities. The thickness of sample D2a was about 460 μm, for the natural type IIa diamond the thickness was about 670 μm and for the two single-crystal diamonds of type Ib the thicknesses were approximately 420 μm and 600 μm, respectively.

The cathodoluminescence topography of high-purity synthetic type IIa HPHT diamond showed a dark blue luminescence in the center region as seen in Fig. 3.18. The blue luminescence becomes more intense at the edge of the material. It is assumed that the intensity of the luminescence in different regions of the sample varies as a function of the concentration of uncompensated boron impurity. Crystallographic defects were not observed in this sample using this technique, and thus were assumed to have very low density. On the other hand, in a type IIa natural diamond, see Fig. 3.19, the topography showed a purple-blue luminescent colour. In addition,

the slight brown colour results from the presence of dangling bonds. Therefore, the luminescent colour shown by this material is a mixture of luminescence from uncompensated boron acceptors and from the dangling bond or from uncompensated boron acceptors in a different excited state.

The type Ib diamond, see Fig. 3.20, with 46 ppm of SSN shows dark yellow luminescence at the center, mixed with a slightly yellow and bluish luminescence. This results from a relatively high factor for the compensation of SSN and boron impurities. The edges of the sample are characterised by the presence of yellow and blue bands, which results from a compensating factor. The type Ib diamond, see Fig. 3.21, with a 215 ppm concentration of SSN displayed green bands resulting from emission of vibronic modes due to presence of crystallographic defects. This sample contains high density of defects. In the region with growth sectors there were brown nodes on dark brown and blue backgrounds. These regions are characterised by strains and a high factor for compensation or, more probably, the almost absence of impurities due to the lattice distortions. The impurities in these regions being expelled to other regions of the sample. Also the edges were characterized by a yellow brownish colour due to the high density of SSN.

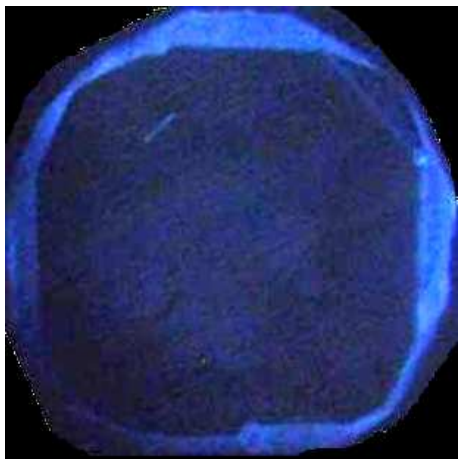

Figure 3.18: In sample D2a the dark blue colour reveals a very low concentration of boron acceptors. The distribution of the intensity is probably a function of compensation in all regions.

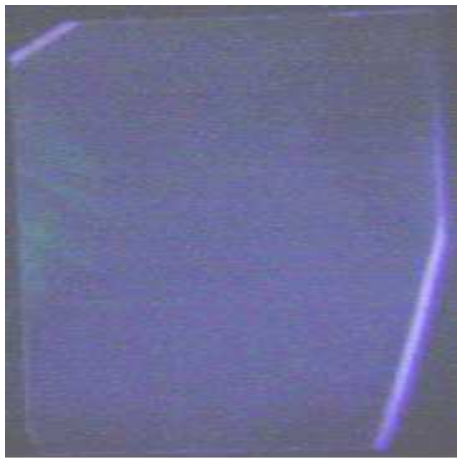

Figure 3.19: In type IIa natural diamond, the purple-blue luminescence might result from different excited states of boron acceptors in bulk or the combination of luminescence emitted by boron acceptors and the luminescence emitted by the dangling bond.

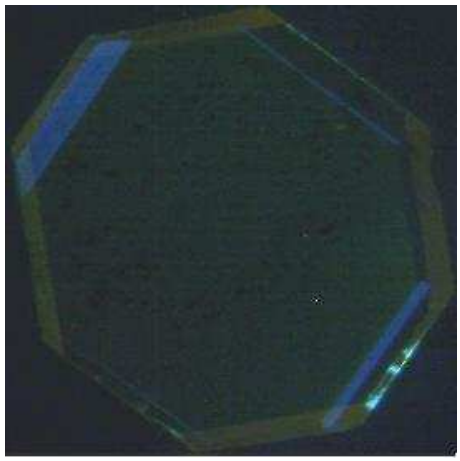

Figure 3.20: The topographic image of type Ib (sample Ib_1) with 46 ppm of SNN, shows a dark colour in the center as a result of high compensation. At the edge there are blue and yellow bands due to low compensation.

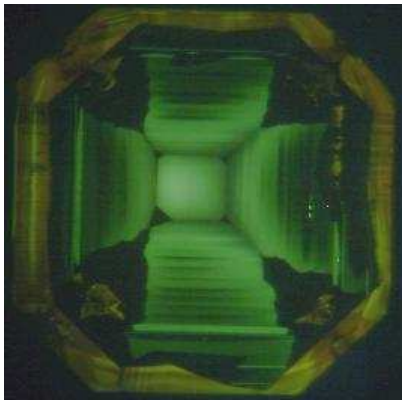

Figure 3.21: The type Ib (sample Ib_2) with 215 ppm of concentration of SSN shows light-green luminescent bands at center as a result of high emission of vibronic modes. The yellow bands at the edge are a signature of high concentration of SSN. There is a high compensation factor of impurities in the region of growth sectors, shown as a dark colour.

3.7 Electron spin resonance (ESR)

In diamond when the concentration of single substitutional nitrogen (SSN) is lower in comparison to that of boron acceptors or when the concentrations of these impurities are at the same level compensation do not occur [17, 82]. On the other hand, extremely low concentrations of boron impurities can hardly be quantified using conventional spectroscopy methods. However, these negligible and non-compensated quantities are enough to alter significantly the electronic properties of a diamond.

The *electron spin resonance* (ESR) technique is employed to determine the concentrations of SSN in high purity synthetic type IIa HPHT diamond and is expected to have an extremely low value. This constitutes an indirect method of roughly estimating the concentrations of boron acceptors, which should be of the same value of SSN impurity or slightly higher. The unpaired electrons generated by the presence of impurities, like in the case of SSN, gives to the material a paramagnetic property. One efficient to detect and determine the concentration of a paramagnetic impurity is the ESR technique. The basic mechanism of this technique lies on the rate of the exchange of energy quanta between the interacting unpaired electrons (dipoles) of the impurity and on their relaxation times [83].

A moving electron generates current and sets up a magnetic moment μ_s. The electron has spin with two-fold degeneracy and the relationship between the spin vector $\overrightarrow{S}$ and μ_s is given by following equation:

$$\mu_s = \frac{g\mu_B}{\hbar}\overrightarrow{S}, \tag{3.7.1}$$

where g is the Landé factor and μ_{B} is the Bohr magnetron. In the proximity of a steady external magnetization vector, $\overrightarrow{H}_0$, the electron experiences a torque, resulting in alignment between $\mu_{\overrightarrow{s}}$ and $\overrightarrow{H}_0$. The electron acquires two projections, (the Zeeman levels), $\overrightarrow{S}_{\mathrm{z}} = \pm\ \hbar/2$, along $\overrightarrow{H}_0$ and the magnetic moment of the spins is given by:

$$\mu_{\mathrm{z}} = \pm\frac{1}{2}\mathrm{g}\mu_{\mathrm{B}}. \tag{3.7.2}$$

The energy of the electron in one of these two projections, as a function of $\overrightarrow{H}_0$, is given by:

$$E = \pm\frac{1}{2}\mathrm{g}\mu_{\mathrm{B}}\overrightarrow{H}_0. \tag{3.7.3}$$

The transition of electrons in the Zeeman energy levels occurs when absorption of a radio frequency wave is observed at a frequency corresponding to the difference between the two energy levels, $\Delta E = E_+ - E_- = \hbar\nu$. This effect is known as electron spin resonance (ESR).

The relative population in the two energy levels, N_+ and N_-, in ESR is described by the Boltzman distribution [83, 85]:

$$\frac{N_+}{N_-} = \frac{\Delta E}{\mathrm{k}_{\mathrm{B}}T}, \tag{3.7.4}$$

where k_{B} is Boltzman's constant and T is the absolute temperature. The dipolar field associated with the magnetic moment is given by [83]:

$$\overrightarrow{H}_{r_{(e-e)}} = \frac{\mu_0}{4\pi}\frac{1}{r^3_{\text{(e-e)}}}\Big[-\mu_{\text{s}} + \frac{3\mu_{\overrightarrow{\text{S}}}\text{r}_{\text{(e-e)}}\text{r}_{\text{(e-e)}}}{r^2_{\text{(e-e)}}}\Big], \tag{3.7.5}$$

where μ_0 is the magnetic moment of the external magnetization and $r_{(e-e)}$ is the distance between the two interacting dipoles. For the same frequency the energy at the same distance is found between E_{dd} and $-E_{\text{dd}}$ [83], where

$$E_{\text{dd}} = \frac{\mu_0}{8\pi}\text{g}^2\mu_{\text{B}}^2\frac{1}{r^3_{\text{(e-e)}}}. \tag{3.7.6}$$

Transitions from lower to upper Zeeman level cease when equilibrium between the two levels occurs. The relaxation times of the interacting dipoles (spin-spin) is designated T_2. Until the equilibrium is reached, transfer of energy between individual spins occurs at a rate of about $1/T_2$.

In diamond the single substitutional nitrogen (SSN) is a paramagnetic impurity, also known as P1 center. For this center $1/T_2$ is given by [84]:

$$\frac{1}{T_2} = \frac{1}{T_{2\text{(P1-P1)}}}. \tag{3.7.7}$$

The shape of the ESR line is given a Gaussian function as described in Ref. [84]:

$$f(H) = \frac{1}{\Delta(2\pi)^{1/2}}\exp\Big(-\frac{(H-H_0)^2}{\Delta^2}\Big), \tag{3.7.8}$$

where Δ is the relation containing the natural abundance of ^{13}C, about 1% in almost all natural diamonds and less in synthetic type IIa diamonds.

The width of the pulse obtained from the shape of the ESR line is found by measuring the maximum and the minimum, as in the case of pulses shown in Figs. A1, A2 and A3. Which is equivalently found by multiplying the term $\frac{1}{\sqrt{\Delta(2\pi)}}$ in the Eq. (3.7.8) with $\frac{\Delta^2}{2}$ [84, 85]:

$$\delta = \frac{2}{\sqrt{\pi}}\Delta, \tag{3.7.9}$$

where $\delta = \sqrt{(1.2 \times 14^{-4}C_e^2 + 0.014)}$ G, C_{e} is the concentration of the SSN and G is the unit of the magnetic field.

For concentrations higher than 10 atomic parts per million (appm) the relationship between the width of the ESR peak and $1/T_2$ is given by [85]:

$$\Delta = (1.2 \times 10^{-4}C_{\mathrm{e}}^2 + 0.014)^{1/2}\mathrm{G}, \tag{3.7.10}$$

and for concentrations less than 10 ppm this relationship is given by [85]:

$$\frac{1}{T_2} = 1.4 \times 10^4 C_{\mathrm{e}}. \tag{3.7.11}$$

For extremely low concentrations where T_2 yields higher values greater than 1 ms, that could be beyond the detectable region of the phase detector used, the ESR line is obtained by sweeping the radio frequency wave through the resonance in a time shorter than T_2. This causes the alignment between of $\mu_{\vec{S}}$ and $\overrightarrow{H}_0$ to occur. This method is called the adiabatic rapid passage (ARP) [83] and was employed in this work.

3.7.1 Experimental procedure and results

ESR spectra were obtained using a X-band spectrometer, model Bruker ESP300E Varian CW. The sample was mounted in a cold finger at liquid nitrogen temperature and placed inside a resonant cavity. The homogeneous and static magnetic field was varied between 0 and 5000 G. The field was modulated by the 100 kHz sweep generator located within the resonant cavity. A phase reference voltage was supplied to a signal phase detector. The sample was then irradiated using the klystron oscillator that produces radio frequency wave. When resonance is obtained from the sample the impedance of the cavity is changed and a signal is reflected to the phase detector. As such, when the rate given by $1/T_2$ is sufficient to produce ESR the concentration of the SSN is obtained by measuring the line width of the spectrum acquired by the detector.

When the ARP method is implemented, the only parameter extracted from the output pulse is the intensity. This parameter is compared with the intensity of a reference sample with a known mass and concentration of SSN. The reference sample used was a type IaA diamond with known concentration of SSN of about 10^{15} cm^{-3} with mass of about 228 mg. This sample contained nitrogen in other forms not sensitive to ESR technique. In order to extract the absolute concentration of SSN, the following equation was used:

$$[\mathrm{SSN}]_{\mathrm{IIa}} = \frac{I_{\mathrm{IIa}}}{I_{\mathrm{IaA}}} \times \frac{m_{\mathrm{IIa}}}{m_{\mathrm{IaA}}} \times \frac{1}{2}[\mathrm{SSN}]_{\mathrm{IaA}}, \tag{3.7.12}$$

where I is the intensity of the resonant pulse, m is the mass of the sample and [SSN]

is the concentration of the single substitutional nitrogen. The units of the output results are given in atomic parts per million [Appm] and are converted into (spins gram^{-1}) or (spins cm^{-3}). The conversion is obtained knowing that a concentration of about 19.9 Appm corresponds to 1×10^{17} spins cm^{-3}. As expected, using the normal ESR technique it was not possible to determine the real concentration of SSN. The signals obtained in all samples investigated fall in the noise region, as shown in Fig. 3.22.

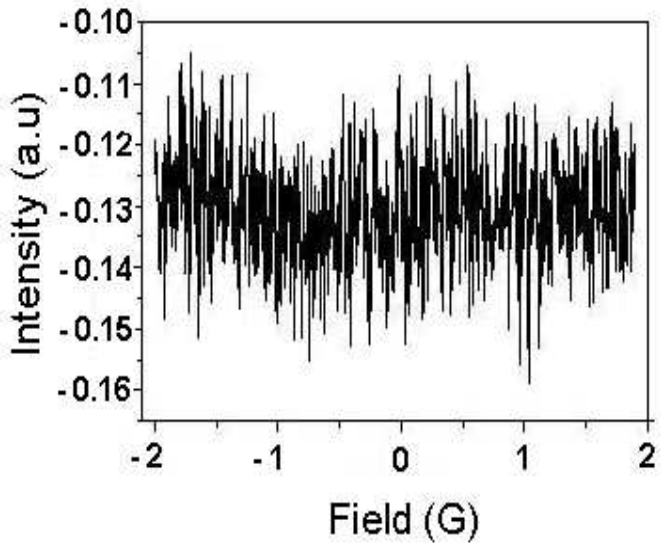

Figure 3.22: A spectrum of a ultra pure type IIa HPHT synthetic diamond acquired using the normal ESR technique.

The results obtained using the ARP method give an average concentration of SSN impurity in synthetic type IIa HPHT diamond of about $\leq 10^{13}$ cm^{-3}. The width, the intensity and the position of the peak are also a function of concentration of the SSN. The narrower the width and the higher the intensity of the peak, the higher the concentration of SSN. In the reference sample the peak intensity, see Fig. 3.23, is about 40×10^{6}, given in arbitrary units (a.u). The position of the most probable

value is 3439.75 G, and the width is 0.25 G.

The results obtained from sample D2, see Fig. 3.24, with a mass of about 79 mg, gives an estimation of concentration of SSN about $\leq 10^{13}$ spins cm^{-3}. The intensity of the peak is about 10×10^{6} in a.u., the position of the most probable resonant value is 3443.75 G and the FWHM is 0.35 G. The width of the peak is ten times larger compared to the reference sample. This implies a long relaxation time for the interacting spins.

The resonant line of sample D3 shown in Fig. 3.25, with mass of about 63 mg, gives an intensity of about $\leq 10\times10^{6}$ a.u. The peak is positioned at 3445.25 G and the FWHM is about 1 G, which means an increase in the relaxation time of the interacting spins compared to that observed in the previous sample. By implementing the Eq. (3.7.12), the concentration of SSN is $\leq 10^{12}$ spins cm^{-3}. On the right hand side of the resonance the baseline shows a long decay time, which suggests the presence of a defect sensitive to the ESR technique. The defect might be correlated to crystalline discontinuity in the bulk which can be observed using other techniques.

For sample D4 shown in Fig. 3.26, with mass of about 59 mg, the concentration of SSN is estimated to be about $\leq 10^{13}$ spins cm^{-3}. The intensity of the peak is about 12.5×10^{6} a.u, the peak position is 3443.75 G and the FWHM is 0.25 G.

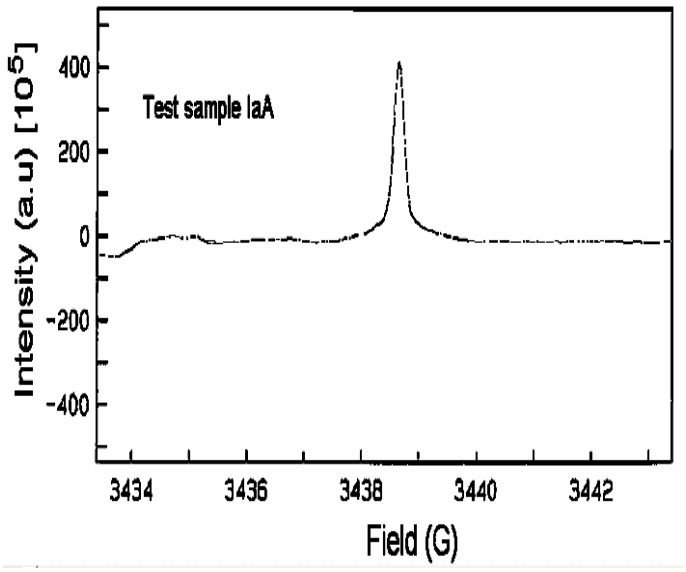

Figure 3.23: The ARP spectrum of the reference sample, type IaA.

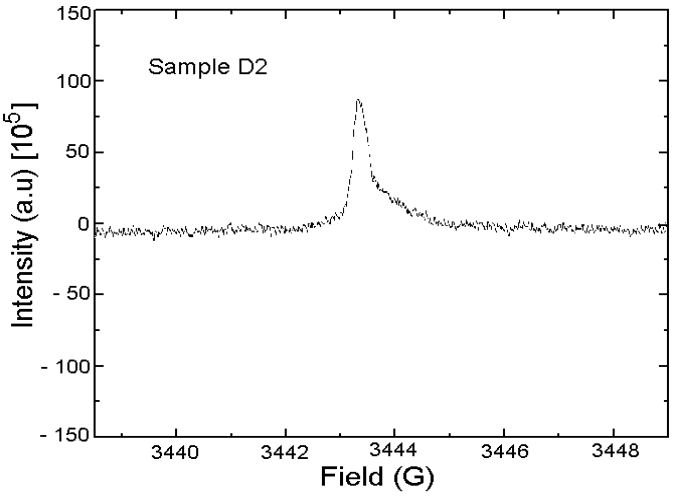

Figure 3.24: The ARP spectrum of sample D2. The estimated concentration of [SSN] is $\leq 10^{13}$ spins cm^{-3}.

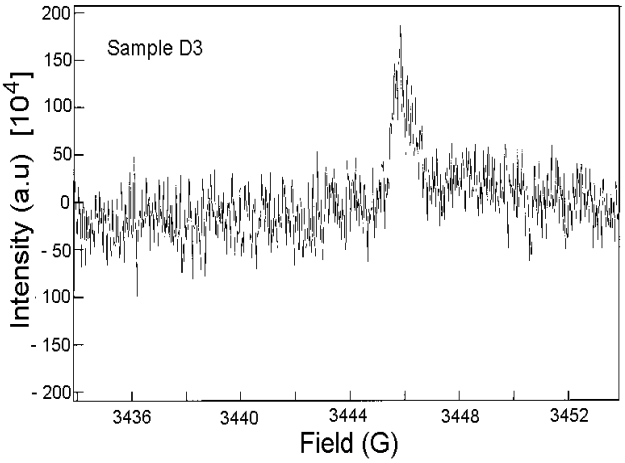

Figure 3.25: The ARP spectrum of sample D3. The estimated concentration of the SSN is $\leq 10^{12}$ spins cm^{-3}.

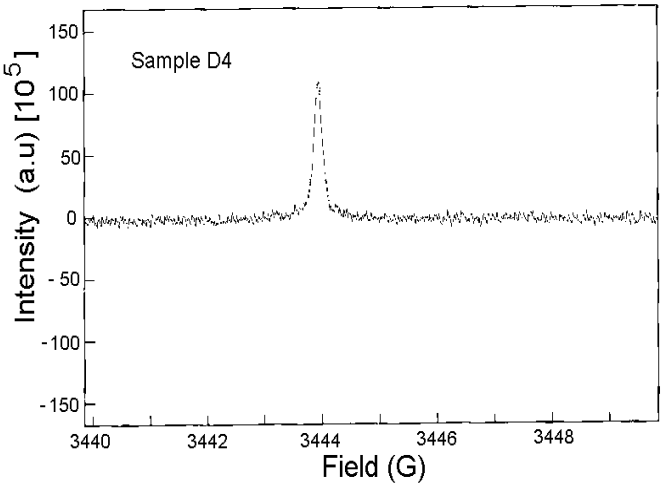

Figure 3.26: The ARP spectrum of sample D4. The estimated concentration of SSN is ≤ 10 ^{13}spins cm^{-3}.

The values of [SSN] in the samples are very low, about 10^{13} spins cm^{-3}. Using the ARP method the peak parameters, such as FWHM, intensity and position, and the concentration of [SSN] are correlated, as shown in Tables 3.2 and 3.3. Sample D3, in which crystallographic discontinuity was observed using other techniques, shows lower concentration of SSN.

Table 3.2: [SSN] as a function of mass and the intensity of the peak, using the ARP method

Sample type	mass (mg)	Peak intensity ($\times 10^6$)	[SSN] ($\times 10^{13}$spins cm^{-3})
IIa HPHT Synthetic diamond (D2)	79.00	10.00	6.85
IIa HPHT Synthetic diamond (D3)	63.00	$\leq$10.00	0.11
IIa HPHT Synthetic diamond (D4)	59.00	12.50	6.40
IaA Natural diamond	288.00	40.00	100.00

Table 3.3: The width and the position of the resonance peak using the ARP method

Diamond	Peak position (G)	FWHM (G)	Peak resolution $\sigma(\times 10^{-5})$
IIa Synthetic (D2)	3443.65	0.35	3.5
IIa Synthetic (D3)	3446.00	1.00	10.0
IIa Synthetic (D4)	3443.75	0.25	2.6
IaA Natural	3439.75	0.25	2.6

Chapter 4

Electronic Characterisations

4.1 Introduction

Two methods of surface metallization for synthetic type IIa HPHT diamonds have been investigated: a) surface hydrogenation, tested in a type IIb diamond and b) the use of a metal with a high work-function as electrodes tested in a synthetic type IIa HPHT diamond. The performance and electronic properties of devices with such contacts were then assessed with measurements using charged particles and UV-laser photons. Of particular concern was the optimization of the amount of applied external electric field on the detector, which leads to an improvement of the charge collection properties of the device.

The properties of Schottky and ohmic contacts were investigated in type Ib diamonds with respect to concentrations of SSN of 46 ppm, 100 ppm, 150 ppm and 215 ppm. For this purpose, the current-voltage characteristics were analyzed and the properties of electric pulses generated by a UV-laser and by α-particles were investigated. In this chapter the results from the deep-level transient spectroscopy (DLTS) used to characterise the synthetic type IIa HPHT diamond are also presented.

4.2 Surface metallization of the samples

In order to measure the electronic properties of diamond, electrodes were deposited on the surfaces in parallel plate geometry using an electron beam (e-beam) system [86, 87] in an evacuated chamber. The level of vacuum during the metal evaporation and deposition on the surface of the diamonds is of particular importance for the type of conduction required. For example, if tunnelling conduction is required then a high vacuum is needed, while a low vacuum is preferred for conduction through thermionic emission.

4.2.1 Ohmic contacts

Ohmic contacts are commonly obtained for diamond by depositing layers of titanium (Ti), platinum (Pt) and gold (Au) [73, 88]. The deposition ratio used in this work was about 200 Å of Ti, 300 Å of Pt and 1000 Å of Au. Deposition was performed in a chamber coated with Ti at a starting vacuum level of about 1×10^{-9} mbar. Such a high vacuum is required in order to minimize the oxygen content on the diamond surfaces. It should be noted that the binding energies depending upon the ....involved between titanium and oxygen (TiO_2) are 530.67 eV and 531.53 eV [89], and between carbon and oxygen on the surface of diamond is 531.00 eV, as seen in Fig. 3.9 and in Ref. [72]. Titanium reacts with the dangling bonds of carbon on the surface of the diamond, forming a very thin carbide layer with binding energy of 281.8 eV [73], responsible for tunnelling conduction. Platinum is deposited over it to form an intermediate layer between the initial and the final layers. Here, platinum is used as an intermediate layer in order to prevent the penetration of carbon atoms

into the top gold layer which would otherwise produce the non-desirable effect of rectification. Gold, with anti-oxidative properties, is the final layer to be deposited on the surface of diamond. Ohmic contacts can also be achieved by creating a p-type layer by heavy doping of a surface layer of the sample, usually with an acceptor impurity forming a p-type surface layer. This is then followed by metallic deposition on the same surface [90, 91, 92].

After the process of metallization the samples were annealed in a vacuum of about 10^{-5} mbar. To allow for a rapid heating and cooling process the samples were placed inside a quartz glass, which was in turn placed inside a ceramic furnace. Heating was performed by ramping up temperatures at a rate of about 10°C/min up to 600°C and maintaining the temperature for 10 min. Cooling was performed by ramping down the temperatures at the same rate.

Current-voltage characteristics

The effect of SSN concentration on current-voltage characteristics was investigated for two samples of type Ib diamond *viz.* Ib_1 and Ib_2, with 46 ppm and 215 ppm concentration of SSN, respectively. The leakage current was measured as a function of applied external electric field on the metal plates separated by distances of about 420 μm for sample Ib_1 and 600 μm for sample Ib_2. The area of the contacts for both samples was 0.19 cm^2, respectively. The I-V characteristics shown in Fig. 4.1 and 4.2 were acquired using a KEITHLEY electrometer model 6517A.

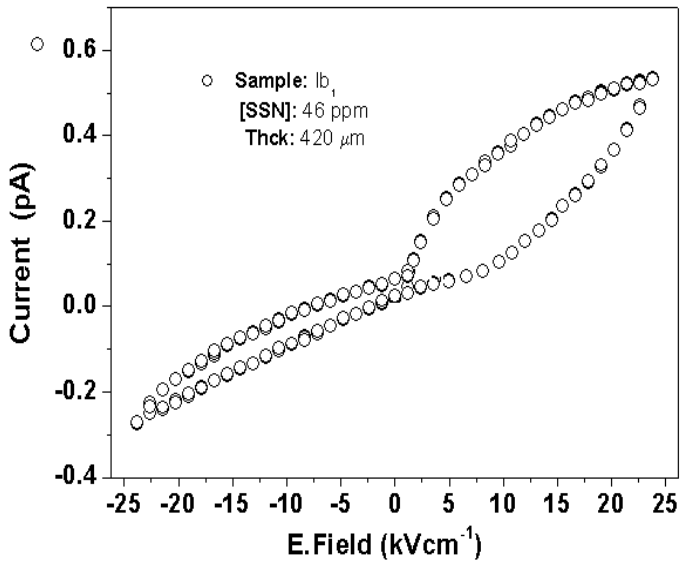

Figure 4.1: Current-voltage characteristic of a type Ib diamond, sample Ib_1, with 46 ppm of concentration of SSN showing hysteresis behaviour.

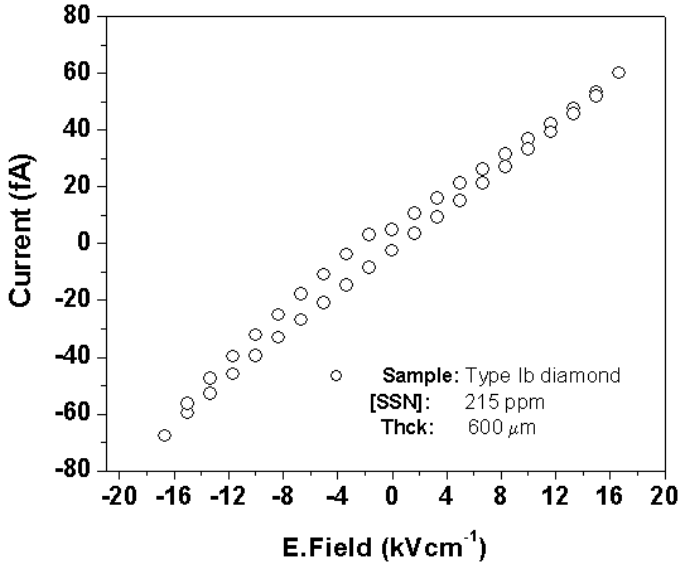

Figure 4.2: Current-voltage characteristic of a type Ib diamond, sample Ib_2, with 200 ppm of concentration of SSN.

In sample Ib_1 with a SSN concentration of 46 ppm, see Fig. 4.1, the leakage current was measured to be of the order of 10^{-13} A at a maximum applied external electric field of about ± 22.5 kVcm^{-1}. The hysteresis behaviour, with wide open cycle at positive applied external electric field clearly seen, in the I-V characteristic.

The leakage current obtained from sample Ib_2, with a SSN concentration of 215 ppm, see Fig. 4.2, is about 10^{-14} A at a maximum applied external electric field of about ± 17.5 kVcm^{-1}. For this sample the hysteresis cycle is very narrow.

The increase of leakage current in sample Ib_1 and the presence of a wide hysteresis cycle at positive applied external electric field as compared to the sample Ib_2 is the result of reduced concentrations of deep traps and small concentrations of uncompensated boron impurities as discussed in Chapter 3.

The hysteresis cycles for both I-V characteristics may also be attributed to differences in the capacitances of both devices. The capacitances were estimated using the relation $C = \epsilon\epsilon_0 \frac{A}{D}$, where ϵ_0 is the permittivity of the free space, ϵ is the dielectric constant of diamond, A is the area of the contacts and D is the thickness of the diamond. For sample Ib_1 the capacitance is about 2.26 pF, which is $\sim 2\times$ the capacitance of that of sample Ib_2, being 1.58 pF.

4.2.2 Schottky contacts

The choice of this type of contact for synthetic type IIa HPHT diamond was determined by the presence of some boron acceptors found by the UV-cathodoluminescence

topography, as presented in Chapter 3. As the concentration of boron acceptors increase the I-V curve exhibits ohmic, rather than Schottky behaviour, with saturation at high currents. On the other hand, for small concentrations of boron acceptors the saturation curve may occur only at μA region. Therefore Schottky contacts will give rise to a hole depletion layer [31, 93] reducing this way the leakage current due to presence of boron impurity.

Samples D2, D3, D4 and the type IIb natural diamond, had Schottky contacts made of Cr/Au, [31, 94, 95], deposited on both surfaces forming parallel plates. The deposition was performed in an argon spattering chamber in a vacuum of about 10^{-6} mbar. Chromium was the first layer to be deposited, which reacted with existing oxygen on the surface forming metal oxide layer, followed by Au as an antioxidant layer. The annealing process for these samples took place in argon environment for 1 h at temperatures of about 400 °C. The type IIb natural diamond had its surface treated with hydrogen to passivate boron acceptors [96, 97, 98] and to increase the contact resistivity.

Sample D2a had its contacts made using a combination of Ti/Pt/Au-diamond-Cr/Au, with deposited thicknesses of about 1500 Å. The deposition of Ti/Pt/Au was performed using the e-beam system in vacuum starting from 10^{-7} mbar, while for the Cr/Au deposition the vacuum was of the order of 10^{-6} mbar. The contacts for this sample were not annealed in order to reduce formation of titanium carbide, thus enhancing in this manner the Schottky contact characteristics.

Current-voltage characteristics were acquired for samples D2, D3, D4 of thicknesses

of about 3 mm, D2a of thickness of about 0.46 mm, and a type IIb natural diamond with a thickness of about 1.6 mm. Sample D2a was sliced from sample D2. The areas of contacts where about 0.5 cm^{-2} for the synthetic type IIa HPHT diamonds and about 0.2 cm^{-2} for the natural type IIb diamond.

Current-Voltage characteristics

The I-V measurements were performed on the aforementioned samples using a Keithley electrometer model 6517A. In the case of the natural type IIb diamond, the I-V characteristic was acquired before and after irradiation with α-particles. In the case of sample D2a, additional measurements were performed by selecting three different areas on the surface, namely, the center, the edge and half way between the center and the edge. In this case, the sample had a distribution of metallic dots made of Cr/Au, on one of the surfaces, while the other surface was entirely covered with layers of Ti/Pt/Au. The different metallic dots on one surface were used to probe different regions of the sample and observe the differences.

The current-voltage characteristics were first obtained for samples D2, D3 and D4. As shown in the Fig. 4.3, the leakage current measured for samples D2, D3 and D4 varies between 10^{-6} A and 10^{-3} A at a maximum applied external electric field of about 14.2 Vcm^{-1}. It was found that the current depends on the concentration of SSN, which was measured in the adiabatic rapid passage manner, as presented in the chapter 3. Lower concentrations of the SSN result in low factor of boron compensation, which is responsible for high leakage current as a function of applied bias voltage, as seen in Fig. 4.3. The I-V characteristic curve of sample D2a, in

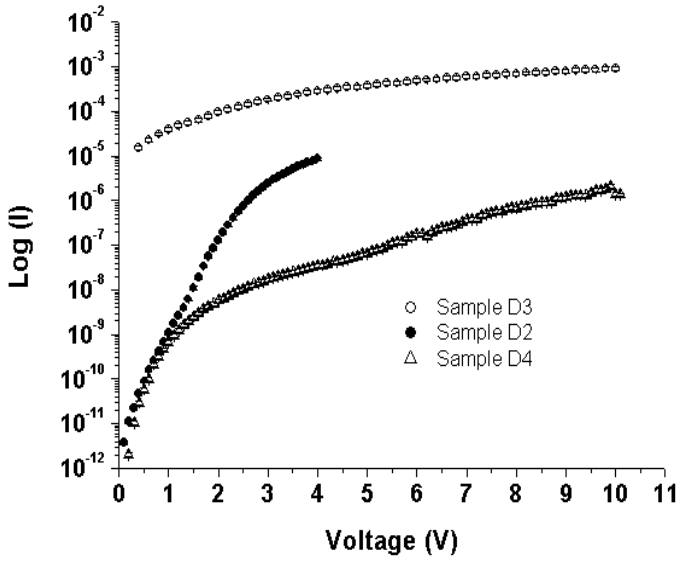

Figure 4.3: I-V characteristic for samples D2, D3 and D4, with Schottky contacts after the annealing process. The higher leakage is associate with lower concentration of SSN.

which the contacts deposited were not annealed, is shown in Fig. 4.4 together with I-V curve of sample D2 for comparison reasons. The leakage current measured is of the order of 10^{-6} A and the resistivity is about 10^{7} Ωcm. These values were obtained at a maximum applied external electric field of approximately 440 Vcm^{-1}, as shown in Fig. 4.3. Since sample D2a originated from the same crystal, D2, the observed differences must be related to the different contact deposition processes followed by the possible reduced concentrations of boron acceptors in the near surface region of the sample D2 compared to the bulk region. The last effect has also been observed by J. Buttler *et al.* [99].

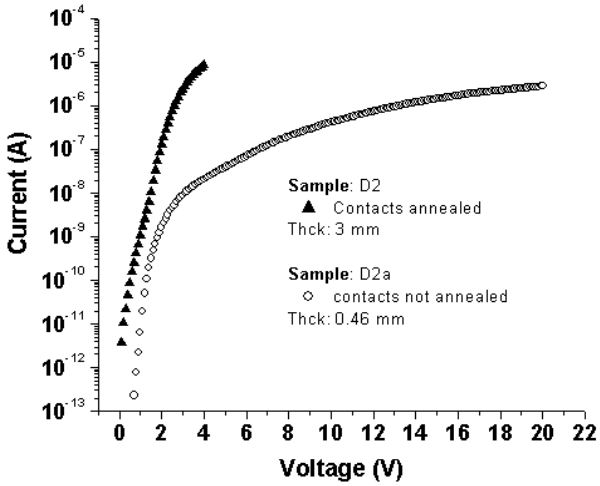

Figure 4.4: I-V characteristic for samples D2 and D2a, with Schottky contacts, before and after annealing process.

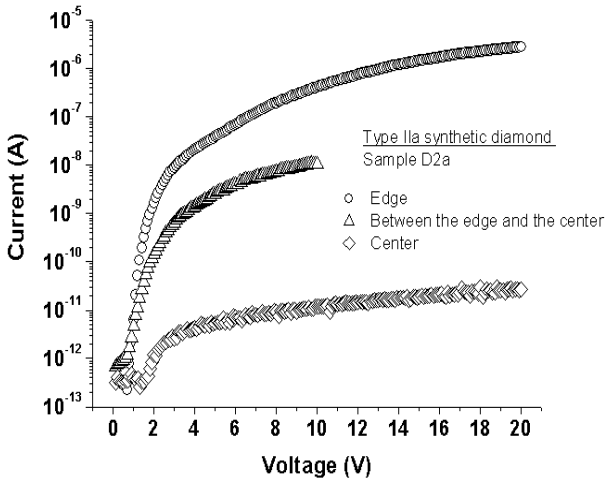

Figure 4.5: I-V characteristics measured in different regions of the sample D2a. The contacts were not annealed.

I-V measurements in three regions of sample D2a show variations in the leakage current as seen in Fig. 4.5. At the center of the sample the saturation curve is about 10^{-12} A, half way between the center and the edge the saturation curve is about 10^{-9} A and at the edge it starts at about 10^{-8} A. The saturation in all cases occurs at $\sim$ 2.5 V.

From these findings, and correlated with the previous results obtained by UV-catholuminescence topograph presented in Chapter 3, one can conclude that the center of the sample contains a high fraction of compensated impurities compared to the other regions of the diamond. This occurrence may or may not be always reproducible in all synthetic type IIa HPHT diamonds.

4.2.3 Current-voltage characteristics for a hydrogenated surface of a type IIb diamond, before and after irradiation

The surface of a natural type IIb diamond was exposed to hydrogen plasma for five minutes, in order to compensate boron acceptors on the surface before metallization. The area of the contact applied was 2 mm^2 and the thickness of the sample was about 1.6 mm. The sample was irradiated with α-particles (5.486 MeV) from ^{241}Am source for a time $\sim$ 1 min. I-V characteristics were acquired before and after irradiation.

Results and discussion

The I-V characteristic curve of a type IIb diamond with a surface treated in hydrogen plasma shows a leakage current of about 3.0×10^{-9} A. The maximum applied external electric field was about 10 kVcm^{-1}, as shown in Fig. 4.6.

After the radiation exposure for a time $\leq$ 1 min, the I-V characteristics no longer show Schottky but ohmic behaviour. In this case the leakage current increased to about 10^{-3} A, with a saturation of about $\pm$ 2$\times 10^{-3}$ A at applied external electric field of about $\pm$ 1 kVcm^{-1}, as shown in Fig 4.7.

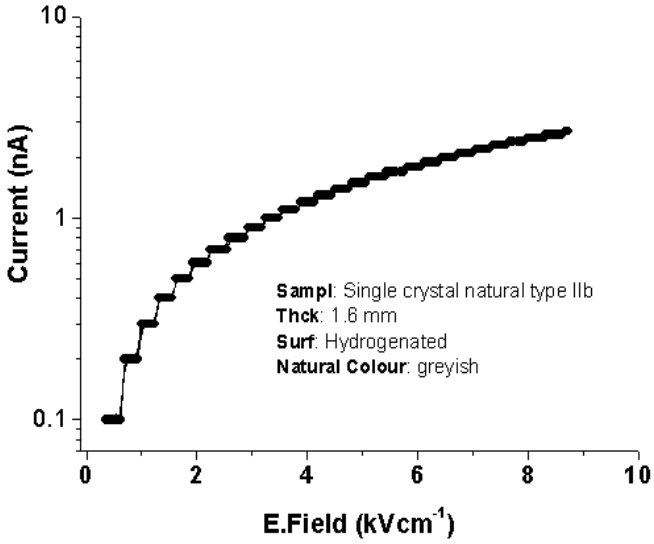

Figure 4.6: I-V characteristic of a natural type IIb diamond after surface hydrogenation. The contacts were not annealed.

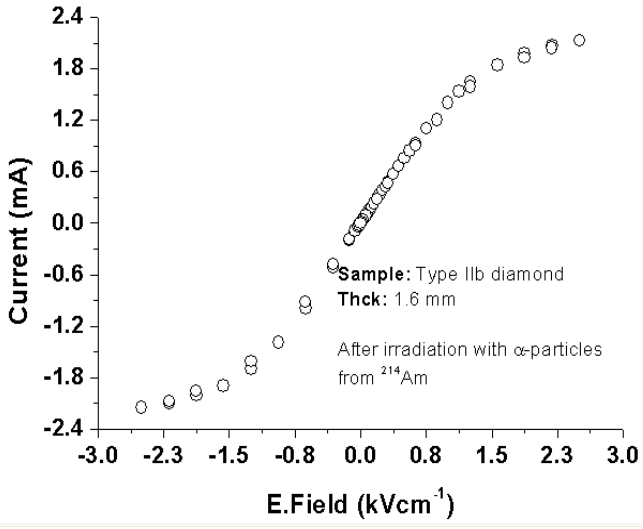

Figure 4.7: The I-V characteristic of natural type IIb, after been exposed to α-particles emitted by ^{241}Am source.

4.2.4 Assessment of Ohmic and Schottky contacts using photons

Characterization of timing properties using UV-photons

Detector devices made of type Ib diamonds were fabricated and their response in terms of output pulses as a function of contacts applied was investigated. Measurements of photocurrent *versus* time [32, 65] as a function of type of contacts were performed using UV-photons of about 5.6 eV, matching the diamond band gap. Ohmic contacts were deposited in parallel plate geometry, which were composed of layers of 200 Å of Ti, 300 Å of Pt and 1000 Å of Au. The sample was annealed after contact deposition using the same aforementioned procedures applied to the samples Ib_1 and Ib_2.

Measurements were also performed on the same sample with Schottky contacts [32, 65], also using UV-photons of 5.6 eV. These contacts consisted of layers of 300 Å of

Cr and 1000 Å of gold, deposited in one surface while on the opposite surface the contacts were made of Ti/Pt/Au, using the same ratio as in the previous case. The contacts were not annealed.

The photon beam was generated by quintupled 5 ns neodymium-yttrium aluminium garnet (Nd:YAG) laser, the energy of the photon was 5.6 eV and the width of the pulse emitted was 5 ns with repetition rate of 10 Hz [14]. By using the frequency doubling crystal, β-barium-borate (BBO), the width of the pulse generated with the photon energy of 5.6 eV was narrowed to 500 ps [31]. The external electric field applied to the detector was varied between $-$ 5.0 kVcm^{-1} and $-$ 20.0 kVcm^{-1}. The pulses were acquired using a wide bandwidth oscilloscope of about 1 GHz, terminated with 50 Ω resistance. The pulses were normalized to the same photocurrent to facilitate the analysis.

In the case of ohmic contacts, as seen in Fig. 4.8 a), small fluctuations regarding the centroid of the pulses was observed as the applied external electric field was varied. The pulses have a narrow width and background fluctuations for an applied external electric field lower than -20 kVcm^{-1}. The photocurrent measured was of the order of 10 $^{-6}$ A. In addition, each pulse shape consists of two main peaks; the first represents fast extraction of charge carriers from the front contact and is dependent on the total energy deposited in the near surface region and the type of contacts, and the second peak is due to charge carriers extracted from the opposite electrode. The second peak centroid also exhibits fluctuations with the applied external electric field, of 14 ns for fields in the region of $-$ 5 kVcm^{-1} and $-$ 20 kVcm^{-1}.

In the case of Schottky contacts, see Fig. 4.8 b), the centroid of the pulses is $\sim$ 1.5 ns faster compared to the same parameter for ohmic contacts and does not vary with the field. In general, the FWHM increases with increasing external electric field, however, space charge effects tend to reduce this parameter at high fields due to polarization effects. The top of the pulse at high applied external electric field starts to become flat and the device nears the saturation region. The photocurrent induced in the device with Schottky contacts is one order of magnitude higher than that of ohmic contacts, which is about 10^{-5} A. The second peak, observed when ohmic contacts are implemented, almost vanishes with Schottky contacts since all charges carriers are extracted from one contact and the decay time is a function of concentration of impurities and the size of applied external electric field.

The only constraints with the application of Schottky contacts on type Ib and natural type IIa diamond with certain density of defects is the enhanced probability of generation of space charge and internal polarization effects. This affects the amplitude of the pulses as a function of time. The differences between Schottky and ohmic contacts are summarized on the Table 4.1.

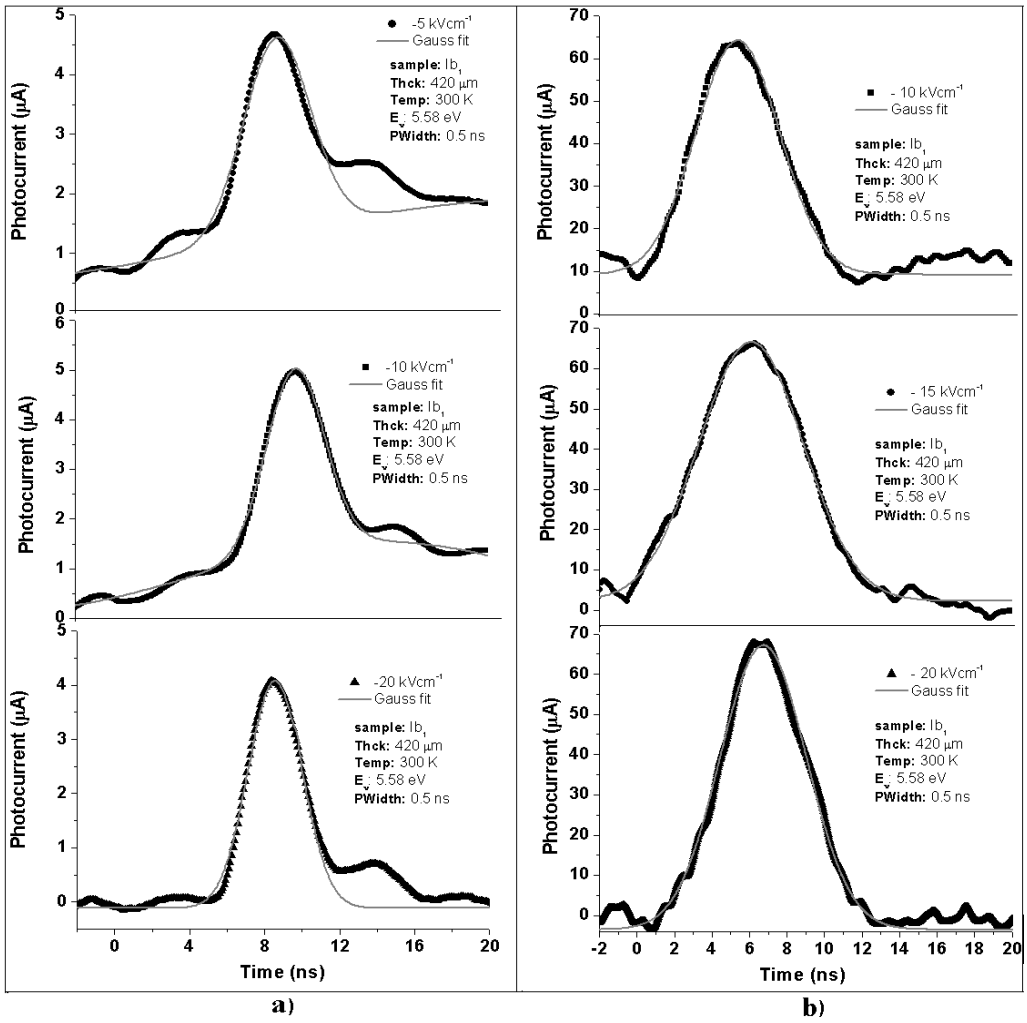

Figure 4.8: Pulse generated by UV photon on the sample Ib_1. On a) the detector is implemented with ohnmic contacts made of Ti/Pt/Au and on b) the detector is implemented with Schottky contacts made of Ti/Pt/Au and Cr/Au.

Table 4.1: Property of the output pulse as a function of contacts

E.Field ohmic (kV/cm)	1^{st} Peak centroid (ns)	FWHM (ns)	2^{nd} Peak centroid (ns)	E.Field Schottky (kV/cm)	1^{st} Peak centroid (ns)	FWHM (ns)	2^{nd} Peak centroid (ns)
−5.00	8.70	3.18	14.00	−10.00	6.03	4.27	N/A
−10.00	9.88	3.46	15.00	−15.00	6.07	5.59	N/A
−20.00	8.46	2.52	14.00	−20.00	6.74	4.60	N/A

4.2.5 Summary of the results obtained assessing Ohmic and Schottky contacts as a function of impurities

It was found that the leakage current as a function of concentration of SSN increased 10 orders of magnitude when the concentration of SSN was reduced in 150 ppm. Taking into account that a pure diamond is a material of very low leakage current, the increment in the leakage current in sample Ib_1 is definitely related to the presence of low concentrations of uncompensated boron impurity, as seen in the cathodoluminescence topography presented in Chapter 3.

In the case of a synthetic type IIa HPHT diamond it was shown that although the concentration of boron acceptors is very low the leakage current is very high. The low leakage current observed for sample D2a, sliced from D2, is probably due to the fact that the contacts were not annealed. Another contribution to this effect could be that the sample was sliced from the top part of the sample D2, and the spacial distribution of boron concentration in the bulk was not uniform. On the other hand, different regions of this sample show variations in the leakage current. These variations are a function of compensating factor of impurities and differences in the concentrations of boron impurity in various regions of the diamond.

The compensation of boron in type IIb diamond by treating the surface with hydrogen is not an effective method to increase the resistivity in order to use the crystal as a particle detector.The generation of charge carriers in the detector during irradiation seems to destroy boron-hydrogen bond increasing the tunnelling probability of charge carriers through the junction. In this case, the contacts lost their Schottky

and gained ohmic properties. According to Massarani *et al.*, in Ref. [70], the ionizing radiation induces a change in the population distribution of impurities, decreasing the compensation. On the other hand, according to Ref. [98] hydrogen in a boron doped diamond vanishes at temperatures of 400 °C and above.

Time response of the device as a function of contacts applied

The results obtained from the interaction of UV photons with a diamond device show time fluctuations in the average signal obtained from the device with ohmic contacts. These signals are composed of two major peaks; one resulting from the fast extraction of charge carriers from the front contact and the other from extraction from the rear contact. Using Schottky contacts the photocurrent induced improves to about 10 orders of magnitude, in addition there is less time fluctuation. The width of the output pulse is even larger. This implies that the pulse is mainly extracted from only one contact. The width of the pulse is dependent on the concentration of impurities, the size of applied external electric field and the polarization effects.

4.3 Deep level transient spectroscopy (DLTS)

In an attempt to estimate the concentration of boron acceptors [100, 101] in a synthetic single crystal type IIa HPHT diamond, sample D2a, and the energy levels introduced by this impurity, Deep Level Transient Spectroscopy (DLTS) was employed. This technique also allows an estimation of the degree of compensation between SSN and boron impurities as described in Ref. [41]. From the results obtained using the ESR technique and the cathodoluminescence topography in Chapter

3, it is clear that the average compensation factor is very low and the properties of the material is determined by the presence of uncompensated boron impurity. However, the current-voltage characteristic shows variation of leakage current in different regions of the sample, as seen in Fig. 4.5. By measuring the energy levels of boron in these particular regions it is possible to have a clear picture of the compensation factor, concentration and the distribution of impurities.

The thermal emission of trapped charge carriers to the conduction band, where they are instantaneously swept away by the electric field at the junction, is observed as a majority-carrier capacitance transient [102]. The emission rate of the charge carriers from the trap, given by Eq. (2.2.26), can be determined from the time dependence of the capacitance transient. In addition, the density of occupied traps, as a function of the emission rate, is given by Eq. (2.2.23) [33, 103, 104]. Also, the extraction of the emission rates, Eq. (2.2.26), allows a determination of the energy levels $E_{\mathrm{T_i}}$ (i=1,2,3...), and the respective apparent capture cross sections σ_{n} of the defects. The thermal activation energy for emission of an electron to the conduction band is given by Eq. (2.2.27).

In the case where the capacitance of the interface junction, at zero applied electric field, is negligible a different variation of the DLTS technique, current-Deep Level Transient Spectroscopy (I-DLTS) is applied. The transient current I_{t} is given by:

$$I_{\mathrm{t}} = I_{\mathrm{e}} + I_{\mathrm{d}}, \tag{4.3.1}$$

where I_{e} is the emitted current and I_{d} is the displacement current due to the applied

field. The total current generated is give by [105]:

$$I_{\mathrm{T}} = \frac{qAW(t)e_{\mathrm{n}}n_{\mathrm{T}}(\mathrm{t})}{2} + I_{\mathrm{j}}, \tag{4.3.2}$$

where the $W(t)$ is the width of the depletion region as a function of transient time (t) of charge carriers, q is the charge, A is the thickness of the specimen, e_{n} is the emission rate of charge carriers from the traps, given by Eq. (2.2.26), n_{T} is the total concentration of charge trapped, which is a function of temperature and I_{j} is the current at the interface junction. The transient current is contained in the first term, in the Eq. (4.3.1). The width of the depletion region $W(t)$ is given by [105]:

$$W(t) = \frac{W(0)}{\sqrt{1\text{-}\mathrm{n_T}/\mathrm{N_A}}} + I_{\mathrm{j}}, \tag{4.3.3}$$

where $W(0)$ corresponds to the width of the depletion region at zero transient time.

By applying a steady-state reverse bias, the traps in the depletion region above the Fermi-level are empty. Reducing the applied bias voltage, which in turns reduces the width of the depletion region, the charge carriers are trapped in the deep levels. By restoring the bias voltage to its original steady-state value, filling of the traps within the depletion region [33] was found.

4.3.1 Experimental procedures

For the DLTS investigation the synthetic type IIa HPHT diamond, sample D2a selected for this measurement, had contacts made of layers Cr/Au deposited on one surface as dots of 0.3 mm and layers of Ti/Pt/Au covering the opposite surface

entirely in parallel plate geometry, forming Schottky diodes, see Fig. 7.7. Current-voltage and capacitance-voltage characteristics were measured in the three regions of the device, namely in the center, in the intermediate region between the center and the edge and at the edge.

The conventional DLTS measurements were performed by scanning the sample temperatures and numerically analyzing the repetitive thermal-emission transients. This was done using either boxcar or lock in amplifier-like analyzer routines. The measurement was performed in an isothermal low-noise DLTS system within a highly stable temperature cryostat chamber. During the measurements, a reverse bias was applied to the Schottky diode. Pulse filling was superimposed onto the reverse bias in order to fill the defect with carriers. The duration of the pulse was long enough to fill most of the traps. After pulse filling, reverse bias was re-applied allowing the defects to emit carriers. The charge carrier emitted gives rise to a transient in the monitored capacitance current.

A DLTS spectrum is obtained by plotting the output of the analyzer *versus* temperature. Each peak in the DLTS spectrum is indicative of an energy level [104] (E_{T}) and the respective capture cross-section (σ_{n}). These parameters can be extracted from the Arrhenius plot of emission rates vs temperature, $\log(\mathrm{e_n}/\mathrm{T}^2)$ *versus* $1/\mathrm{T}$, [100]. The values of the emission rates can be measured during the temperature shifts. The charge density, i.e. the defect concentration, as a function of shallow acceptor defects, was measured in the freeze-out temperature region.

The I-DLTS spectra *versus* temperature in the three regions of the diamond, namely,

the center, the intermediate region and the edge were acquired using a lock-in amplifier with a rate window of 4989.60 s^{-1}. Ramping temperatures of 0.10 K s^{-1}, varied from 170 K up to 290 K, were applied. An external electric field of about − 0.11 $kVcm^{-1}$ was applied to the material and the duration of the filling pulse was about 1 ms. Signals were acquired at a frequency of 5 kHz. These measurements were carried out at constant temperature for a number of different temperatures with an interval of about 2 K in each case.

The DLTS signal was assumed to be a superposition of exponential emission rates [33, 104]:

$$f(t) = \int_0^{\infty} F(s)e^{-st}ds, \tag{4.3.4}$$

where $f(t)$ is recorded transient and $F(s)$ is the spectral density function. Equation (4.3.3) is the Laplace transform of the true spectral function $F(s)$.

4.3.2 Results and discussion

The current-voltage characteristics results obtained from the three regions of sample D2a are shown in Fig. 4.5. A high leakage current was found at the edge of the sample and progressively reduces towards the center. The capacitance-voltage (C-V) characteristics are negligible small and need not to be taken into account. Hence, the carrier density could not be determined and consequently neither the magnitude of the depletion region during the DLTS reverse bias cycle. On the other hand, using the I-DLTS the defect level is only partially populated by the filling of pulses and the charge measured, in freeze-out temperatures, is only representative of a fraction

of trapping defects. Therefore, no quantitative trap concentrations could be derived. However, one can still compare relative peak amplitudes.

Current-DLTS signal

The I-DLTS signal from the edge region of the sample, seen in Fig. 4.9, shows about 7.5× higher strength compared to the pulse acquired from the center region of the sample. This implies a higher concentration of boron acceptors in this region compared to the center. There is also an indication that there may be more than one defect present with closely separated energy levels and respective capture cross-sections.

Spectra of emission rates

The spectra of the emission rates acquired in the three regions of the sample are shown in Figs. 4.10, 4.11 and 4.12. From the center towards the edge, the peak intensity increases with respect to temperature. The central peak, labeled in all spectra as E_{T_1}, is assumed to originate from uncompensated boron impurity since its increment with the temperature is position sensitive. A correlation of this variation and the result from cathodoluminescence topography, shown in Fig. 3.18, can be made. In this figure, the edge shows more intense blue luminescence compared to the other regions of the sample. The peak labeled E_{T_2} shows a stable variation with respect to temperature in all regions of the sample. This peak is probably related to impurity and defect association.

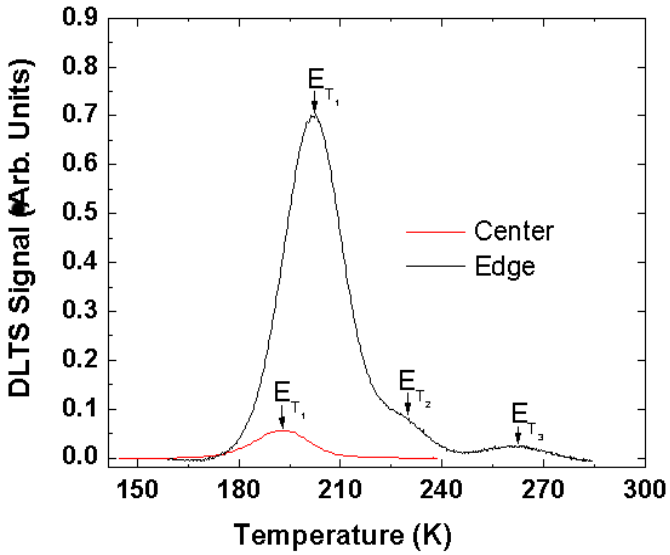

Figure 4.9: I-DLTS signal in the center and of the edge of the type IIa ultra pure HPHT diamond. The spectra show a high intensity signal at the edge which is a function of the compensating factor rather than the concentration of boron impurity acceptor. $E_{\mathrm{T}_{1,2,3}}$ represent signals of the defects from the center to the edge of the sample.

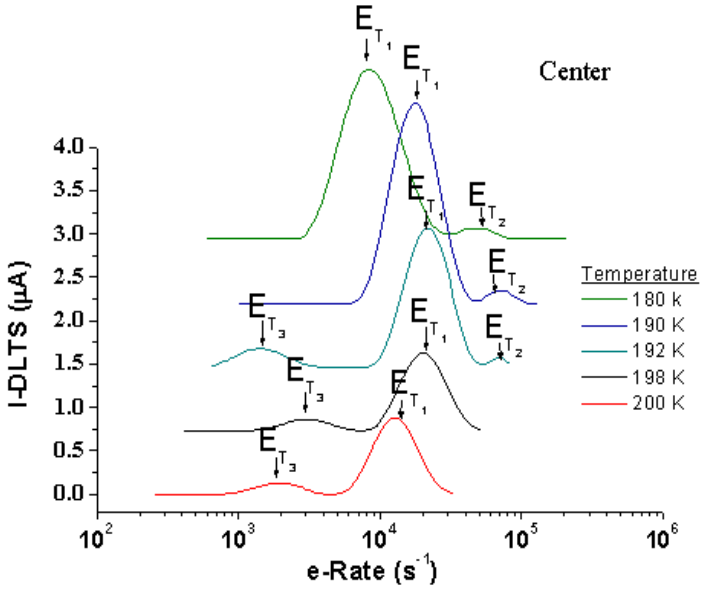

Figure 4.10: At the center of the sample the intensity of the peak at high temperature is dependent on the compensation factor. The higher the compensation factor, the higher the activation energy and the lower the intensity of the emission rates.

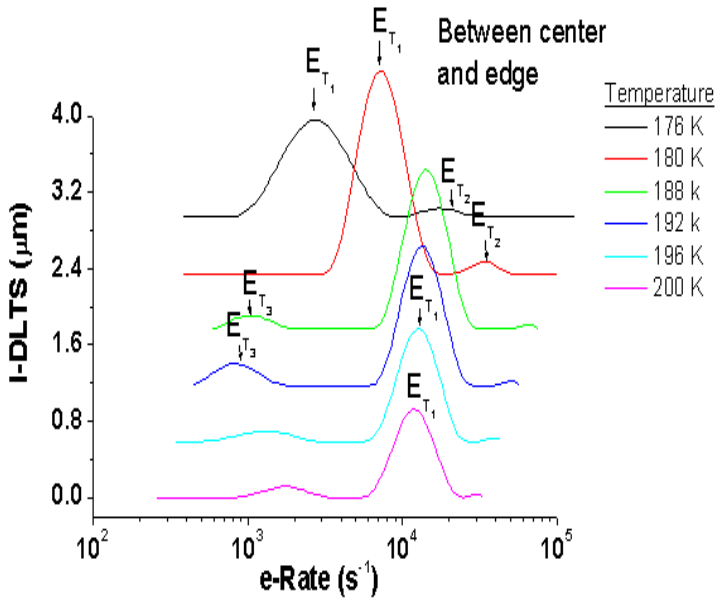

Figure 4.11: In the region adjacent to the center, the increment of the intensity of the peak, labeled E_{T_1}, results from a decrease in the compensation factor of impurities in this region.

The third defect apparent in all spectra has a stable variation only at the edge region of the sample, as shown in Figs. 4.12 and 4.13, relatively to the variation in temperature. This defect is probably associated with high density of crystallographic defect, see Fig. 3.6. At the other two regions, at the center and at the intermediate region, the variation of the third defect with the temperature is not stable. The third signal in these two regions might result from an artefact during the measurements.

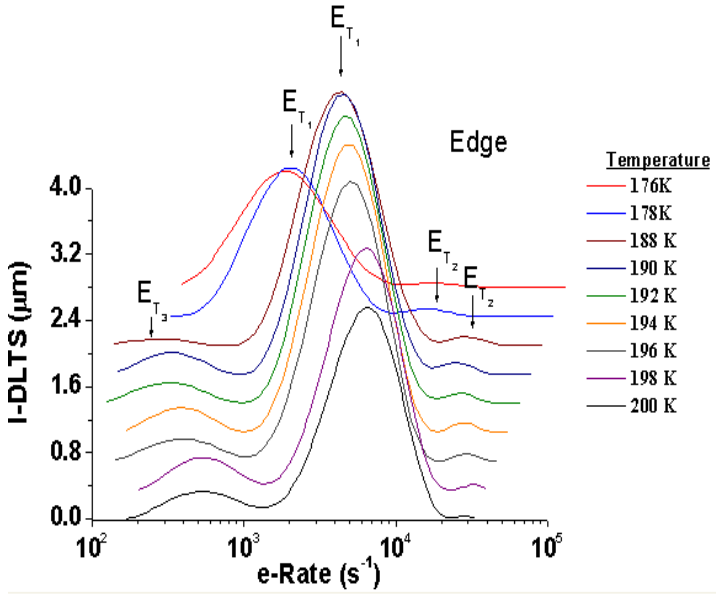

Figure 4.12: At the edge, the intensity of the main peak increased considerably, which is an indication of high concentrations of uncompensated boron impurity. The intensity of other two peaks, corresponding to defects and associations, shows a stable variation in this region of the sample with respect to temperature.

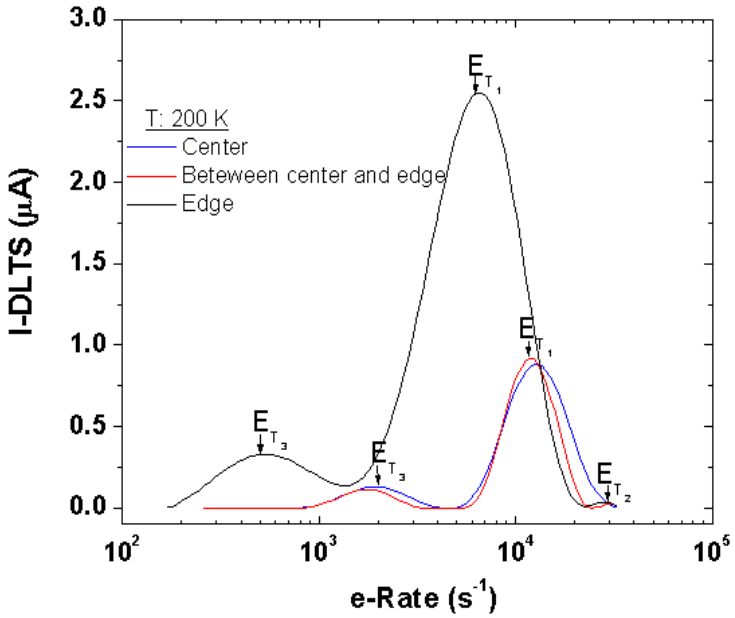

Figure 4.13: The spectra of the emission rates acquired at high temperature shows clearly the differences in intensity of the defects in the three regions of the sample.

Arrhenius plot

The activation energies $E_{T_{1,2,3}}$ and the capture cross-sections σ of each defect measured were extracted from the Arrhenius plot shown in Fig. 4.14. The values of the activation energy of the main defect, E_{T_1} decreased from the center towards the edge. At the center of the sample the value is about 0.31 eV ± 0.002 eV with a capture cross-section of 29.11×10^{-15} cm^2. In the region near the center the activation energy of the main defect is about 0.308 eV ±0.007 eV with a capture cross-section of 28.36×10^{-15} cm^2. At the edge the activation energy of the main defect is 0.254 eV ± 0.007 eV with a capture cross-section of about 0.641×10^{-15} cm^2.

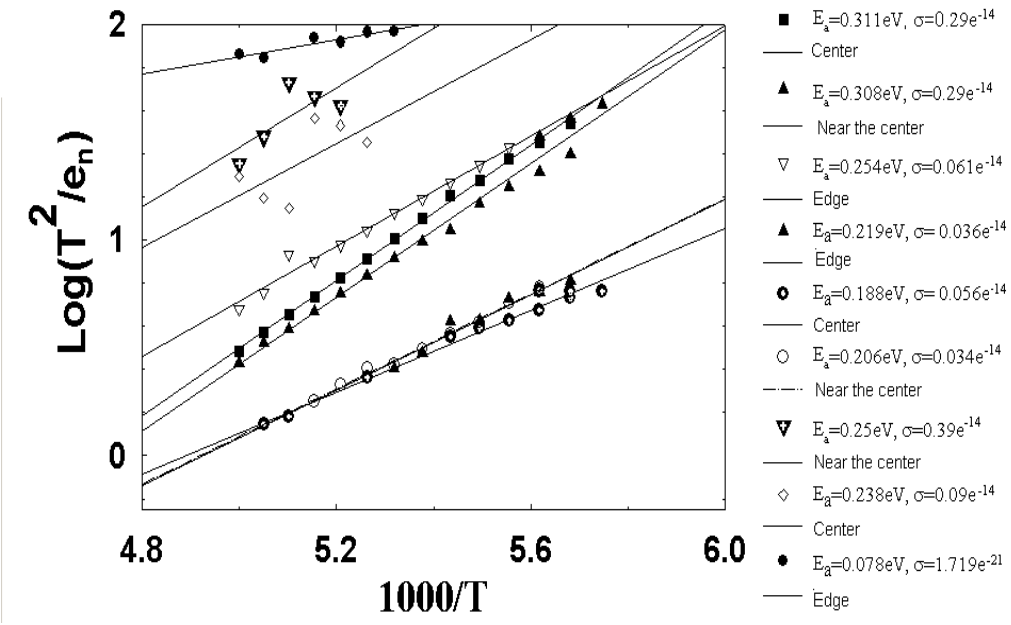

Figure 4.14: The Arrehnius plot of Log(T^2/e_n)*versus* 1000/T of the the three different regions of the sample.

The variation of these values implies the presence of a compensating factor of impurities that is higher at the center region of the diamond and decreases towards the

edge. The second defect, labeled E_{T_2}, also found in the three regions of the sample is not position sensitive. The values obtained suggest the possible presence of associated defects. A third defect center, E_{T_3}, has a stable variation with temperature only at the edge. The energy levels of all defects and their capture cross-sections are summarized in the Table 4.2 and extracted from the Arrhenius plot shown in Fig. 4.14.

Table 4.2: Activation energies and capture cross sections in three regions of diamond sample

B	$E_{a_{\text{near-center}}}$ [eV]	$\sigma_{\text{near-center}}$ [$\times 10^{-15}$ cm^2]	$E_{a_{\text{center}}}$ [eV]	σ_{center} [$\times 10^{-15}$ cm^2]	$E_{a_{\text{edge}}}$ [eV]	σ_{edge} [$\times 10^{-15}$ cm^2]
1	0.308	28.360	0.311	29.111	0.254	0.641
2	0.188	0.056	0.206	0.355	0.219	0.335
3	0.238	0.0884	0.250	0.3881	0.078	1.719×10^{-6}

4.3.3 Summary of the results obtained using the I-DLTS technique

An empirical estimation of the concentration of boron acceptors can be done assuming that it has probably the same concentration values of the SSN impurity, which is approximately 10^{12} or 10^{13}. This assumption has been considered taking into account that boron acceptors and the SSN donor in diamond do not compensate at the same concentration values [17]. The real concentration could not be estimated due to the low effectiveness of trap filling at low temperatures.

The maximum activation energy E_{T_1} of the boron acceptor in each region is position sensitive. At the center the value is 0.31 eV $\pm$ 0.0025 eV, in the region near the center the value is 0.308 eV $\pm$ 0.007 eV and at the edge the value is 0.254 eV $\pm$

0.007 eV. Thus, the center region of the diamond is the region of low concentration of uncompensated boron acceptors. The concentrations of uncompensated boron acceptors increases towards the edge, decreasing in this way the activation energies also.

The second energy level on each region does not vary as a function of compensation, as in the first case, and this level seams to be generated by impurity and defect association. Each region is characterized by defects with high density at the edge. The third energy level exhibits a stable variation with temperature at the edge. It should be noted that the edge of the sample contains a relative high density of crystallographic defects compared to other regions.

The correlation between the maximum activation energies measured and the results obtained from I-V characteristics in these regions, points to the important role that the compensating factor of impurities plays, rather than the reduced concentrations of boron acceptors. Although this result cannot be generalized to all synthetic type IIa HPHT diamonds, since each sample is unique, however, it does show that the electronic behaviour of diamond-based devices cannot be judged by the concentration of the dopants alone.

4.4 Electronic properties of synthetic single crystals type IIa HPHT diamond

The electronic properties, such as the charge carrier mobility, the charge collection and the time properties, of a high purity type IIa HPHT diamond the sample D2a were investigated by employing the time of flight (TOF) technique using pulsed laser beams [106, 107]. Metal of high work function Ruthenium (Ru) [108] and the combination of this metal with layers of Ti/Pt/Au, were applied on the surfaces of the diamond in coplanar geometry to produce a detector device.

In this device, the charge carriers were generated using photons from a pulsed laser with an energy just above the band gap of the material [32, 65]. The incident photons are absorbed within a few μm's of the material depending on their wavelength.

The time of flight was also used in the investigation by employing α-particles [109] with energy of 8.78 MeV emitted from ^{228}Th source. The results were compared to the obtained using UV photons. Alpha particles from the source used have an average stoping range equivalent to 14 μm in diamond. Since this range is in the near surface region and if the α-particles are incident on the surface of the detector containing the electrode then it should produces almost the same effect in a thick sample as of that generated by the UV-photons.

In both cases when UV-photons or α-particles with very short range in the crystal are applied, the electronic properties of the device are determined by the time separation (the mean lifetime) of the pair of charges generated (the electron-hole plasma) and

the mean separation length (the carrier charge Schubweg) before recombination. The transient time and the charge collection properties of the device are obtained by the charges that survived the first recombination process and are accelerated towards the opposite electrode by the electric-field applied to the device. When Schottky contacts are implemented, the ejection of charge carriers will occur when the electric-field applied lowers the barrier height allowing the flat band conditions to occur [31, 63].

On arrival at the opposite electrode an electric pulse is emitted, amplified if necessary and recorded by the electronic readouts applied to the device. An electronic pulse provides information on the timing and collection properties of the diamond detector. Through the amplitude of the pulse, the impedance of the electronics and the area of the electrodes, one can extract the current density (J_{d}) at the electrodes [110]. This physical quantity, together with the amount of applied external bias voltage (V) on the device, allows an estimation of the charge carrier mobility (μ) using the Mott-Gurney Law [26, 57, 111], taking into account the low concentration of impurities in the device:

$$\mu = \frac{8}{9}\frac{J_{\mathrm{d}} D^3}{V^2 \epsilon \epsilon_0}, \tag{4.4.1}$$

where D is the distance between the electrodes, ϵ is the dielectric constant of the diamond and ϵ_0 is the dielectric permittivity of the free space (8.85×10^{-12} $\mathrm{C^2N^{-1}m^{-2}}$).

The transient time $\tau_{(\mathrm{e,h})}$ is extracted from the width of the output pulse, which corresponds to the time that the charge carrier under applied external electric field

travels towards the opposite electrodes before recombining. The charge carrier lifetime, which is the time that the pair of charges generated (N_{gen}) remains separated before recombination or trapped, is obtained from Eqs. (2.5.21) and (2.5.22). The charge carrier life time can also be estimated by [112, 113]:

$$\tau_{(\text{e,h})} = \eta \tau_{\text{t}_{(\text{e,h})}}, \tag{4.4.2}$$

where η is the efficiency of the device and is dependent on the type of conduction performed by the device (see Chapter 2) and Eqs. (2.5.21) and (2.5.22). This parameter is extracted from the following equation [112]:

$$\eta_{(\text{e,h})} = \mu\tau \frac{V}{D^2}, \tag{4.4.3}$$

where V is the applied bias voltage, D is the thickness of the detector. The photocurrent, $I_{\text{ph}_{\text{ind}}}$, induced on the electrodes is given by the following relation [61]:

$$I_{(\text{ph}_{\text{ind}})} = I_{(\text{ph}_{\text{gen}})} \eta_{\text{coll}}, \tag{4.4.4}$$

where $I_{\text{ph}_{\text{gen}}}$ is the total photocurrent generated by the incident photons.

The photocurrent generated is a function of absorption ($\alpha(\lambda)$) and reflectance coefficients ($\rho(\lambda)$). For wavelengths near the fundamental absorption edge, λ= 200 − 230 nm, the photocurrent generated is given by [61]:

$$I_{(\mathrm{ph}_{\mathrm{gen}})} = I_{(\mathrm{ph}_0)}(1-\rho(\lambda))\alpha(\lambda)t, \tag{4.4.5}$$

where $I_{(\mathrm{ph}_0)}$ is the current of the incident laser pulse and t is the absorbing thickness of the detector. The photon energies used for this experiment were established above the fundamental absorption edge, which corresponds to about 5.5 eV for type IIb and IIa diamond [3]:

The measurements in a synthetic type IIa ultra-pure diamond were performed using a quintupled 5 ns neodymium-doped yttrium-aluminium-garnet (Nd:YAG) laser [14]. The energy of the pulsed photons incident on the detector was 5.6 eV, just above the band gap of the diamond which is 5.46 eV. In order to produce narrow pulse width of the pulsed photon with 5.6 eV generated in the laser and incident on the detector, a frequency-doubling β-barium-borate (BBO) crystal was applied and the width of the pulse was narrowed to 500 ps [31]. The second measurement was performed using an excimer laser that releases a pulse with width of about 20 ns. The laser pulse contained UV photons with energy of about 5.7 eV. The laser repetition rate in both measurements was about 10 Hz and the total energy of the pulse was approximately 20 μJ.

The contacts on the detector device were made of the inert metal ruthenium (Ru) with a work-function of 4.4 eV, which depends on the temperature and the chemical surface termination [37, 108]. The detector device in this case was made of a diamond containing very small concentrations of boron impurity, introduced during the growth process. Schottky contacts were deposited on the surfaces in coplanar

configuration with the barrier height at the interface enhanced by using a metal with high work-function, since the surfaces are terminated with oxygen, as described in Chapter 3 and in Ref. [37].

A set of measurements was performed using a type IIa synthetic HPHT diamond with contacts made of Ru and Ti/Pt/Au, deposited in coplanar geometry as Metal-Semiconductor-Metal (MSM). A second set of measurements were performed after the surfaces polished to remove the thin layer exposed to the beam, that could have damaged the surface and Ru was deposited in the opposite surfaces forming parallel plates as in the previous case. In all cases the contacts had the same thickness of 150 nm. The capacitance of the detector was approximately 0.54 pF. In all cases the contacts were not annealed and the electric properties were measured at low and at room temperatures.

The output pulses from the detector, with both set of contacts, induced by the incident laser pulse were recorded on a Tektronix oscilloscope with a bandwidth of 1 GHz, model TDS5104, and terminated with 50 Ω. In a second measurement, the output signals from the detector were recorder using bandwidth of about 200 MHz and were also terminated with 50 Ω. This was done in order to reduce the effect of the noise observed using the oscilloscope with bandwidth of about 1 GHz, when Ru contacts were applied. Table 4.3 summarizes the various relevant properties and parameters of the diamond device used.

In the Table 4.3, the RT is the rise time of the electronics, CRT is the cumulative rise time of the total measuring electronic system and RC is the time constant of

Table 4.3: Device and electronic parameters

Parameters	Units	Type IIa synth HPHT diamond
Area of contacts	$\times 10^{-2}$ cm^2	4.91
Thickness of the diamond	$\times 10^{-4}$ cm	460.00
Geometrical capacitance	pF	0.54
Impedance$_{\text{Electr}}$	Ω	50.00
RC$_{\text{det}}$-constant	ps	27.00
RT$_{\text{Oscl of 1 GHz}}$	ps	350.00
UV-Pulse width(1)	ps	500.00
CRT (1)	ps	610.00
RT$_{\text{Oscl of 200 MHz}}$	ns	1.75
UV-Pulse width(2)	ns	20.00
CRT (2)	ns	20.07

the detector.

The external electric field was applied to the detector at the same contact as exposed to the incident laser pulse. Charge carriers were collected from the rear contact. Therefore in order to collect holes, positive external electric-fields were applied to the detector and the electrons were collected at negative applied external electric fields.

The transient time and the charge carrier density were obtained, using the set-up shown in Fig. 4.15, and were estimated from the full width at half maximum from an average single pulse with a Gaussian distribution. For an average single pulse that displays a plateau followed by an exponential-like decay, the charge carrier density and the transient time were obtained from a 50% decay curve after the plateau [31].

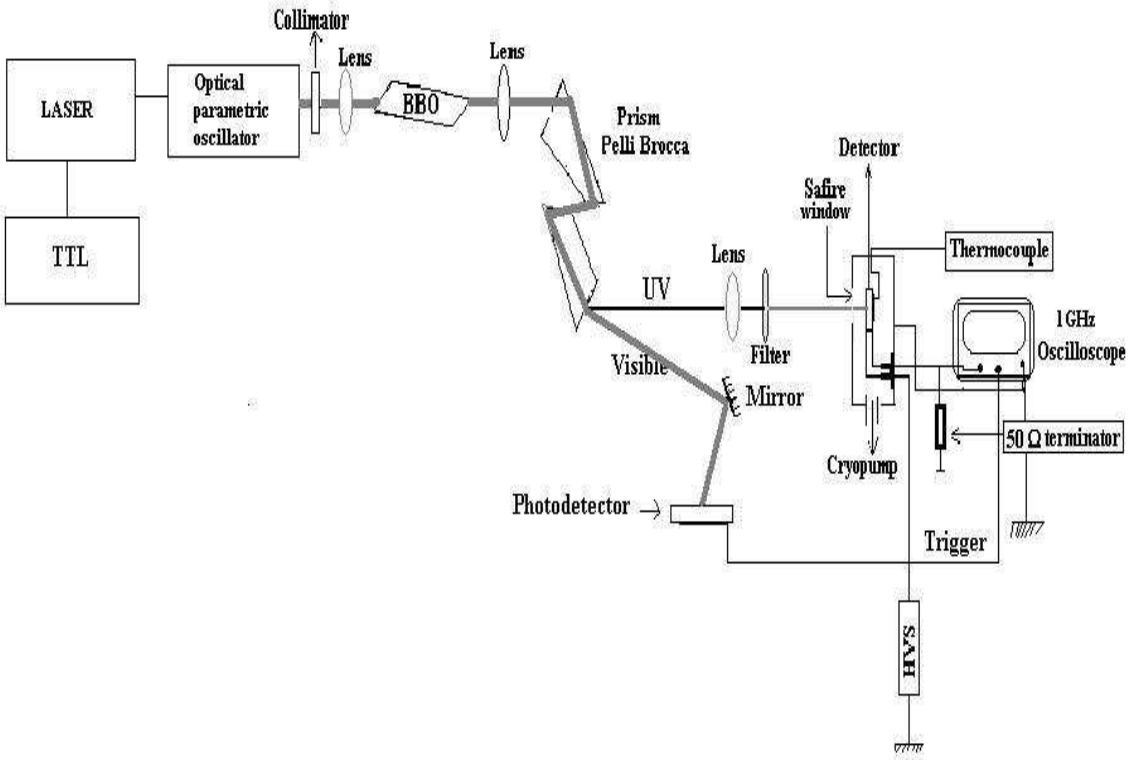

Figure 4.15: Experimental set-up used on the measurements of time of flight (TOF).

4.4.1 Contact characteristics in terms of photocurrent current density

Hole density at field saturation was measured as a function of applied external electric field at low and at room temperatures, and the corresponding resistivity was estimated using Eq. (2.5.5). The resistivities determined at low and at room temperatures with contacts made with Ruthenium (Ru) only were found to be 5.93 $\times$ 10^6 Ωcm and 1.53 $\times$ 10^3 Ωcm, respectively. In the case of contacts made as combination of Ti/Pt/Au-Ru the resistivity was measured at low temperature only to be 6.40 $\times$ 10^4 Ωcm.

The saturation field at low temperature for contacts made of Ru was approximately 741 Vcm^{-1}, while for contacts made with a combination of Ti/Pt/Au-Ru the saturation field was about 3.8 $kVcm^{-1}$. At room temperature the saturation field was approximately 328 Vcm^{-1} when Ru was implemented. In the case of Ti/Pt/Au contacts at room temperature, the saturation field was below 1.52 $kVcm^{-1}$ with a the resistivity of approximately 10^4 Ωcm. The results are summarized in Table. 4.4 and shown in Fig. 4.16.

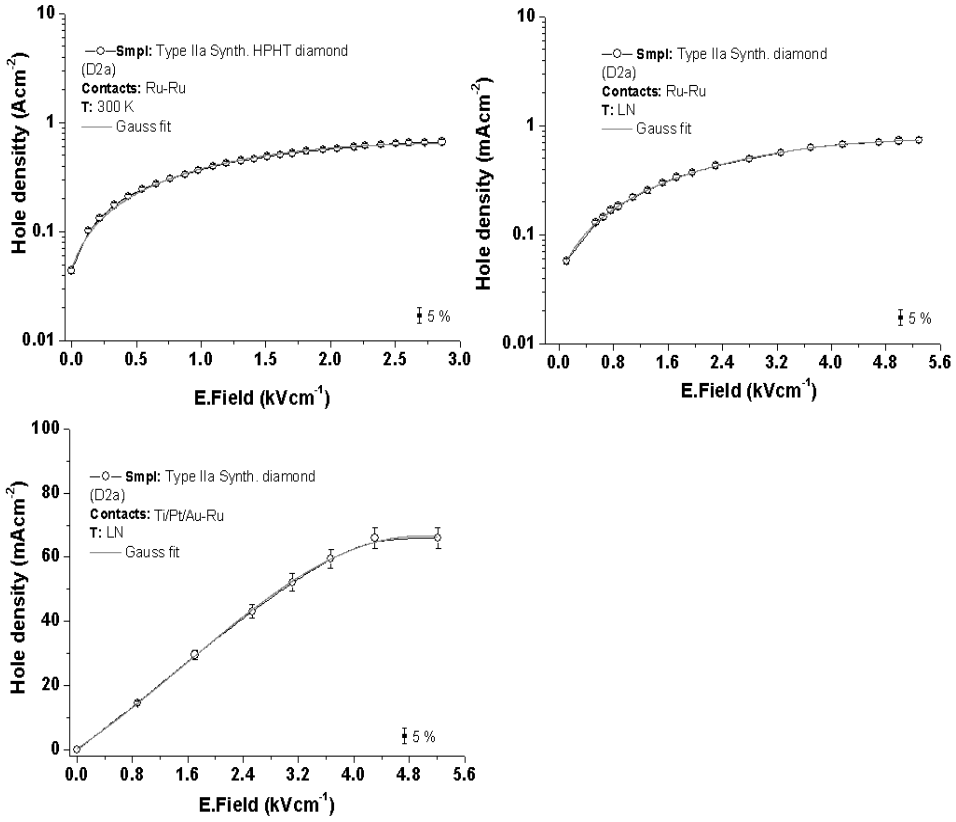

Figure 4.16: Hole density as a function of contacts at different applied external electric fields.

The difference in the resistivity between the two types of contacts is about 10^3 orders of magnitude higher at low temperature, suggesting a high value for the

Table 4.4: Resistivity as a function of contacts and temperature

Parameters	Ti/Pt/Au-Ru T:LN	Ti/Pt/Au-Ru T: 300 K	Ru-Ru T: LN	Ru-Ru T: 300 K
Saturation field (Vcm^{-1})	3.80×10^{3}	1.52×10^{3}	741.00	328.00
Hole density [Acm^{-2}]	65.88×10^{-3}	1.71×10^{-3}	0.71×10^{-3}	1.35
Resistivity [Ωcm]	6.40×10^{4}	8.8×10^{5}	5.93×10^{6}	1.53×10^{3}

barrier height when Ru-Ru is used. At room temperature differences in the resistivity values do not reflect the real properties of both contacts. The real difference is found by estimating the amount of charge released for both types contacts at maximum applied external electric fields. The combination of Ti/Pt/Au-diamond-Ru releases ten times more charge at a maximum applied external electric-field of about 1.52 $kVcm^{-1}$ compared to the amount of charge released in the case of the combination of Ru-diamond-Ru at a maximum applied external electric-field of about 2.80 $kVcm^{-1}$. This shows that in both cases, at low and at room temperatures, the combination of Ti/Pt/Au-diamond-Ru offers less resistivity and, therefore, a low value of barrier height for this type of contact.

4.4.2 Electronic properties of the device implemented with Ti/Pt/Au-Ru contacts

Average single pulses for holes and electrons densities *versus* time were acquired at LN temperature for electron and for holes, as shown in Figs. 4.17 and 4.18 at room temperature for holes, as illustrated in Fig. 4.19. The time spectrum for holes obtained at LN and at room temperatures, shown in Figs. 4.17 and 4.19, respectively, are characterised by two regimes. The first regime is represented by a sharp photocurrent peak due to the screening of the field in the electron-hole plasma [14] and

the second regime is represented by a plateau and followed by an exponential-like decay, attributed to charge carriers which survived the first recombination process and were accelerated by the external electric-field applied on the device. From the

sharp peak on the spectrum the average lifetime $\tau_{(e,h)}$ of charge carriers, was extracted and corresponds to the time that the charge carriers in the form of e-h plasma remain separated before they recombine or are accelerated by the applied external electric-field. The average transient time of the charge carriers that survive the first recombination process and were accelerated by the applied external electric-field was extracted from the 50% decay curve just after the plateau region. In addition, the time spectra of holes acquired at room temperature show long decay time, as shown in Fig. 4.19. This results from additional thermodynamic process at room temperature. At low applied external electric field and temperature, the average

single pulses of hole density *versus* time, illustrated in Figs. 4.17 b), show almost periodic fluctuations which suggest hopping conductivity. This behaviour is clearly reduced at high applied external electric-field as illustrated in Fig. 4.17 a) and by the gray line in Fig. 4.17 b). The efficiency obtained from the time spectra for

holes was extracted using Eqs. (4.4.2) and (4.4.3). This parameter is about 4% at LN temperature and 41% at room temperature. The respective mean free path is obtained from the product of efficiency and the thickness of the detector, which is 460 μm. The average pulse of electrons also obtained at low temperature is shown in Fig.4.18.

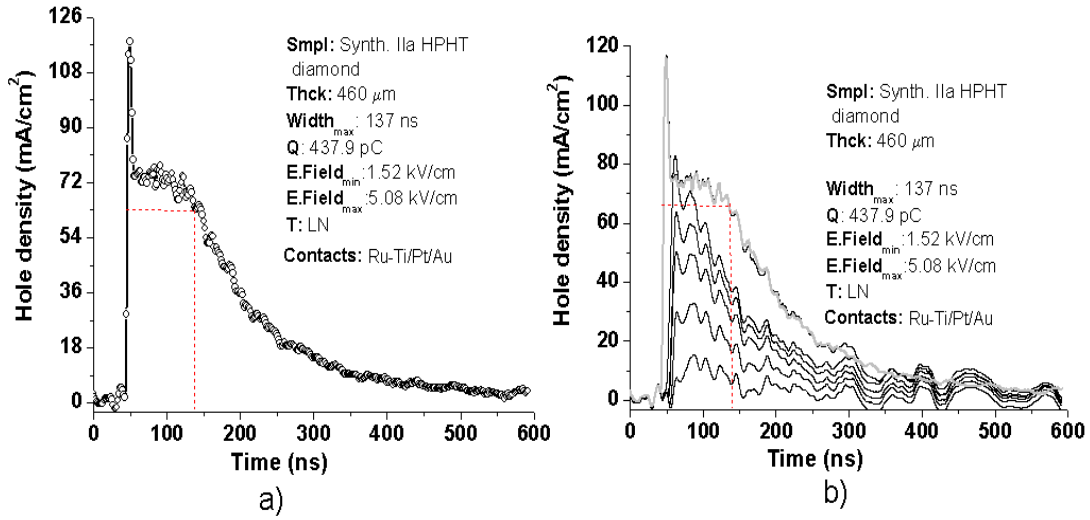

Figure 4.17: a) Hole density *versus* time at positive applied external electric-field at LN temperature at maximum applied external electric field and b) at various applied external electric fields.

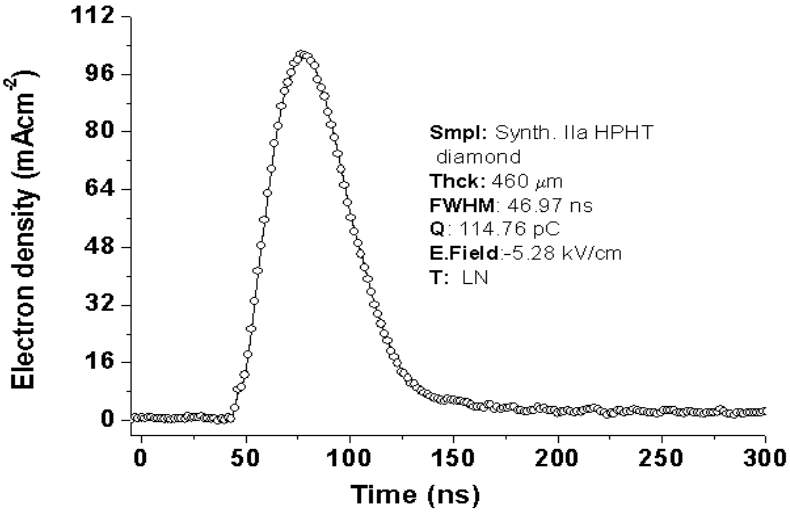

Figure 4.18: Electron density versus time at liquid nitrogen temperature.

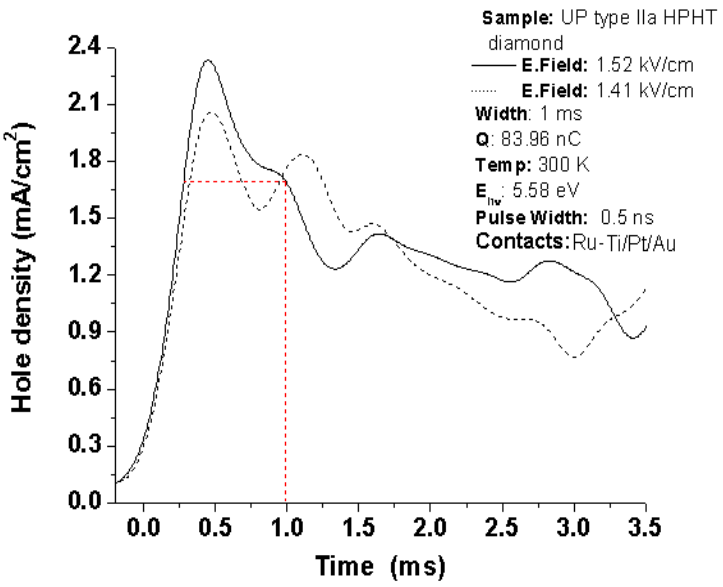

Figure 4.19: The hole density at room temperature versus time as a function of external applied positive electric-field.

The most relevant parameters were estimated to be:

- The maximum transient time τ_{t} for holes was 1 ms at room temperature,
- The life time τ for holes was 5.98 ns at LN temperature and 0.410 ms at room temperature,
- The maximum mobility was measured at LN temperature and was 10^2 $\mathrm{cm^2V^{-1}s^{-1}}$,
- $\mu\tau$ for electrons and holes were 10^{-6} and $10^{-5}\mathrm{cm^2V^{-1}}$, respectively,
- The charge carrier mean free path is 18.86 μm at LN temperature and 188.60 μm at room temperature,
- The maximum CCD for holes was obtained at room temperature and was 90.97 cm and
- The $\mu\tau_{\mathrm{h}}$ was about 10 $\mathrm{cm^2V^{-1}}$,

The results are summarized in the Table 4.5. The differences in the average single pulses of electrons and holes at liquid nitrogen temperature, results from the excess

Table 4.5: Electronic properties of the device with Schottky contacts (Ru-Ti/Pt/Au) at LN temperature

Parameters	Units	Electrons T:LN	Holes T: LN	Holes T: 300 K
E. Field	kV cm^{-1}	-5.28	5.08	1.52
Transient time (τ_t)	ns	46.59	137.00	1.00×10^6
Charge carrier density (J_d)	mA cm^{-2}	50.17	65.88	1.71
Charge carrier mobility (μ)	$cm^2V^{-1}s^{-1}$	146.93	208.00	59.85
Charge collection distance (CCD)	mm	0.36	1.45	909.70
Charge collected (Q_{coll})	pC	114.76	443.15	83960.00
Velocity (υ)	cm s^{-1}	7.75×10^5	1.05×10^6	9.09×10^4

of holes due to presence of uncompensated boron acceptors. This leads to a fast saturation of holes, at higher applied external electric-field, compared to saturation of electrons as illustrated in Figs 4.17, 4.18 and 4.19.

4.4.3 Electronic properties of the device implemented with Ru-Ru contacts

At low temperatures the time spectra of average single pulses of holes as a function of applied external electric-field are smoother when the contacts are implemented only with Ru, as previously shown in Fig. 4.20 b). This is not the case for the same temperature and fields, when the contacts are made as a combination of Ti/Pt/Au-Ru as shown in Fig. 4.17 b). The mobility for holes, however, is decreased by a factor of 10^2 and the collection of holes is also reduced by a factor 10^3. The $(\mu\tau)_h$ is of the order of 10^{-8} cm^2V^{-1}. These parameters were extracted from Fig. 4.20 a) and correspond to the maximum average single pulse as seen in Fig.4.20 b) (LN_2). The spectra on the right hand side of the same figure (LN_1) were obtained from external applied electric fields starting from values of 5.43 $kVcm^{-1}$ up to 6.74 $kVcm^{-1}$. Since

the output pulse acquired at negative applied external electric-field falls within the noise region, results of measurements for electrons are not presented. However, at room temperature the output pulse for holes is broad and shows a very short rise time, as shown in Fig. 4.21 a). At several applied external electric-fields, as shown in Fig. 4.21 b), the average pulses are smooth lines, with fluctuations only on the decay, showing a trend for a square shape which is visible by applying a logarithm to the time scale. The decay time at maximum applied external electric-field becomes shorter with an increase of hole density as illustrated in Fig. 4.21 b). The electron density *versus* time at room temperature at maximum applied external electric-field is shown in Fig. 4.22. The transient time has almost the same value as for holes and the electron density is two times lower comparing to the density of holes. The slight difference in the value of the applied external electric-field, could have influenced the results of electrons relatively to the holes.

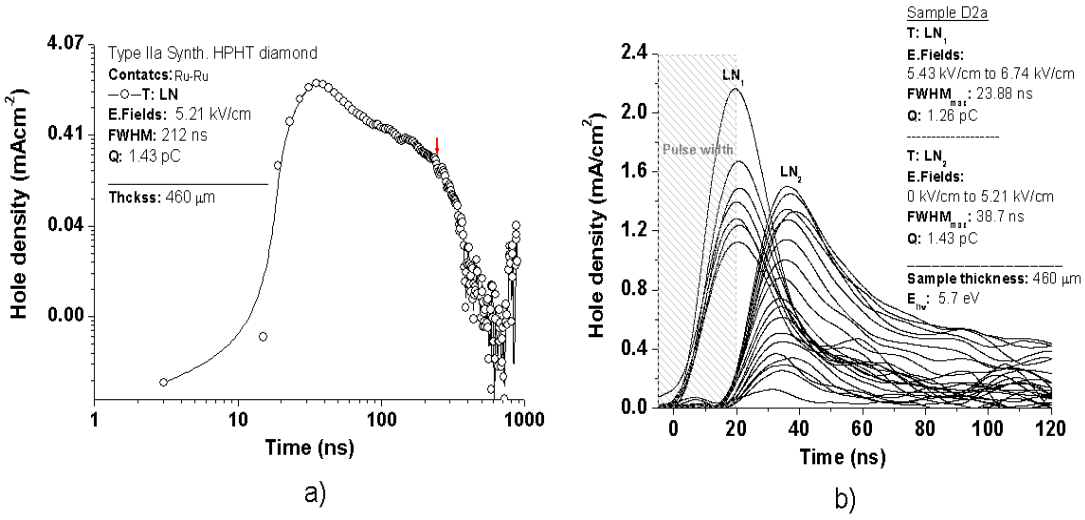

Figure 4.20: a) Hole density *versus* time at positive applied external electric field at LN temperature and b) at various positive applied external-electric field.

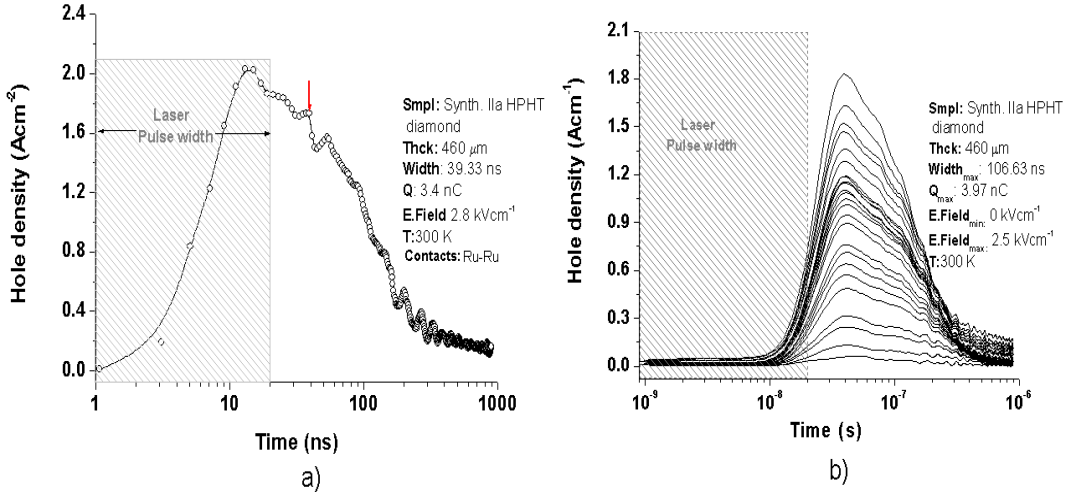

Figure 4.21: a) Hole density *versus* time of flight at positive applied external electric field at room temperature and b) at various positive applied external-electric field.

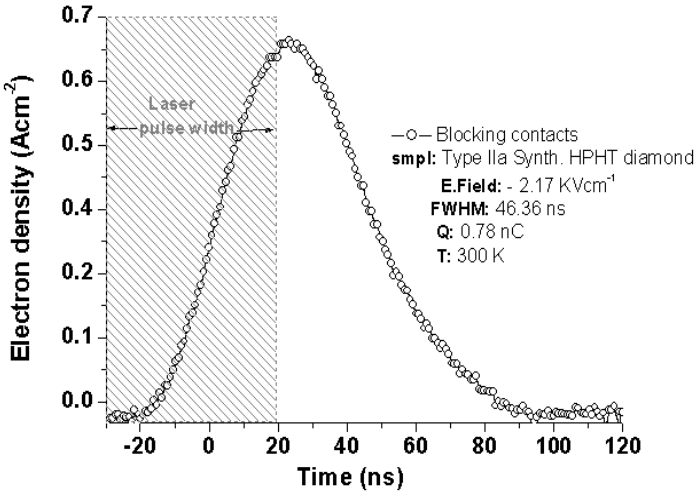

Figure 4.22: Electron density *versus* time measured at room temperatures on the device implemented with Ru contacts.

The most relevant parameters extracted with Ru contacts were estimated to be:

- The maximum hole mobility was measured at LN temperature and was about 10^3 $cm^2V^{-1}s^{-1}$,
- The maximum hole mobility was measured at room temperature and was 10^4 $cm^2V^{-1}s^{-1}$,
- The maximum hole velocity measured at liquid nitrogen temperature was about 10^4 cms^{-1},
- The maximum hole velocity measured at room temperature was about 10^7 cms^{-1},
- The maximum applied external electric field at liquid nitrogen temperature was 6.74 $kVcm^{-1}$,
- The maximum applied external electric field at room temperature was 2.81 $kVcm^{-1}$,
- The charge carrier life time at liquid nitrogen temperature was 48.77 ns,
- The charge carrier life time at room temperature was 7.75 ns,
- The mean free path at liquid nitrogen temperature was 89.73 μm,
- The mean free path at room temperature was 90.64 μm,
- The efficiency at liquid nitrogen temperature was 19. 51% and
- At room temperature was 29.71%,

The results are summarized in Table 4.6. From the results presented in Table 4.6 one

Table 4.6: Electronic properties of the device with Ru contacts

Parameters	Units	Holes T:LN	Electrons T: 300 K	Holes T: 300 K
E.Field	$kV\ cm^{-1}$	5.21	2.17	2.81
Transient time (τ_r)	ns	250.50	46.36	39.33
Charge carrier density (J_d)	Acm^{-2}	0.23×10^{-3}	0.34	1.77
Charge carrier mobility (μ)	$cm^2V^{-1}s^{-1}$	0.69	5831.52	17963.44
Charge carrier collected (Q_{coll})	nC	2.71×10^{-3}	0.78	3.43
Charge collection distance(CCD)	cm	$8.58\ \times10^{-4}$	0.58	1.97
Charge carrier velocity (υ)	$cm\ s^{-1}$	3.61×10^4	1.26×10^7	5.02×10^7

can observe that contacts made of Ru allow higher applied external electric-fields compared to the same parameter when contacts are made out of Ru and layers of Ti/Pt/Au. This leads to a high hole velocity and mobility at room temperatures, with contacts made of Ru as shown in Figs. 4.23 and 4.24, respectively. However, high hole collection distance at room temperature is achieved in the device with contacts made of combination of Ru and layers of Ti/Pt/Au. Electronic characterisations using α-particles were performed and the average single pulse of the time signal falls beyond the noise region of the oscilloscope used. However one can observe large amplitude signal with maximum of - 50 mV , as shown in Fig. 4.26, taking into account that no preamplifier was applied to the detector during the measurements. The signal was recorded on the oscilloscope directly from the detector implemented with contacts made of Ru and layers of Ti/Pt/Au, deposited on the opposite surfaces forming parallel plates. The maximum applied external electric-field to the detector was -2.17 kVcm^{-1}, being this value the maximum applied at room temperature with these contacts. The electronic properties could not be completely explored as the bandwidth of the oscilloscope available in the laboratory offered only 350 ps rise time.

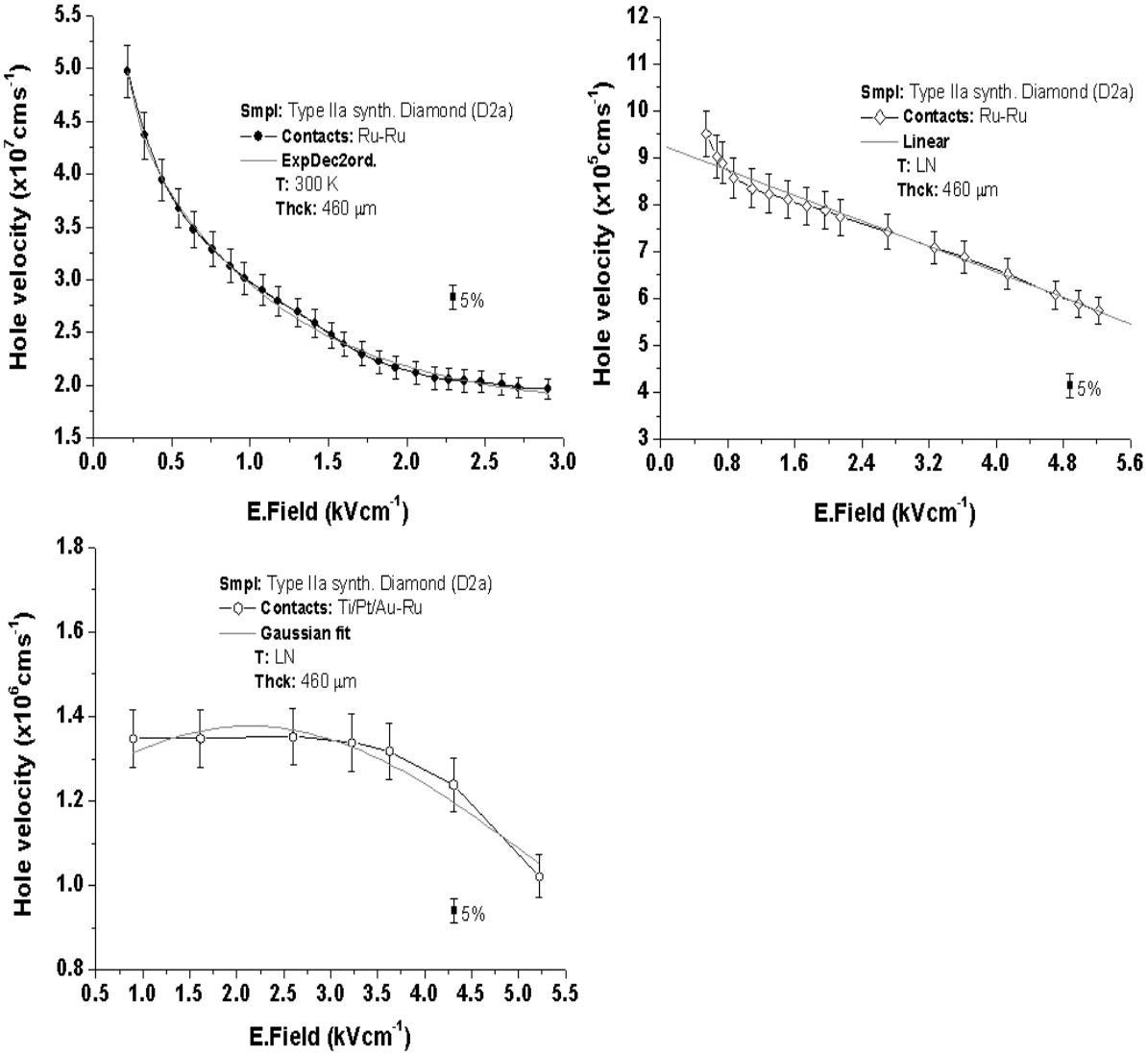

Figure 4.23: Hole velocity as a function of contacts at different applied external electric-fields and temperatures.

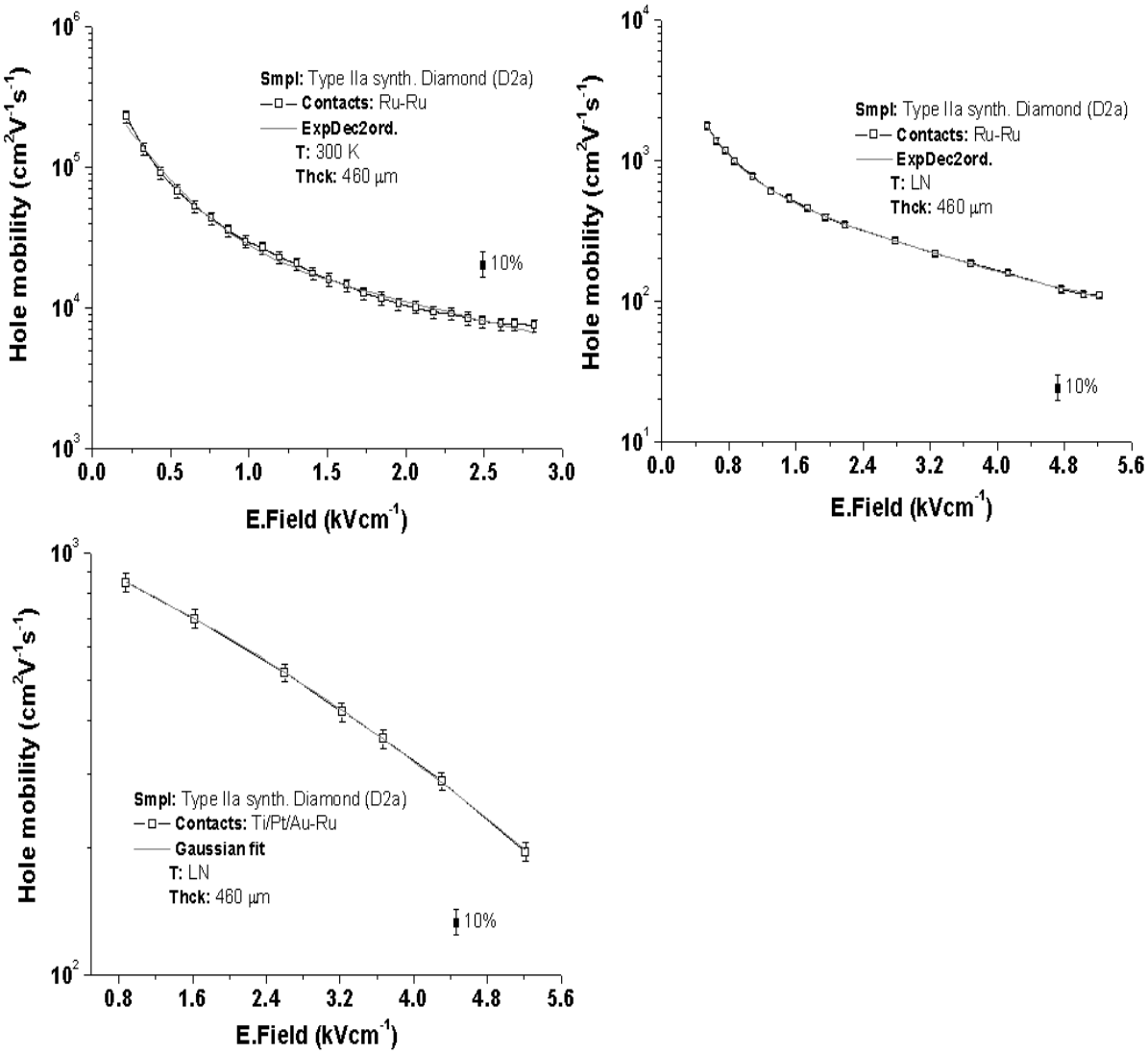

Figure 4.24: Hole mobility as a function of contacts at different applied external electric-fields and temperatures.

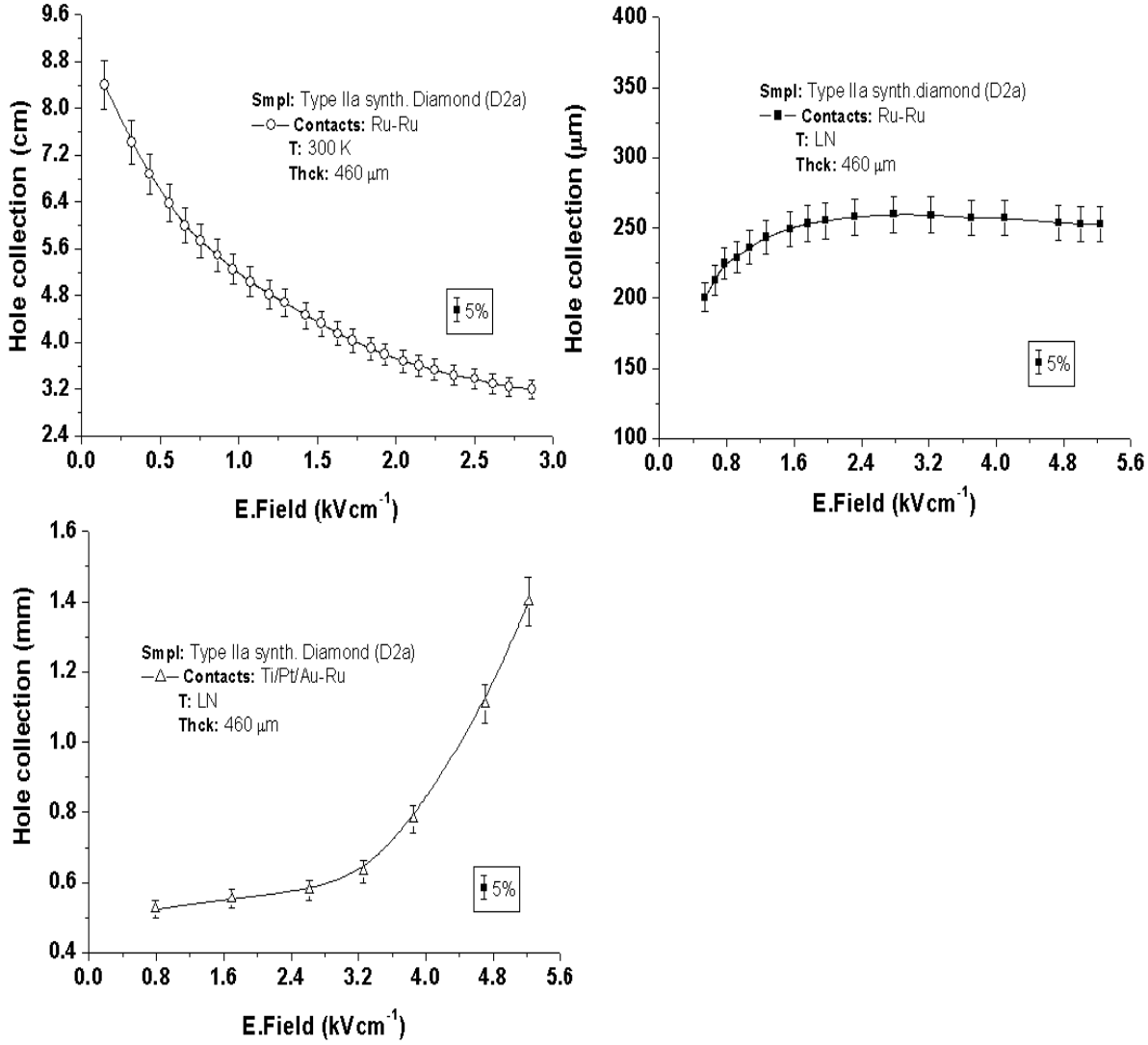

Figure 4.25: Hole collection distance as a function of contacts at different applied external electric-fields and temperatures.

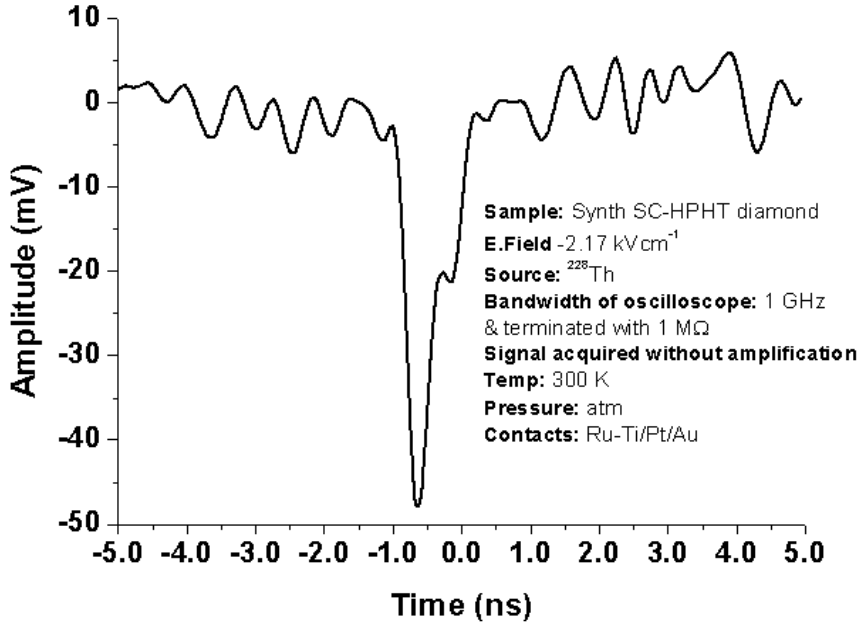

Figure 4.26: The figure shows the average single pulse, of type IIa HPHT synthetic diamond generated by α-particles from ^{228}Th. The background noise could not be totaly subtracted from the signal due to its variation with time.

4.4.4 Summary of the results

The maximum values of electronic parameters measured at room temperatures on a synthetic type IIa HPHT diamond, as function of type of contacts, are summarized in the Table 4.7.

Electronic properties of the material could not be obtained using any other method, such as the Hall effect which is a common technique used for such measurements, due to low capacitance provided by the device constructed as Metal-Semiconductor-Metal (MSM).

It must be noted that despite the fact that no amplifier was used in the measurements with relatively low energy α-particles ($<$ 9MeV), large signal amplitude and very

fast signals were collected with high signal to noise ratio.

Table 4.7: Maximum electronic parameters measured at 300 K in synthetic type IIa HPHT diamond, with the two types of contacts

Parameter	Units	Ti/Pt/Au-Ru	Ru-Ru
Applied external electric field	$kVcm^{-1}$		2.81
Transient time for holes (τ_t)	ms	1.00	
Charge carrier life time ($\tau_{e,h}$)	ms	0.41	
Hole mobility	$cm^2\ V^{-1}s^{-1}$		17963.44
$\mu_h\tau_h$ product	cm^2V^{-1}	3.00×10^{-2}	
Hole density	Acm^{-2}		1.77
Electron mobility	$cm^2\ V^{-1}s^{-1}$		5831.52
Collection of holes	nC	83.96	
Hole collection distance	cm	90.97	
Charge carrier Schubweg	cm	0.019	
Electron velocity	cms^{-1}		1.26×10^7
Hole velocity	cms^{-1}		5.02×10^7
Efficiency (η)	%	41.00	

Chapter 5

The Role of Impurities in Charge Collection and Time Properties

5.1 Introduction

A type Ib diamond containing about 50 ppm of concentration of SSN was used in order to assess the effect of this impurity on the charge collection and general electronic properties [114]. Charge collection properties in two different regions were analyzed [114, 115] in order to gain an insight on the effect of proximity of blue bands, observed with cathodoluminescence topography, on the charge collection properties. The leakage current of the detector made from this material was above the tolerance of the amplifiers used. However, the results on the charge collection in regions near the blue bands, obtained from the type Ib mentioned above should gives insight into the role of impurity compensation in different regions of the diamond. It is expected that in the region which presents yellow colour, the amount of charge collection should be highly reduced, while for regions near the blue bands the charge collection should increase slightly. The magnitude of the applied external electric field also depends on the degree of compensation.

If the blue bands observed in the cathodoluminescence measurements represent areas of uncompensated boron impurity, then larger leakage current should be observed in these regions limiting, therefore, the maximum value of applied external electric-field, resulting in discharges at higher fields. Two well defined regions of the sample separated by a distance of 2.5 mm were selected for measurement of charge collection was performed using β-particles from ^{90}Y with energy of about 2.28 MeV. The diameter of the sample was about 7.0 mm

The presence of deep impurities in the crystal such as the SSN are responsible for generation of internal fields [116], as described in Chapter 2. This leads to trapping of the charge carriers before they reach the conduction band. An electronic signal generated by a crystal containing trapping impurities is characterised by a time dependent pulse amplitude due to trapping or internal polarization effect. The signal can still be induced from the trapping site as an image charge, described by Green's reciprocity Theorem [50], but with reduced amplitude. As the polarization field continues to increase during the detection process the amplitude of the pulse reduces to a minimum possible value. The performance of a detector made of a type Ib diamond [114, 117, 118] with 46 ppm of concentrations of SSN was investigated by measuring the energy resolution using α-particles. Polarization effects and memory behaviour were also investigated. The pulses where acquired at positive and negative applied external electric fields applied to the detector and the trapping effects were investigated as a function of number of events accumulated. Memory behaviour was observed by depolarizing the device and observing the shape of spectrum and the position of the most probable charge trapped.

Timing properties of a diamond [119, 120] as a function of concentration of SSN were also investigated in two detectors made of type Ib diamonds with differences in the concentration of SSN of about 165 ppm. Alpha-particles were used to generate charge carriers [114] and the signals generated were collected using broad band electronics [120]. However, the time response in different regions of the devices could not be explored since α-particles emitted from the radioactive source used were not collimated.

5.2 Experimental procedure

The diamonds were first characterized using the electron spin resonance (ESR) technique in order to quantify the single substitutional nitrogen content [84] (see Fig. A.1). Ohmic contacts were deposited, using the same procedure as described in Section 4.2.1, on the surfaces chosen for these measurements. The deposition was performed in a coplanar geometry configuration, with an intermediate distance of about 420 μm, which correspond to thickness of the diamond. It should be noted that ohmic contacts were used in order to reduce the effect of space charge.

Charge collection properties were investigated using the minimum ionizing particles (MIP's). These were β-particles with energy of 2.28 MeV, emitted by the daughter product of ^{90}Sr source (^{90}Y) with a life time of about 72 h. The ^{90}Sr source with a collimator of a diameter 0.3 mm was placed on the top of the detector in order to increase the solid angle between the incident particles and the surface of the detector. Two different regions of the specimen, namely the center and the region near the

edge, with a distance of 2.3 mm from each other, were probed in this manner. A plastic scintillator was aligned behind the diamond detector, as seen in the schematic diagram of the experimental set-up shown in Fig. 5.1. The signal generated in the detector was triggered by the signal generated in the plastic scintillator, which results from the same charged particle that traversed the diamond detector. The signals generated from MIP's obtained from the type Ib diamond detector using the set-up illustrated in Fig. 5.1 are shown in Fig. 5.2.

The memory behaviour of the sample was investigated using α-particles and positive and negative external electric-fields applied to the detector. The measurement set-up for this experiment consisted of the self-triggering system shown in Fig. 5.3. When the amplitude of the signal generated in the detector deteriorates due to increase on the space charge effect, the electric field was turned off. The space charge accumulated in the device was then released by bombarding the detector with charged particles from the same radioactive source. The signal from the detector was acquired through a very low noise, of 25 μV, home made charge sensitive preamplifier (CSA) [121]. The gain in this device was about 325.15 $\mu V/e^-$ with an impedance of 100 MΩ and was terminated with 50 Ω resistance.

The time properties of a diamond detector as a function of concentration of SSN were investigated using α-particles from ^{241}Am and from the mixed nuclide source (^{239}Pu, ^{241}Am, ^{244}Cm) sources. The time signals were acquired through a fast amplifier, a two stage GaAs monolithic microwave integrated circuit (MMIC), with a bandwidth of about 2.3 GHz with - 3 dB bandwidth (built at the GSI laboratory) [120].

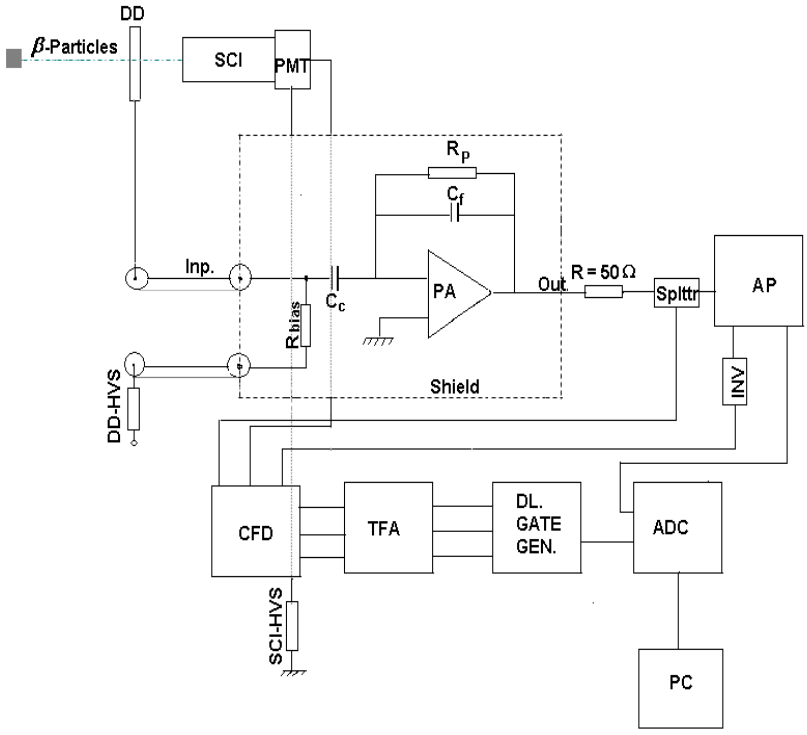

Figure 5.1: Electronic set-up used to measure the charge collection, using MIP's. The individual components are: DD is the diamond detector, DD-HVS is the high, voltage supply to the DD, SCI is the plastic scintillator (N/A in self triggering mode), PMT is the photomultiplier connected to the SCI, the shield protects the signal amplification system from external noise, R_{bias} is the resistor in the amplification through which the circuit the DD is biased by the HVS, C_c is the coupling capacitance, PA is the preamplifier, R_P is the shunt resistor for the current noise, C_f is the fed back capacitor, Spltter is the signal splitter, INV is the signal inverter, CFD is the constant fraction discriminator, TFA is the timing filter amplifier, DL GATE GEN is the delay gate generator, ADC is the analog to digital converter and PC is the computer for data processing.

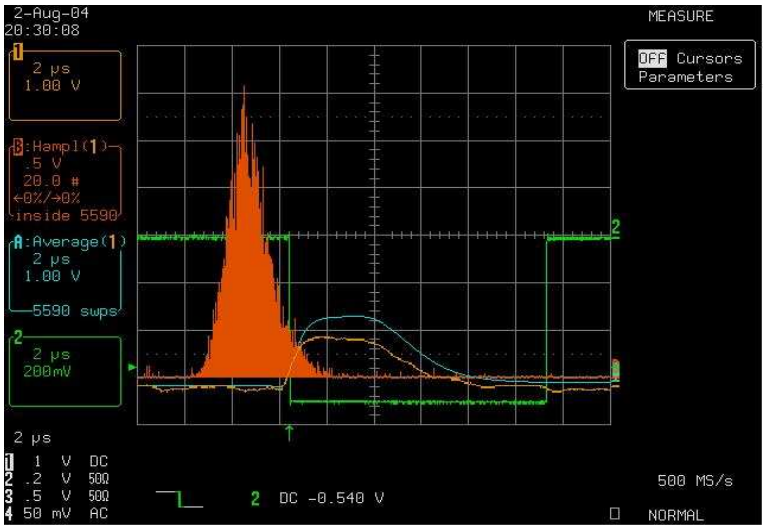

Figure 5.2: The electric signals generated by MIP's in the detector made of type Ib diamond, using the set-up in Fig. 5.1. In dark orange is the spectrum of MIP's, the signal in light orange is the single pulse, the signal in blue is the average single pulse and the signal in green is the signal from the discriminator.

The induced charge signal from the amplifier is given by the following relation [121]:

$$ne_{\text{ind}} = \frac{U_{\text{out}}}{G}, \tag{5.2.1}$$

where U_{out} is the output amplitude signal from the preamplifier, G is the gain of the amplifier and the corresponding unit is given in $\frac{\mu\text{V}}{\text{e}^-}$ [121].

Set-up for measurement in self triggering mode

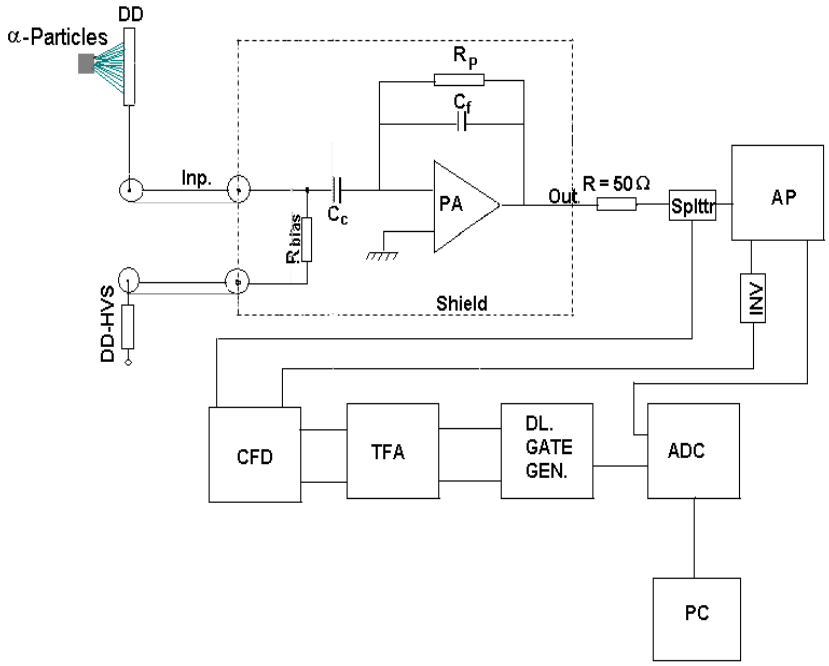

Figure 5.3: Electronic set-up to measure energy resolution, in self triggering mode.

Set-up for time measurement

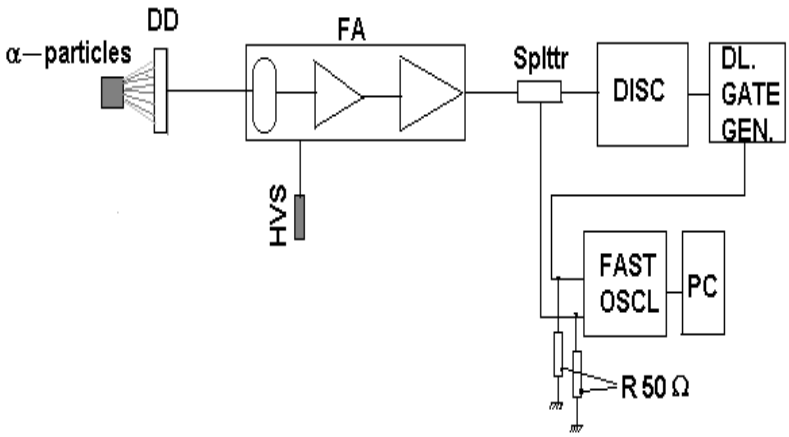

Figure 5.4: Schematic diagram for fast acquisition using broad band amplifier, [120]. DD is the diamond detector, FA is fast amplifier, DISC is signal discriminator and FAST OSCL is the 1.5 GHz bandwidth oscilloscope used.

The noise figure for this amplifier was 2.5 dB. Signals were recorded by a LeCroy oscilloscope with a bandwidth of 1.5 GHz as shown in Fig. 5.4. For these experiments two detectors with 50 ppm and 215 ppm concentration of SSN were investigated. A timing spectrum is also acquired to discriminate the peaks observed in the average single pulses [120].

5.2.1 Results and discussions

Charge collection in different regions of the diamond

In the center region of the sample, defined as Region 1, charge collection showed a very small variation in the most probable charge collected as a function of applied external electric field. The maximum value of this parameter was achieved at applied external electric-field of -30 kVcm^{-1} and was about 2500 e^{-}. This corresponds to the most probable charge collection distance of 70 μm, with an efficiency of 17%. The spectra of MIP's corresponding to the region 1 as a function of applied external electric field is shown in Fig. 5.5.

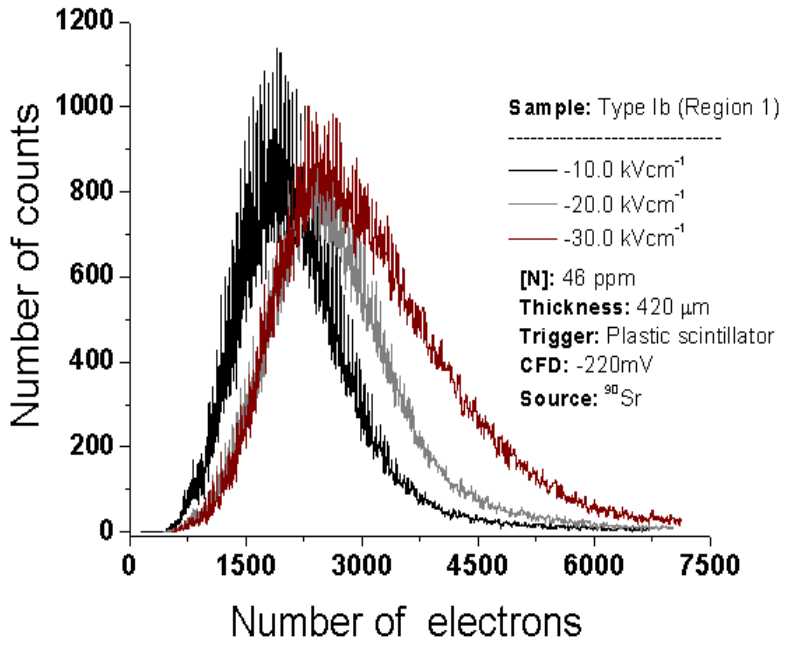

Figure 5.5: Charge collected as a function of applied external electric field at the center of the sample, Region 1.

Near the edge region of the sample defined as Region 2 (near the blue bands), the maximum negative applied external electric-field was -20 kVcm^{-1} and the most

probable charge collected is twice of that collected at fields of about -10.00 kVcm^{-1} in the same region. This parameter is only limited by the leakage current which increases with field in this region. The maximum value of the most probable charge collected was 5000 e$^-$ with a charge collection distance of 130 μm. This corresponds to an efficiency of 31%, which is two times higher than the efficiency in Region 1 at an applied external electric-field of -30 kVcm^{-1}. The spectrum of the MIP's in the region 2 as a function of applied external electric field, is shown in Fig's. 5.6 and 5.7. The charge collection distance as a function of applied external electric field is shown in Fig. 5.8. The results are summarized in Table 5.1.

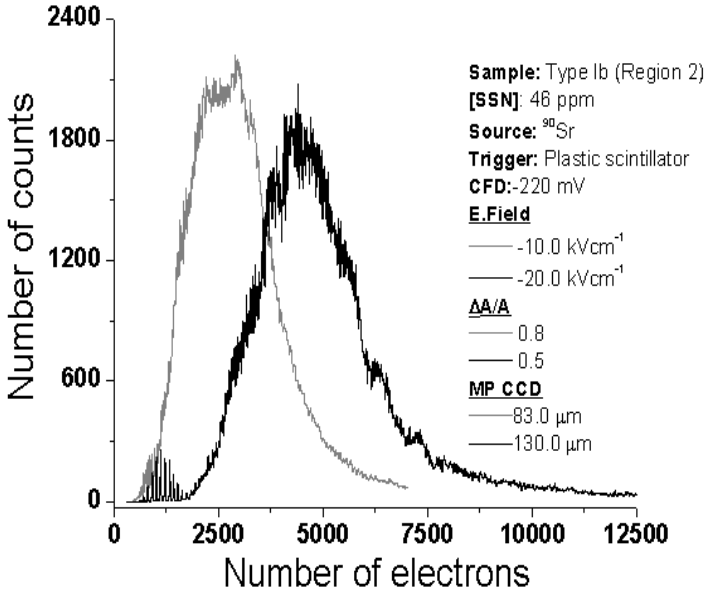

Figure 5.6: Charge collected as a function of applied external electric field at the edge of the sample, Region 2. In this figure, the noise region at high applied external electric field is observed.

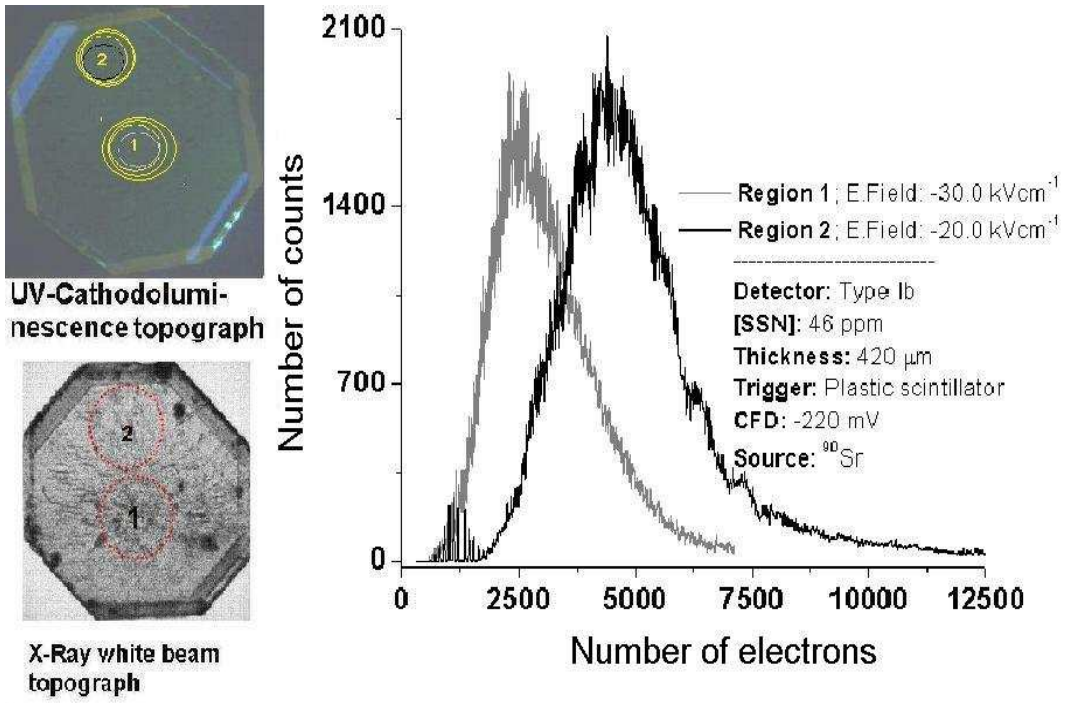

Figure 5.7: Variation of the most probable charge collection at the maximum applied negative external electric fields in the Regions 1 and 2. From the X-ray white beam topograph of the sample, also shown in this figure, it is possible to observe the differences in the density of defects between these two regions, which might be a sign of differences in the concentration of impurities and their compensation. This aspect also influences the electric response of these two regions.

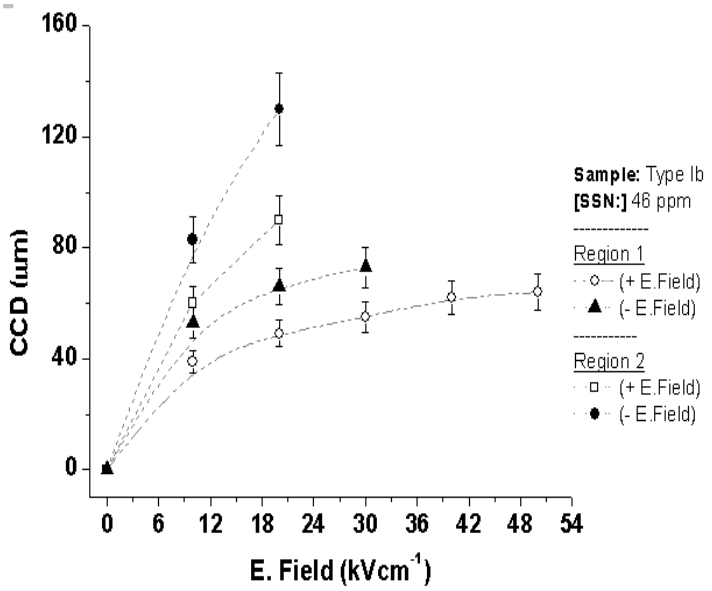

Figure 5.8: Charge collection distance *versus* applied external electric field, in the two regions of the diamond.

Table 5.1: Electronic properties as a function of defects

Region	E.Field ($kVcm^{-1}$)	MPCC 1) (e^-)	CCD 2) (μm)	η 3) (%)
Center	−30.00	2500.00	70.50±0.50	17.00
Edge	−20.00	5000.00	130.00±0.50	33.00
Center	50.00	2100.00	58.00±0.50	13.80
Edge	20.00	3060.00	85.00±0.50	20.23

1. MPCC is the most probable charge collected at the electrodes,
2. CCD is the charge collection distance and
3. η is the efficiency of the device .

5.2.2 Memory behaviour

The energy spectra generated by α-particles were acquired at positive and at negative applied external electric-fields. To observe the effect of polarization, the spectra were

acquired and recorded as the number of events increased.

At positive applied external-electric field, the polarization effect is almost an instantaneous effect. However, there is still a relatively large charge collection signal, as shown in Fig. 5.9 compared to the same parameter at negative applied external electric-field. This is a result of collection from the front-electrode near the region where the total energy is deposited, since the range of α-particles from a ^{241}Am source is 12 μm in diamond.

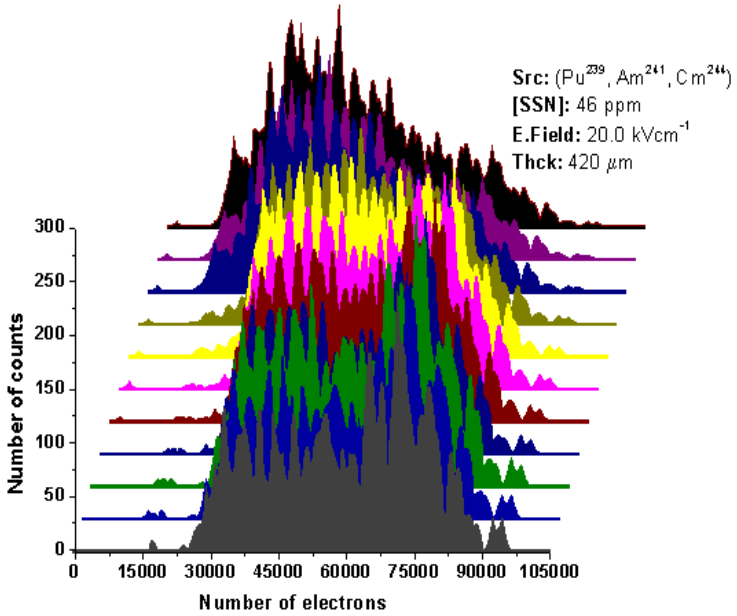

Figure 5.9: Variation of the signal charge with number of events generated at positive applied external electric field.

At zero applied external electric-field under the influence of α-particles the detector exhibits depolarization. The pulses are of negative polarity and the shape of the spectrum, see Fig. 5.10, resembles the spectrum acquired at positive applied external electric-field before polarization effects take place.

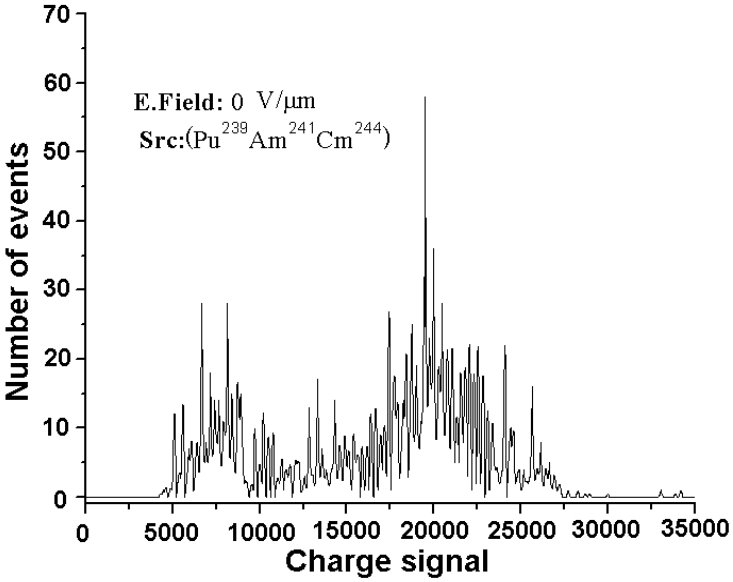

Figure 5.10: The spectrum acquired at zero volts, shows charge stored at positive applied bias voltage.

At negative applied external electric-field the charge signal is very small, see Fig. 5.11. This is due to charge collection over long distances since the charge carriers travel to the opposite electrode, far from the region where the total energy of the α-particles is deposited. The shape of the charge collection signal does not change over the number of events as in the case of positive applied external electric-field. The differences between the negative and positive applied external electric-fields result from the fact that large number of charge carriers are generated by a single ion deposited. In the presence of defects, these charges generate clouds of polarized sites that result in the fluctuation of the applied external electric field in the device. The effect is immediately observed near the contact where the total energy is deposited, as a shift in the spectra from a higher to lower charge signal, as the number of events increases. At negative applied external electric-field this shift is not observed

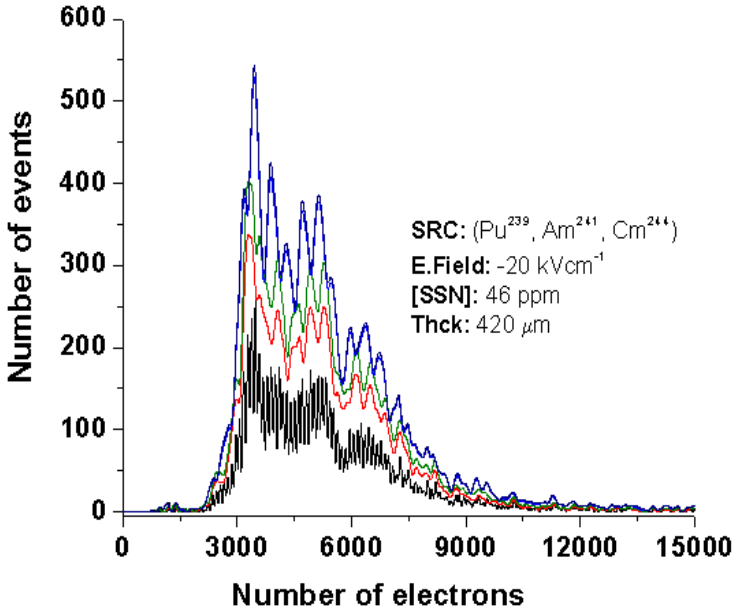

Figure 5.11: Variation of the signal charge with number of events generated at negative applied external electric field.

since the number of charge carriers that reach the opposite electrode is constant and is regulated by the clouds of polarized sites producing fluctuations in the applied external electric field.

When the field is turned off and the detector is exposed to the radiation from the same source, the shape of the depolarization spectrum, see Fig. 5.12, also resembles the spectrum acquired at negative applied external electric-field. It should be noted that depolarization using β-particles from a ^{90}Sr source, after irradiation with α-particles from ^{241}Am, is less effective. This suggests that the effective depolarization is possible only with equivalent polarizing energy. On the other hand, the polarization due to irradiation with β-particles from ^{90}Sr source is negligible. One can see from the shape of the spectrum (Fig.5.10) that the polarization probability is reduced in the direction of the opposite electrode. The polarization charges

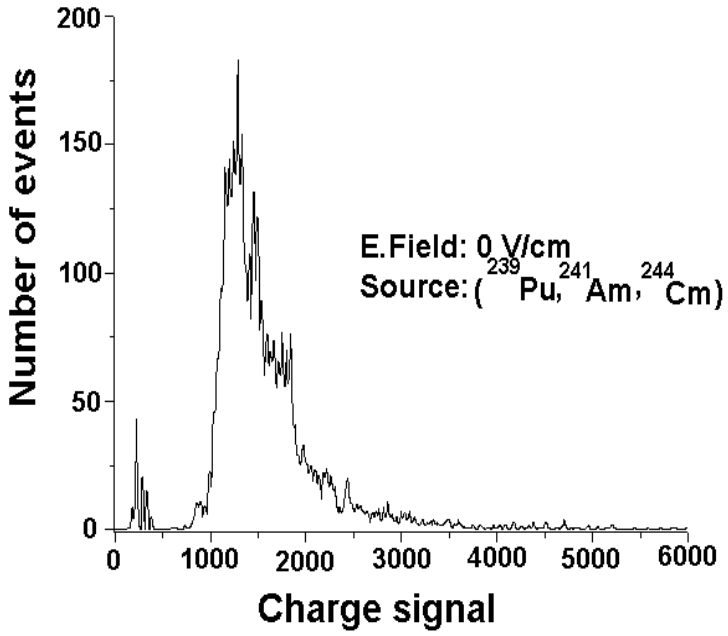

Figure 5.12: The spectrum acquired at zero volts, shows charge stored at negative applied bias voltage.

correspond to the high charge collection probability, as shown in Fig. 5.9. This results from the lower charge collection in comparison to the top electrode.

5.2.3 Time properties as a function of concentration of SSN

The timing properties as a function of concentration of SSN was investigated for two type Ib samples with 50 ppm concentration of SSN (sample D1) and 215 ppm concentration of SSN (sample D2). The average single pulses and the spectra from both detectors were compared using α-particles were used. Due to space charge effects which results in non accurate amplitudes of the average single pulses corresponding to both detectors, the amplitudes were normalized. A logarithmic scale on the corresponding timing spectra of both detectors was used to allow a better

interpretation and comparison of the timing features of both detectors.

The geometric capacitance of both detectors is mostly determined by the thickness of the crystals, for sample D1 being 310 μm and for sample D2 120 μm. The contacts for both detectors had areas of 0.0491 cm^2. Using 50 Ω termination for the electronic system and multiplying with the capacitance of the detectors, the RC-constant of detectors D1 and D2 were found to be 40 ps and 102 ps, respectively.

The average single pulses of the two detectors shown in , Fig. 5.13, exhibits three peaks. Differences with respect to the rise time of the signals were observed as a result of the differences in time constant (RC-constant) of the detectors. The time spectra, see Fig. 5.14, of the average single pulses display clearly the three peaks apparent in the average pulses (Fig. 5.13).

The first peak in the time spectra corresponds to the cumulative rise times of the active electronic system, including the RC-constant of the detector.

The second peak, occurring at 1 ns, results from the screening of the field in the electron hole plasma [14]. It represents a fast extraction from the front contact [31] since the α-particles stop 12 μm away from the front contact.

The third peak is the transient time of the charge carriers, which survived the trapping and recombination processes during the energy deposition. These charges traveled a certain distance during certain time t_t towards the electrodes under the influence of the applied external electric-field. The differences in the transit times between both detectors is about 70 ps.

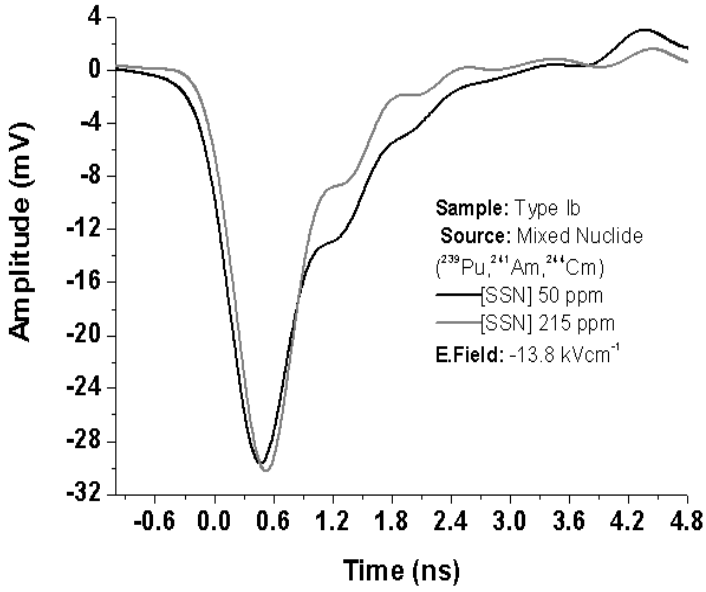

Figure 5.13: Pulse heights of two detectors with different concentrations of the SSN, normalized due to effect of space charge.

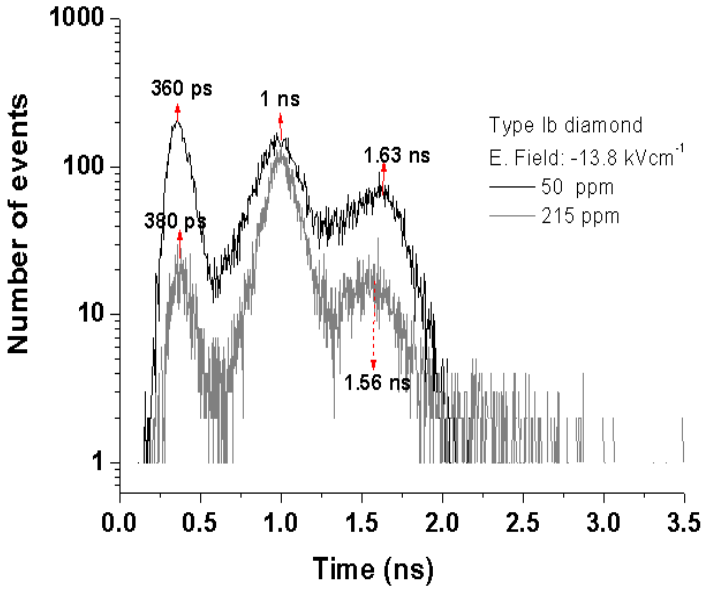

Figure 5.14: Time spectrum of two detectors as a function of concentration of SSN.

Time properties as a function of applied external electric-field

In order to assess the effect of the external applied electric-field on the timing properties of a type Ib (sample D2) with a concentration of SSN of 215 ppm was used. An increase in the applied external electric-field decreases the amplitude of the noise peak which corresponds to the first peak in the spectrum, as seen in Fig. 5.16 which correspond the spectra shown on Fig. 5.15.

The occurrence in time, about 1 ns, of the second peak in the spectra remains unaltered with variation of the applied external electric-field.

The third peak corresponding to the decay time increased to 100 ps when the external applied electric-field was -13.8 kVcm^{-1}. This very small increment is consistent with the presence of high concentrations of deep trapping impurity.

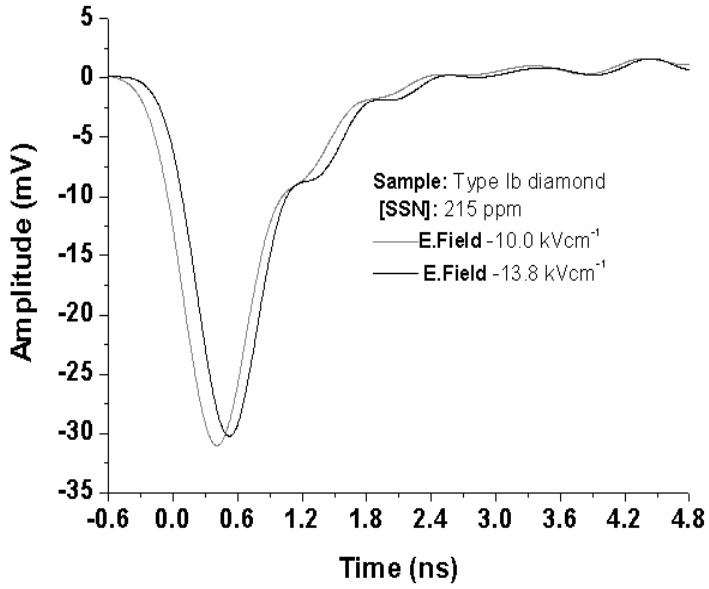

Figure 5.15: Pulse height as a function of applied external electric field.

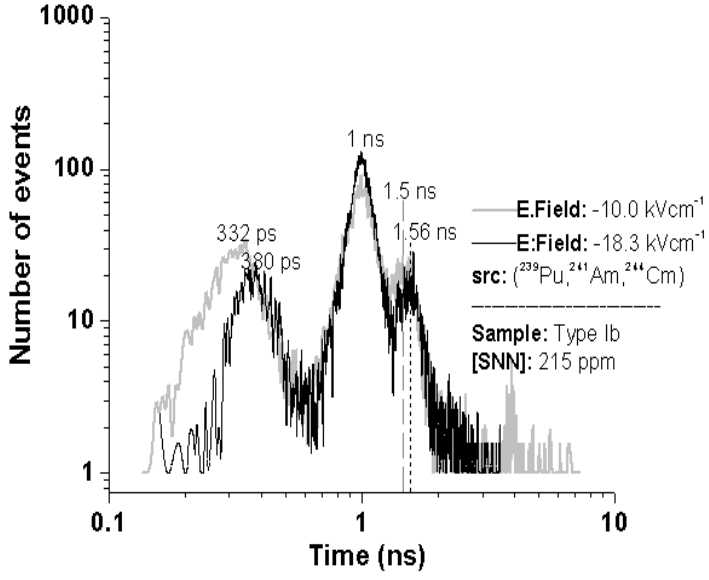

Figure 5.16: Time spectrum as a function of applied external electric field.

5.2.4 Differences in the pulse heights and time spectra generated by two different α-particle sources

No difference was found between the pulses generated by α-particles from the three mixed nuclides source and from the mono-energetic source, as shown in Figs. 5.17 and 5.18. The results are summarized in Table 5.2.

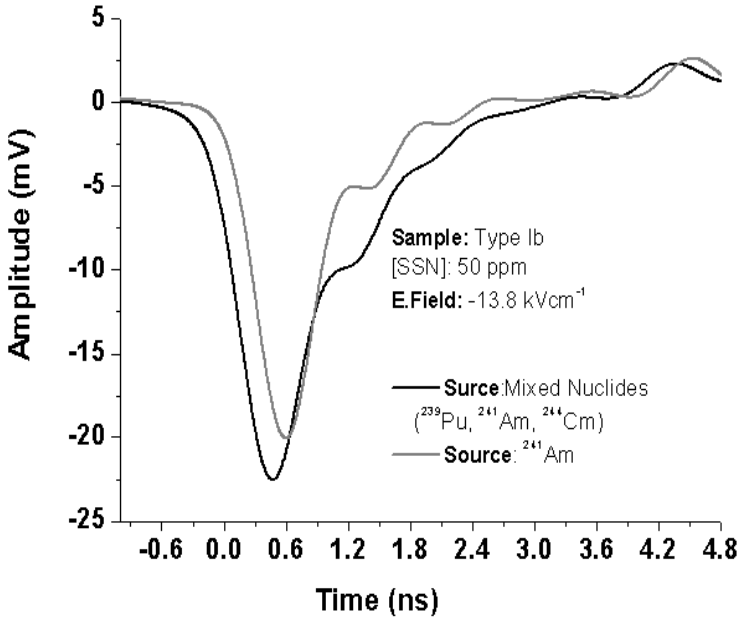

Figure 5.17: Pulse heights generated by a mono-energetic source and by a three mixed nuclide source of α-particles

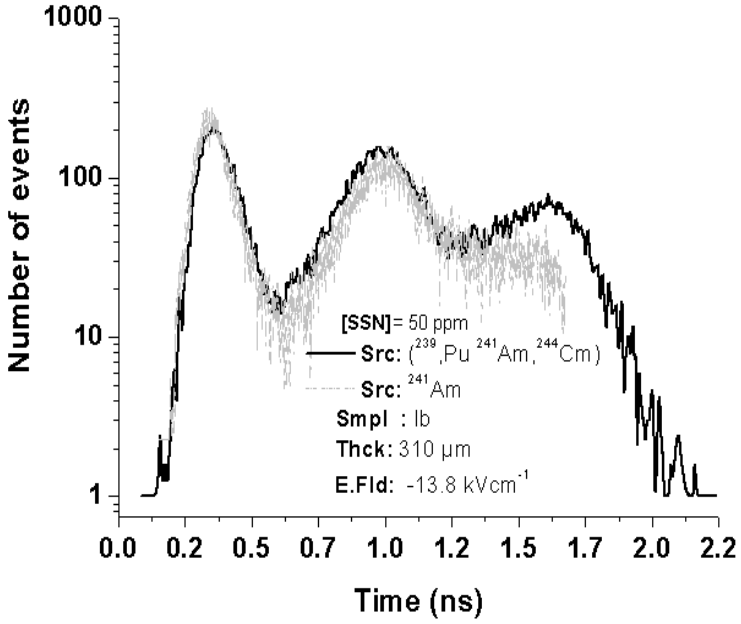

Figure 5.18: Spectra of the above signals generated by a mono energetic source and by a three mixed nuclide source of α-particles.

Table 5.2: Effect of concentration of SSN on the rise and decay times

SSN 1) [ppm]	Thickness [μm]	RC-const 2) [ps]	CCRT 3) [ps]	E.Field [kVcm^{-1}]	E.Noise [ns]	RT 4) [ns]	DT 5)
50 (D1)	310.00	40.00	281	-13.80	332	1.00	1.60
215 (D2)	120.00	102.00	300	-13.80	380	1.00	1.50

SSN is the single substitutional nitrogen

1. RC-constant is the time constant of the detector,
2. CCRT corresponds to the calculated cumulative rise times
3. RT is the rise time estimated from the spectra
4. DT is the decay time or the transit time of the charge carrier under the effect of the applied external electric field.

5.2.5 Summary

Charge collection in different regions of the diamond

The central region of the type Ib diamond, with a concentration of SSN of 46 ppm, exhibits low collection efficiency, while in the region near the edge the collection efficiency is nearly double. It should be noted that the center of this diamond sample contains a relatively high density of lattice dislocations, which could be the result of the higher concentration of SSN compared to the region near the edge. The region near the edge is also influenced by small concentrations of uncompensated boron acceptors, observed as blue bands on the edges. This limits the amount of external electric field that can be applied.

Memory behaviour

The memory behaviour observed in the type Ib diamond with 46 ppm of concentration of SSN is mostly related to the effect of polarization due to the presence of crystallographic defects. This means that any diamond can generate the same behaviour when polarizing defects are present. On the other hand, long exposure to radiation or high energy losses, may also cause similar behaviour.

Time properties as a function of impurity concentration

The presence of three peaks in the time pulse of both detectors independently of the amount of applied external electric field, concentration of impurities and total energy deposited, results from: 1) cumulative rise times of the total electronic system used, 2) fast extraction from the front contact due to plasma generation and 3) the

extraction from the back contact, which is considered the life time of the charge carrier across the bulk, under the influence of applied external electric field.

Chapter 6

Conclusion

6.1 Summary of the results

A summary of the most significant findings in this study is provided with respect to characterization of impurities and defects and the evaluation of electronic properties of high-purity synthetic HPHT diamond of different types.

The adiabatic rapid passage (ARP) method of the electron spin resonance (ESR) technique was employed in order to determine the approximate concentration of SSN in synthetic type IIa HPHT diamond. The lower spin population in the deep energy level introduced by SSN dictated the use of this method. In addition to information regarding the SSN center the results obtained from this characterisation became an important tool in order to evaluate the possible concentrations of boron impurities and study aspects of boron-nitrogen compensation, otherwise difficult to determine with other spectroscopic tools.

Boron impurities present in the samples studied, although at very low concentrations, were not compensated, and constituted the main cause of significant conductivity in the diamond.

The low activation energies extracted using the current-deep level transient spectroscopy (I-DLTS) have been attributed to low compensation of boron rather than simply its presence in the crystal.

The influence of reduced concentrations of SSN and the distribution of uncompensated boron acceptors and its influence on the electronic properties of diamond were also investigated in a type Ib diamond. The sample contained 50 ppm of concentration of SSN. The presence of uncompensated boron acceptors, determined by cathodoluminescence topography, was found to be higher at the edge of the material as in the case of a synthetic type IIa HPHT diamond. The measured charge collection properties shows about 100% increase by comparison to the central region of the sample, with the applied external electric-field being about ten orders of magnitude less than the value applied at the center of the sample.

6.2 Conclusion and outline of the results

The performance of a detector device using Schottky contacts made with two different combinations of metal layers, namely Ti/Pt/Au-Ru and Ru-Ru was investigated. The time of flight technique (TOF) was employed in this case, incorporating a laser setup with photons having energies above the diamond band gap. The device was constructed as metal-semiconductor-metal (MSM), coplanar structure, with no implantation of a resistive layer. The contacts were not annealed in order to reduce the tunnelling probability. In this way, when the detector is made as Ti/Pt/Au-diamond-Ru device, a high charge-carrier mean separation is achieved due to the

photo interaction. The respective mean time separation, the charge collection properties as a function of applied external electric fields, and the respective transient times are obtained. On the other hand, when the detector is made as Ru-diamond-Ru device, then high values of charge carrier density, mobility and velocities are achieved at both low and room temperatures.

The device construction did not contemplate the guard ring due to the small area of the device. The guard has an effect of reducing the amount of leakage current due to surface conductivity at high applied external electric field. Other techniques to evaluate the electronic properties of the diamond such as Hall effect measurement, was not implemented due to low capacitance of the device.

It was difficult to assess the effects due to charged particle irradiation on the detector made as Ti/Pt/Au-diamond-Ru, due to limitations related to the electronic equipment available. However, signals obtained from α-particles from a ^{228}Th source even without amplification (see in Figs 4.26 and A.13), provides an insight into the good electronic properties of the material.

The Tables 6.1, 6.2 and 6.3, summarize most of the findings in terms of SSN concentrations, energy levels and the capture cross-sections of boron acceptors introduced in the sample, and the electronic properties under various conditions. It was found that the average concentration of SSN in all three synthetic type IIa HPHT diamonds, investigated in this work, was $\leq 10^{13}$ atoms cm^{-3}. These results are summarized in the Table 6.1.

Table 6.1: SSN concentration in a synthetic type IIa diamond

Sample type	mass (mg)	Peak intensity ($\times 10^6$)	SSN ($\times 10^{13}$ spins cm^{-3})
IIa HPHT Synthetic diamond (D2)	79.00	10.00	6.85
IIa HPHT Synthetic diamond (D3)	63.00	$\leq$10.00	0.11
IIa HPHT Synthetic diamond (D4)	59.00	12.50	6.40

Table 6.2: Activation energies and the capture cross sections of boron impurity in synthetic type IIa HPHT diamond

B	$E_{a_{\text{near-center}}}$ [eV]	$\sigma_{\text{near-center}}$ [$\times 10^{-15}$ cm^2]	$E_{a_{\text{center}}}$ [eV]	σ_{center} [$\times 10^{-15}$ cm^2]	$E_{a_{\text{edge}}}$ [eV]	σ_{edge} [$\times 10^{-15}$ cm^2]
1	0.308	28.360	0.311	29.111	0.254	0.641

Table 6.3: Electronic properties of a type IIa syntheticHPHT diamond at 300 K.

Parameter	Units	Holes Ti/Pt/Au-Ru	Holes Ru-Ru
Applied external electric field	kVcm^{-1}	1.52	2.81
Saturation field	Vcm^{-1}	$\ll$100	328.00
Contacts resistivity	$\times 10^6$ Ωcm	$\ll$1.00	0.88
Transient time for holes τ_t	ms	1.00	39.33×10^{-6}
Charge carrier life time $\tau_{e,h}$	ms	0.41	7.77×10^{-6}
Hole mobility	cm^2 V^{-1}s^{-1}	59.85	17963.44
$\mu_h\tau_h$	cm^{2}V^{-1}	5.98×10^{-2}	7.06×10^{-4}
Hole density	Acm^{-2}	1.71×10^{-3}	1.77
Collection of holes	nC	83.96	3.43
Hole collection distance	cm	90.97	1.97
Charge carrier Schubweg	μm	188.60	90.64
Hole velocity	cm s^{-1}	9.09×10^4	5.02×10^7
η	%	41.00	29.71

By using the I-DLTS method it was possible to extract the energy levels in three different regions of the diamond and the respective capture cross sections. The highest hole-collection distance achieved is about 91 cm with a respective transient

time of about 1 ms. The highest hole mobility and velocity achieved were 17963.44 $cm^2\ V^{-1}s^{-1}$ and $5.02\times10^7\ cms^{-1}$, respectively.

Further investigation on the electronic properties will be performed using weak semiconducting synthetic type IIa diamond, which includes selection of metals and alloys to establish appropriate electrodes, analysis of the barrier heights as a function of electrodes applied and compensating factor of impurities in the material, surface morphology, chemical composition and radiation hardness.

The ultimate goal is to explore the potentials offered by presence of small concentration of uncompensated boron impurity in the material in order to produce a highly improved particle detector, built in a coplanar geometry as metal-semiconductor-metal (MSM), with very good energy resolution, producing very fast signals with high amplitudes, which implies very good signal to noise ratio. A device operating at room temperature should perform with minimal signal amplification requirement. The expectation then of a device with good performance is that it will also respond to radiation that deposits only a small amount of energy in the detector. Finally it should be noted that since very fast signals are produced high bandwidth ADC will be required.

Appendix A

Compendium of results of the complementary

ESR spectra of types Ib, IIa natural and synthetic diamonds

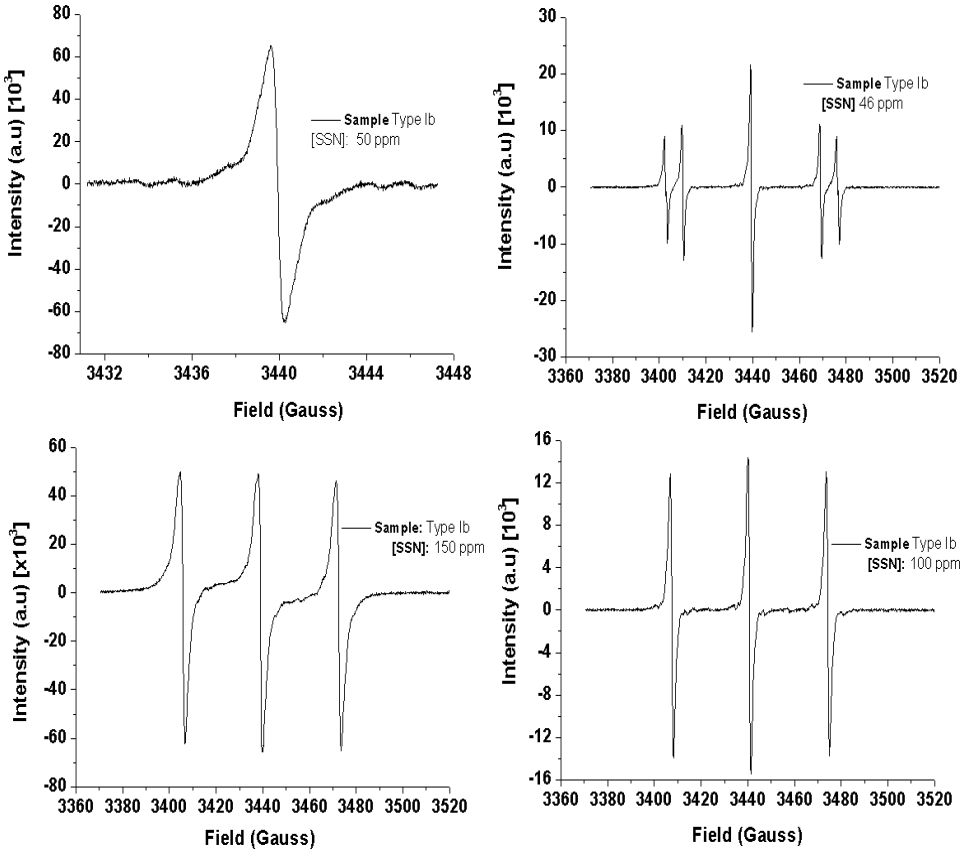

Figure A.1: ESR spectra of various type Ib diamonds used in this work.

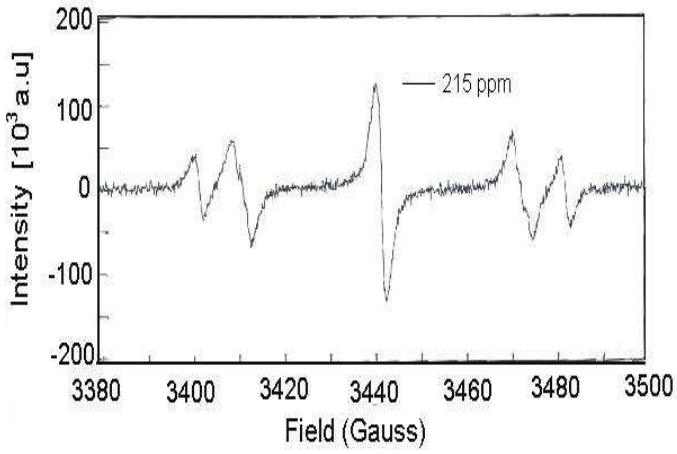

Figure A.2: ESR spectrum of type Ib synthetic diamond.

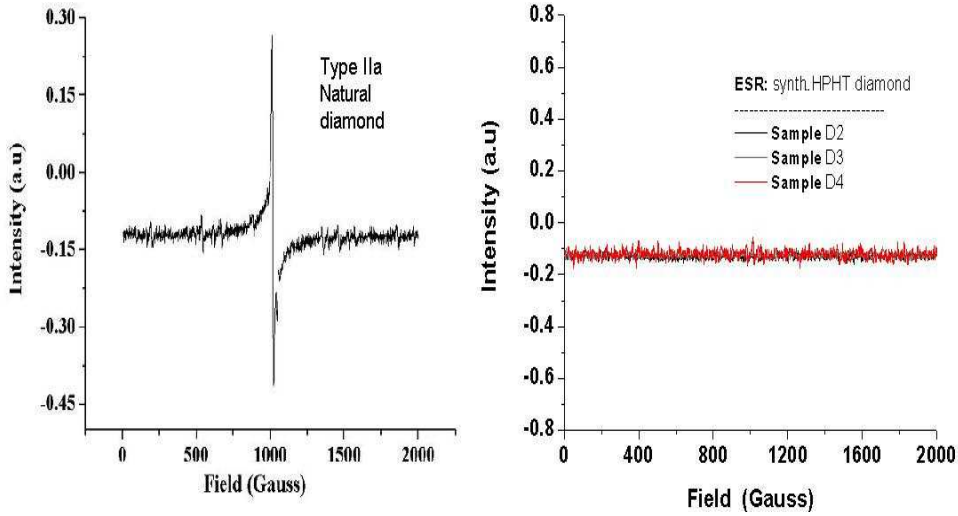

Figure A.3: Normal ESR spectra of type IIa natural diamond and synthetic type IIa HPHT diamonds.

IR spectra of type IIa synthetic diamond

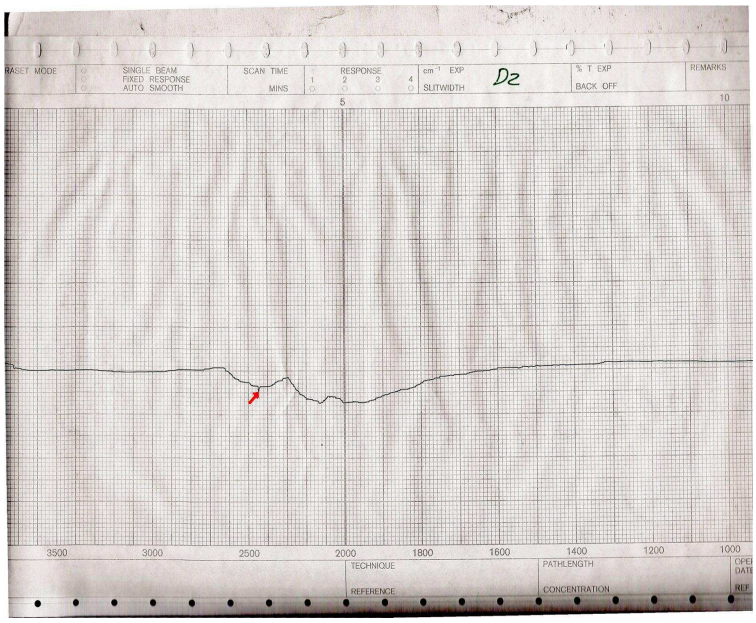

Figure A.4: Infrared spectra of a synthetic type IIa HPHT diamond, sample D2. The red arrow shows the position of an energy level corresponding to 0.305 eV. The technique is not sensitive to low concentrations of B acceptors impurity.

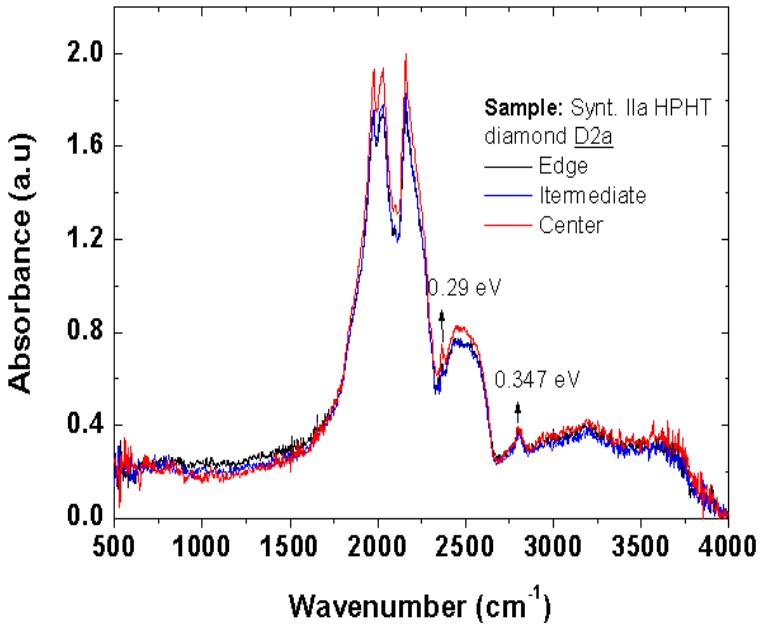

Figure A.5: Infrared spectra of three regions of synthetic type IIa HPHT diamond, sample D2a, after experiments with UV-laser.

Raman spectra of type IIa synthetic diamonds

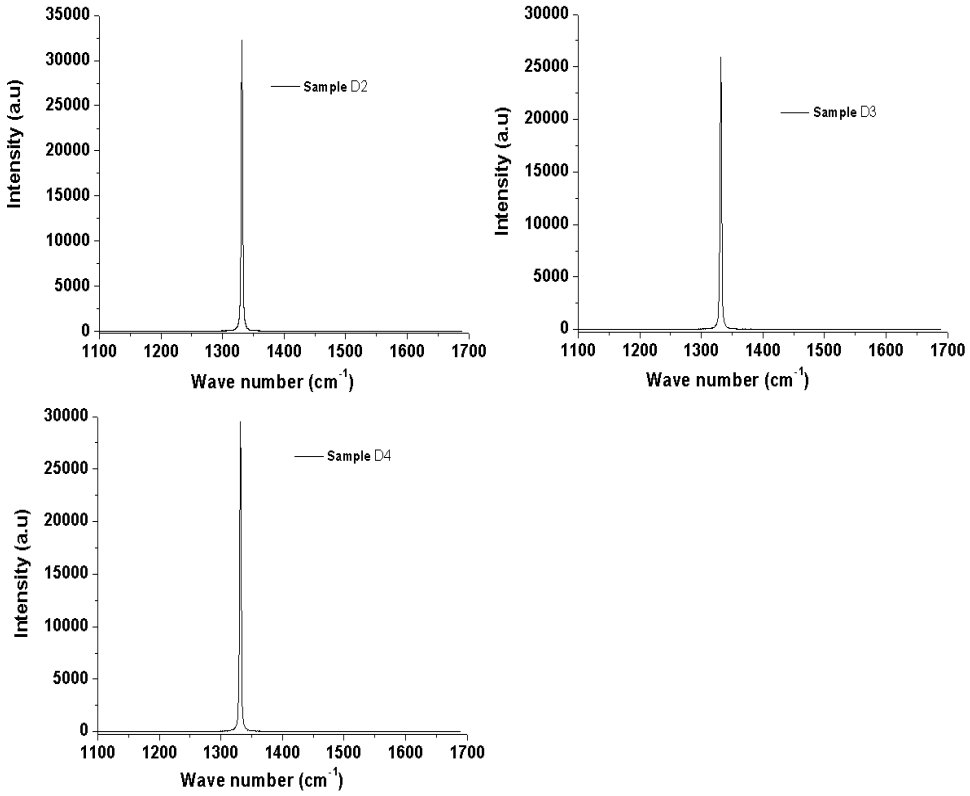

Figure A.6: Raman spectra of the three high purity synthetic type IIa HPHT diamonds.

Sample D2a with metallic contacts for I-DLTS measurements

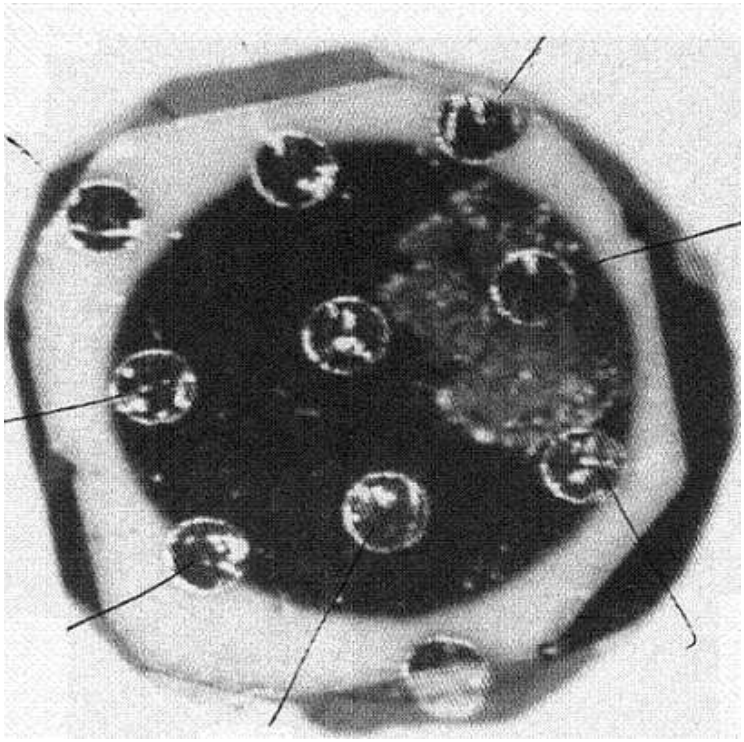

Figure A.7: Metallization on the sample D2a, for IV-characteristics and DLTS measurements.

Routine program used in analusis of I-DLTS results

```
k=8.62e-5
q=1.6e-19
h=6.63e-34
T=200K
Effective masses of holes in Diamond
; mhh=2.1*9.1095e-31     hh-> heavy holes      for thermal velocity at 100K
; mlh=0.7*9.1095e-31     lh-> light holes      g  ...2.3* at 100 K
;mso=1.06*9.1095e-31     so-> spin orbit
;mso=1.46e-30
;mef=1.39e-30      ; Diamond H(lh,hh)          On the total efective mass for diamond,
                                               the spin orbit is not taken into account.

pi=3.1416
l=15

vth_T=sqrt(8*k*q/pi/me1*T)                  ;  =sqrt(8*k*q/x)   ; m s^-1,   T
Nc_T=2*(2*pi*me*k*q/h^2)^1.5
prefactor=vth_T*Nc_T/10000/6                ; /cm,  T,   /6 for degeneracy
cell(2,12)=prefactor

for m=0 to 16 do
    T=col(10*m+3)
    col(10*m+4)=1000/T
    for i=1 to 3 do
       e(i)=col(10*m+3+2*i)
       col(10*m+4+2*i)=log(T^2/e(i))
    end for
;
for j=1 to 3 do
    cell(10*m+2,13)=prefactor
    E(j)=2303*k*cell(10*m+2,l+1+6*(j-1))
    cell(10*m+2,l+2+6*(j-1))=E(j)
    slope(j)=1/10^cell(m*10+2,l+6*(j-1))
    cell(10*m+2,l+3+6*(j-1))=slope(j)
    cell(10*m+2,l+4+6*(j-1))=slope(j)/prefactor     ;prefactor  ; capture cross section;
;cell(m,13)=prefactor/3.14e21
end for
cell(10*m+1,11)=vth_T*sqrt(T)*100
end for

;for ii=1 to 10 do
;cell(17,ii)=1000/(100+ii*20)
;cell(18,ii)=6
;end for
; 3.14e21
Originaly from Vladimir  (Modifyied in this work for Diamond)
```

Figure A.8: Routine used in Σ-plot to determine the activation energies and the capture cross-sections from Arrhenius plot .

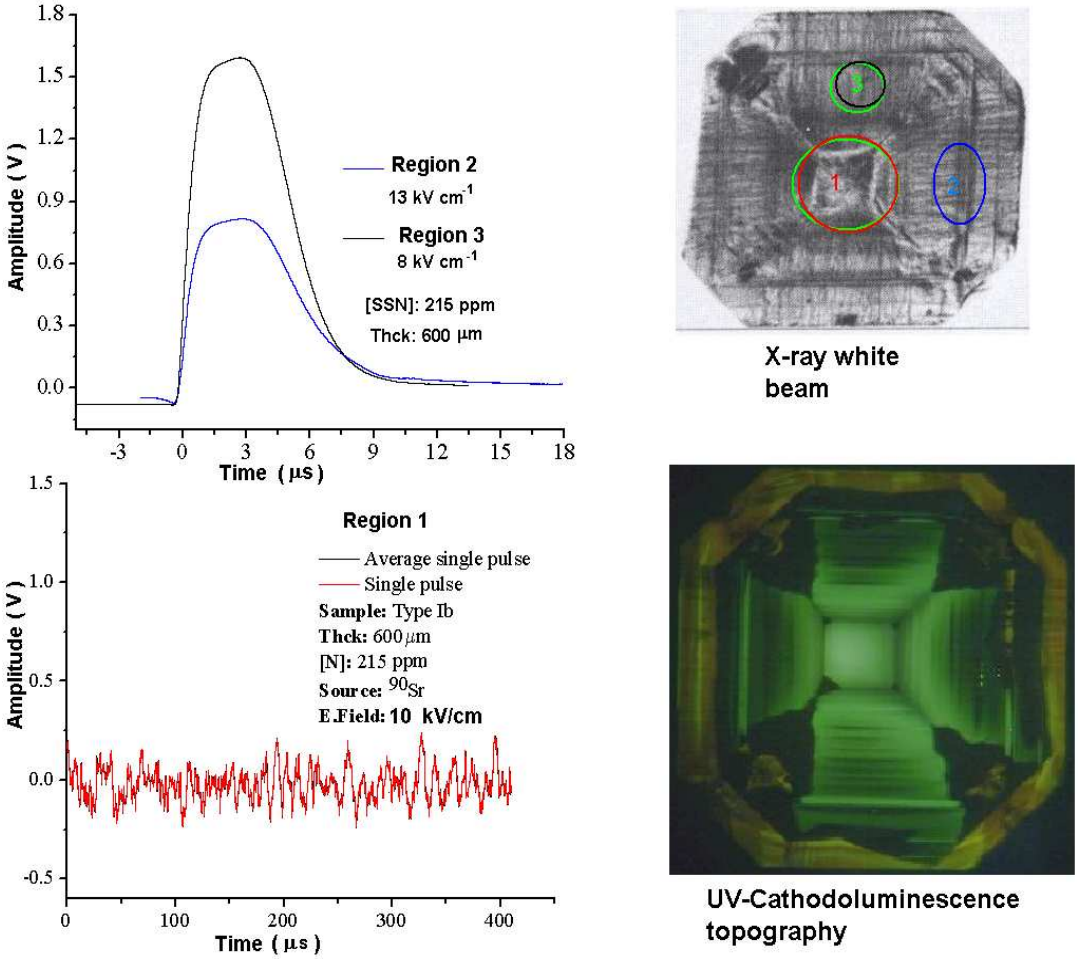

Figure A.9: Signal charge as a function of defects in three regions of a type Ib with 215 ppm of SSN.

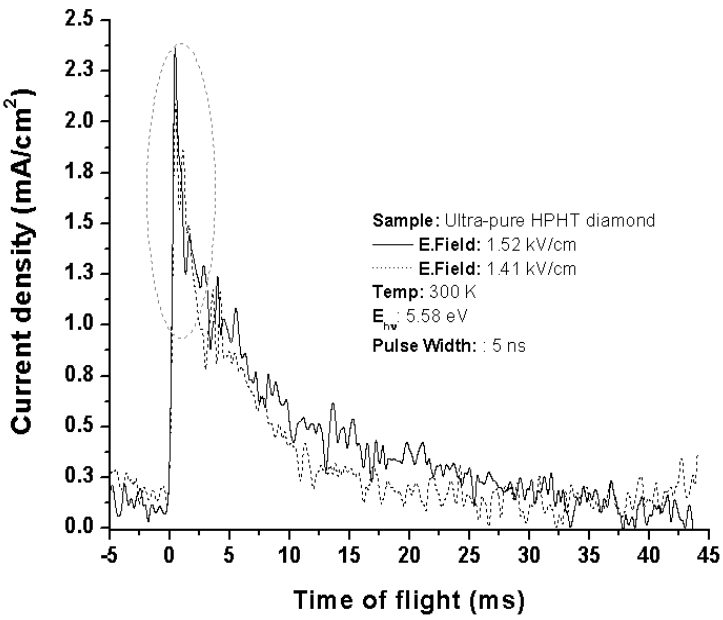

Figure A.10: TOF full signal as a function of applied external electric-field, at room temperature with contacts made of Ru-diamond-Ti/Pt/Au.

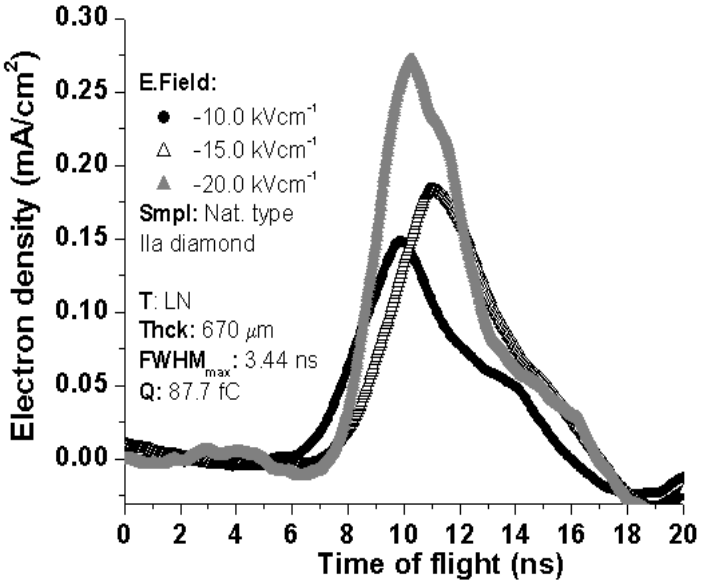

Figure A.11: Photocurrent signal generated by 5.6 eV photons in natural type IIa diamond, at negative applied external electric fields, at LN temperature with contacts made of Ru-diamond-Ti/Pt/Au. The signal was inverted to allow clearer analysis.

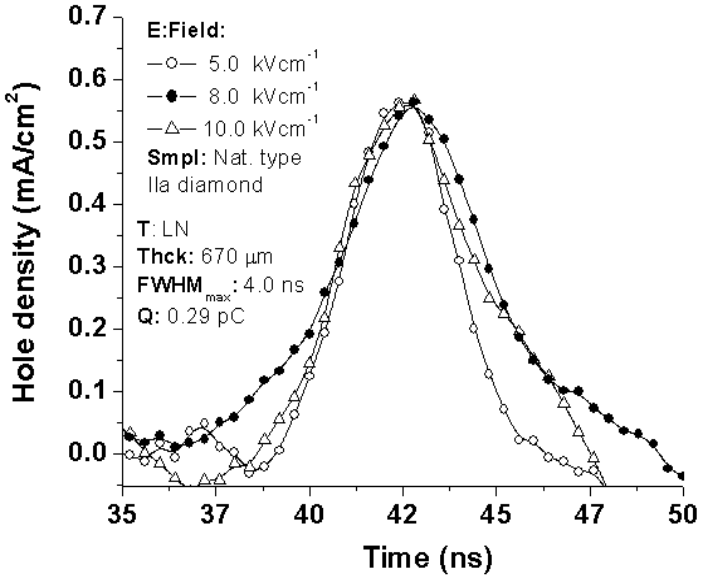

Figure A.12: Photocurrent signal generated by 5.6 eV photons in detector made with natural type IIa diamond, at positive applied external electric-fields, at LN temperature with contacts made of Ru-diamond-Ti/Pt/Au.

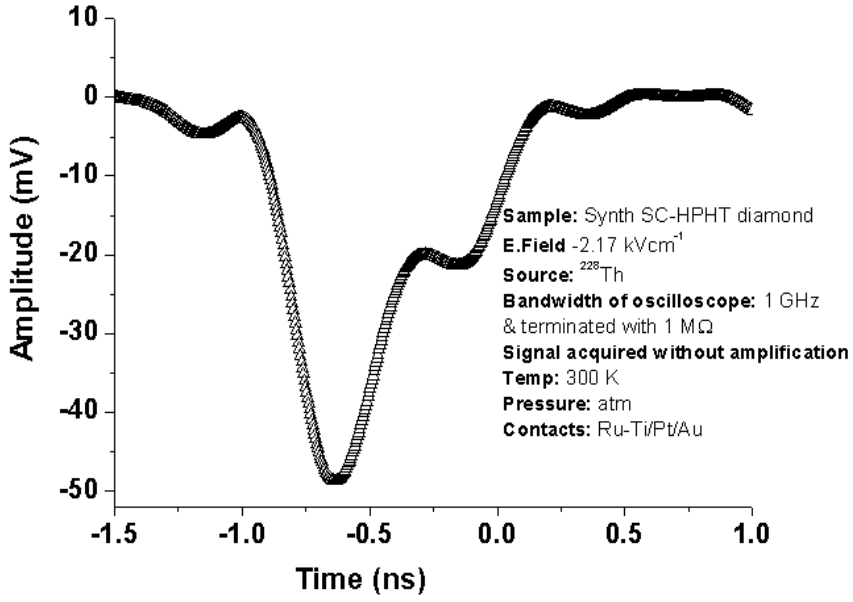

Figure A.13: Signal generated by α-particles, in type IIa HPHT synthetic diamond, with contacts made of Ti/Pt/Au-Ru. The thickness of the crystal was 460 μm and the geometrical capacitance of the detector was 0.54 pF. The RC constant of the detector is 27.00 ps. The rise and the decay times fall outside the bandwidth of the oscilloscope available in the laboratory.

Bibliography

[1] A. M. Zaitsev, *Optical Properties of Diamond*, A Data Handbook, ©Springer-Verag 2001.

[2] J. P. F. Sellschop *et al.*, *Synchrotron X-ray Applications of Synthetic Diamonds*, New Diamond Frontier Carbon Technology, Vol. 10, No. 5 2000, MYU Tokyo.

[3] J. E. Field, *The Properties of Diamond*, University of Cambridge, ©1979 by Academic Press Inc (London).

[4] J. E. Field, *The Properties of Natural and Synthetic Diamond*, University of Cambridge, Second edition 1992. U.K.

[5] A. Rossani, *Generalized kinetic theory of electrons and phonons: models equilibrium and stability*, Physica B 334 (2003) 292-297.

[6] D. Meier, *CVD Diamond Sensors for Particle Detection and Tracking*, Thesis dissertation, CERN, Geneva, January 1999. http://atlasinfo.cern.ch/Atlas/documentation/thesis/thesis.html.

[7] T. Sharda, *Studies of defects and impurities in diamond thin films*, Diamond and Rel. Mat. 7 (1998) 250.

[8] E. Rohrer *et al.*, *Nitrogen-related dopant and defect states in CVD diamond*, Phy. Rev. B, Vol. 54 No 11, 15 September 1996.

[9] R.J.Tapper, *Diamond detector in particle physics*, Rep.Pro.Phys.**63** (2000), pp1273, UK.

[10] K. E. Spear and J.P.Dismukes, *Synthetic Diamond Emerging CVD Science and Technology*, A Wiley-Interscience Publication by John Wiley and Sons, Inc. New York, Canada 1994.

[11] W. Adams *et al.*, *Review of the development of diamond radiation sensors*, Nucl. Inst. Meth. Phys. Res., A 434 (1999) 131-145.

[12] H. M. Strong and R. M. Chrenko, *Diamond growth rates and physical properties of laboratory-made diamond*, J.Phys.Phys.Chem vol 75., iss. 12, 1971, pp1838.

[13] R. Wedenig *et al.*, *CVD Diamond pixel detectors for LHC experiments*, Nucl. Phys. B (proc. Suppl.) 78 (1999) 497-504.

[14] J. Isberg *et al.*, *High Carrier Mobility in Single Crystal plasma-Deposited Diamond*, Reports, 6 September 2002 Vol 297, Science, www.sciencemag.org.

[15] M. Kasu, N. Kobayashi, *High mobility and high crystalline-quality chemical vapour deposition grown homoepitaxial diamond*, Diamond and Relat. Mater. 12 (2003) 413.

[16] J. H. Kaneko *et al.*, *Radiation detector made of a diamond single crystal grown by a chemical vapor deposition method*, Nucl. Inst. Meth. Phys. Res. A 505 (2003) 187-190.

[17] A. T. Collins, *The Fermi level in diamond*, J.Phys.: Condens. Matter 14(2002)3743.

[18] H. Speiler, *Radiation Detector and Signal Processing*, 8-Oct. 12, 2001, Univ. Heidelberg.

[19] T. Tanaka *et al.*, *Diamond radiation detector made of an ultrahigh-purity type IIa diamond crystals grown by high pressure and high-temperature synthesis*, Review of scientific Instruments, vol. 72, number 2, Feb 2001.

[20] Y. Tanimura *et al.*, *High-temperature operation of a radiation detector made of a type IIa diamond single crystal synthesized by a HP/HT method*, Nucl. Instr. Meth. Phys. Res. A 443 (2000) 325.

[21] C. Kittel, *Introduction to Solid State Physics*, Whiley, 1976.

[22] R. Dalven, *Introduction to Applied Solid State Physics*, Second Edition,1990, Plenum press, New York, US.

[23] G. Calzarferri and R. Rytz, *The band Structure of Diamond*, J. Phys. Chem. 1996, vol. 100, pp 11122.

[24] C. D Clark, P. J. Dean and P. V. Harris, *Intrinsic edge absorption in diamond*, Proceedings of Royal Society of London, Series A, Mathematical and physical sciences, vol 277, N0 1370, pp. 312., Feb. 1964.

[25] J. B. Sokoloff *et al.*, *Electron localization in crystals with quasiperiodic lattice potentials*. Phys. Rev. B, Vol 22 No 12, 15 December 1980.

[26] L. Reggiani *et al.*, *Hole drift velocity in natural diamond*, Phys. Rev. B 23, 3050 (1981).

[27] J. Callaway, *Quantum Theory of the Solid State*, Part A, 1974, Academic press, Inc, London UK.

[28] K. C. Kao and W. Hwang, *Electrical transport in solids*, Pergamon press, First edition, London 1981.

[29] J. D. Jackson, *Classical Electrodynamics*, second edition, Wiley, New York, 1975.

[30] S. M. Sze, *Physics of semiconductor Devices*, 2nd Edition by Wiley-Interscience Publication 1981 by John Wiley & Sons, Inc. USA.

[31] C. E. Nebel *et al.*, *Electronic properties of CVD and synthetic diamond*, Phys. Rev. B Vol. 55, No 15, 15 April 1997.

[32] C. E. Nebel *et al.*, *Carrier trapping and release in CVD-Diamond films*, Diamond and Rel. Mat., 7 (1998) 556.

[33] F. D. Auret and P. N. K. Deenapanray, *Deep Level Transient Spectroscopy of Defects in High-Energy Light-Particles Irradiated Si*, Critical Reviews in Solid State and Materials Science, 29:1-44, 2004, ©Taylor & Francis Inc, ISSN:1040-8436 print, DOI:10.1080/10408430490442458.

[34] M. Hasegawa *et al.*, *Characterisation of nitrogen-implanted CVD homoepitaxial diamond*, Diamond and Rel. Mat. 13(2004)600.

[35] D. R. Frankl, *Electrical Properties of Semiconductor Surface*, Pergamon Press Ltd, London, First edition 1967.

[36] H. Kim *et al.*, *Magnetospectroscopy of acceptors in "blue" diamonds*, Phys B, Physica B 302-303(2001) 88.

[37] K. Thonke, *The boron acceptor in diamond*, Semicond. Sci. Technol. 18(2003)S20-S26.

[38] T. Inushima *et al.*, *Hopping conduction via the excited states of boron in p-type diamond*, Diamond and Rel. Mat. 9 (2000) 1066.

[70] B. Massarani, J. C. Bourgoin and R. M. Chrenko, *Hopping conduction in semiconducting diamond*, Phys. Rev. B, vol. 17, N0 4, pp1758, Feb. 1978.

[40] M.H. Nazaré and A.J. Neves, *Properties, Growth and Applications of Diamond*, EMIS, Date Reviews Series, n0 26 p40, INSPEC Publication, 2001.

[41] V. I. Polyakov *et al.*, *Electrical properties of thick boron and nitrogen contained CVD diamond films*, Diamond and Rel. Mat. 10 (2001) 593.

[42] R. A. Smith, *Semiconductors*, Cambridge: Cambridge University Press, 1961.

[43] A. T. Collins, *The attraction and limitations of semiconducting diamond for electronic device applications*, S. Afr. J. Phys. 16 No.1/2 (1993).

[44] E. Segrè, *Nuclei and particles*, University of California, Second edition, 1977.

[45] S.P Ahlen, *Theoretical and experimental aspects of energy loss of relativistic*

heavely ionizing particles, Reviews of Modern Physics, Vol. 52, N0. 1, January 1980.

[46] M. K Sundaresan, *Handbook of Particle Physics*, CRC Series in Pure and Applied Physics, CRC Press, U.S 2001

[47] K. Kleinknecht, *Detectors for particle radiation*, University of Cambridge, University press 1986, English edition.

[48] E. Vittone *et al.*, *Theory of ion beam induced charge collection in detectors based on the extended Schokley-Ramo theorem*, Nucl. Inst. Meth. Phys. Res. B 161-163 (2000) 446-451.

[49] G. Cavalleri *et al.*, *Extension to Ramo's Theorem as applied to induced charge in semiconductor detectors*, Nucl. Inst. Meth. Phys. Res, 92 (1971) 137.

[50] Z. He, *Review of the Shockley-Ramo theorem its application in semiconductor gamma-ray detectors*, Nucl. Inst. Meth. Phys. Res. A 463 (2001) 250.

[51] M. Werner, *Diamond metallization for device applications*, Semicond. Sci. Thechnol. 18 (2003) S41.

[52] C. A. Mead and W. G. Spitzer, *Fermi-Level at Metal-Semiconductor Interfaces*, Phys. Rev. 134, A713, Issue 3A, May 1964.

[53] M. Craucin *et al.*, *A 3.4 eV Potential barrier height in Schottky diodes on boron-doped diamond thins films*, Diamond and Rel. Mat. 13 (2004) 292.

[54] J. Shirafuji and T. Sugino, *Electrical properties of diamond surfaces*, Diamond and Rel. Mat. 5 (1996) 706.

[55] J. Ihm, S. G. Louie. and M. L. Cohen, *Diamond Metal Interfaces and the Theory of Schottky Barriers*, Phys. Rev. Lett, Vol. 40, No.18, 1 May 1978.

[56] L. S. Pan and D. R. Kania, *Diamond: Electronic Properties and Applications*, Kluwer Academic Publisher,1995,USA.

[57] P. N. Murgatroyd, *Theory of space-charge-limit current enhanced by Frankel effect*, J. Phys.D, Appl. Phys. 3, pg.151, Iss.2 1970.

[58] A. Mainwood, *CVD diamond particle detector*, Diamond and Rel. Mat. 7 (1998) 504-505.

[59] R. C. Alig *et al.*, *Scattering by ionization and phonon emission in semiconductors*, Phys. Rev. B, Vol 22, No 12, 15 December 1980.

[60] C. Canali *et al.*, *Electrical properties and performance of natural diamond nuclear radiation detector*, Ncl. Inst. Meth. Phys. Res. **160** (1979) pp73.

[61] S. Salvatori, M. C. Rossi and F. Galuzzi, *Minority-carrier transport parameters in CVD diamond*, Carbon, **37**(1999) 811.

[62] R. T. Mainardi, T. S. Plivelic and P. A. Derosa, *Assessment of pulse height selection methods for several spectrum shapes in radiation detection*, Nucl. Instr. Meth. Phys. Res. B 201 (2003) 525.

[63] S. Salvatori *et al.*, *Transient photoresponse of a CVD diamond-based detectors in a time domain* $10^{-9} - 10^{3}s$, Diamond and Rel. Mat. 8(1999)871.

[64] J. P. F. Sellschop *et al.*, *Diamond Film, Electrical Properties*, Encyclopedia of

Physical Science and Technology, Third edition, vol. 4, Academic Press of the University of the Witwatersrand, 2002, SA.

[65] R. D. McKeag *et al.*, *Photoconductive properties of thin film diamond*, Diamond and Rel. Mat. 6 (1997) 374.

[66] M. Dudley *et al.*, *White-Beam synchrotron topography studies of defects in 6H-SiC single crystal*, J. Phys. D. Appl. Phys. 28 (1995) A63.

[67] R. D. Black and G. G. Long, *X-ray Topography-NIST Recommended practice guide*, Nat. Inst. Stand. Technol., Spec. Publ. 960-10., April 2004.

[68] R. H. Telling *et al.*, *Theoretical Strength and Cleavage of Diamond*, Phys. Rev. Lett, Volume 84, Number 22, 29 May 2000.

[69] E. Friedland and J. P. F. Sellschop, *Temperature dependence of critical damage energies in diamond*, Nucl. Instr. Meth Phys. Res. B 191 (2002) 17.

[70] B. Massarani, J.C. Bourgois and R.M Chrenko, *Hopping conduction in semicnducting diamond*, Phys. Rev. B., vol. 17, N0 4, 1978.

[71] J. F. Prins, *Preparation of ohmic contacts to semiconducting diamond*, Phys.D: Appl. Phys. 22 (1989) 1562. Printed in UK.

[72] N. W. Makaw and T. E. Derry, *Study of oxygen on the three low index surfaces by XPS*, Surface Review and Letters, Vol. 10, Nos. 2 and 3 (2003) 295.

[73] T. Tachibana and J. T. Glass, *Correlation of interface chemistry to electrical properties of metal contacts on diamond*, Diamond and Rel. Mat. 2(1993) 963.

[74] M. P. Seach, *Quantification of AES and XPS*, Edited by D. Briggs and M. P. Seach, ©1983, John Wiley & Sons, Ltd.

[75] Y. Kawabata *et al.*, *XPS studies on damage evaluation of single-crystal diamond chips processed with ion beam etching and reactive ion beam assisted chemical etching*, Diamond and Rel. Mat. 13(2004)93.

[76] M. Yoshikawa *et al.*, *Characterization of crystalline quality of diamond films by Raman spectroscopy*, Appl. Phys. Lett., vol 55(25). 18 December 1989.

[77] M.Mermox *et al.*, *Raman characterization of boron-doped {111} homoepitaxial diamond layers*, Article in press, Diamond and Rel. Mat. xx(2005)xxx-xxx.

[78] D. Wu *et al.*, *Optical properties of boron-doped diamond*, Phys. Rev. B 73, 012501 (2006).

[79] N. Teofilov *et al.*, *Optical high excitation of diamond: phase diagram of excitons, electron-hole liquid and electron-hole plasma*, Diamond Rel. Mat. 12 (2003) 636.

[80] S. J. Sharp *et al.*, *Higher resolution of shallow bound exciton luminescence in diamond*, J. Phys.: Condens. Matter 9 (1997) L451.

[81] A. Wotherspoon *et al.*, *Photoluminescence studies of type IIa and nitrogen doped CVD diamond*, Diamond and Relat. Mater. 11 (2002) 692.

[82] K. Lakoubovskii *et al.*, *Characterisation of defects in monocrystalline CVD diamond film by electron spin resonance*, Diamond and Rel. Mat. 12 (2003) 511.

[83] A. Abragam and B. Bleaney, *Electron Paramagnetic Resonance of Transition Ions*, Dover Publications, Inc, 1986, New York, ISBN 0-4865106-1.

[84] J. A. Van Wyk *et al.*, *The dependence of ESR line widths and spin-spin relaxation times of single nitrogen defects on the concentration of nitrogen defects in diamond*, J. Phys. D: Appl. Phys., 30 (1997)1790.

[85] E. C. Reynhardt, G. L. High and J. A. Van Wyk, *Temperature dependence of spin-spin and spin-lattice relaxation times of paramagnetic nitrogen defects in diamond*, J. Chem. Phys., Vol 109, No. 19., 1998.

[86] G. Myburg and F. D. Auret, *Influence of electron beam evaporation rate of Pt and the semiconductor carrier density on the characteristics of Pt/n-GaAs Schottky contacts*, J. Appl. Phys, 71(12), 15 June 1992.

[87] F. D. Auret, *Comparison between defects introduced during electron beam evaporation of Pt and Ti on n-GaAs*, Material Science Forum vol. 83-87 (1992)pp.1499.

[88] T. Tanaka *et al.*, *Diamond radiation detector made of an ultra-purity type IIa diamond crystal grown by high-pressure and hih-temperature synthesis*, Rev. Sci. Instrum., vol 72, No. 2, February 2001.

[89] S.Mathur and P.Kuhn, *CVD of titanium oxide coatings: Comparative evaluation of thermal and plasma assisted processes*, Surf. Coat. Technol. 201 (2006) 807.

[90] T. Teraji emphet al., *Ohmic contacts for phosphorous doped diamond*, phys. Stat. Sol. (a) 181, 129 (2000).

[91] J. F. Prins, *Ion implantation of diamond for electronic applications*, Semicond. Sci. Technol. 18 (2003) S27.

[92] A. Alexov, *Diamond diodes and transistors*, Semicond. Sci. Technol. 18 (2003) S59.

[93] D. Takeuchi *et al.*, *Schottky junction properties of high conductivity layer of diamond*, Diamond and Rel. Mat. 11 (2002) 355.

[94] F. Borchelt *et al.*, *First measurement with a diamond microstrip detector*, Nucl. Instr. and Meth. in Phys. Res. A 345 (1995) 318.

[95] O. A. Williams and R. B. Jackman, *Surface conductivity on hydrogen terminated diamond*, Semicond. Sci. Technol. 18 (2003) S34.

[96] C. Uzan-Saguy *et al.*, *Diffusion of hydrogen from a microwave plasma into diamond and its interaction with dopants and defects*, Diamond and Rel. Mat. 11 (2002) 316.

[97] Y. Dai *et al.*, *The role of dangling-bond, hydrogen and adsorbate in diamond surface conduction*, Diamond and Rel. Mat., 12 (2003) 15-19.

[98] J. Chevallier *et al.*, *Hydrogen in n-type diamond*, Diamond Rel. Mat. 11 (2002) 1566.

[99] J. E. Butler *et al.*, *Exceptionally high voltage Schottky diamond diodes and low boron doping*, Semicond. Sci. Technol. 18 (2003) S67.

[100] R. Zeisel *et al.*, *Deep level transient spectroscopy of synthetic IIb diamond*, J. Appl. Phys. Vol. 84, No 11, 1 December 1998.

[101] M. E. Mora-Ramos *et al.*, *Hole state in boron delta-doped diamond*, Diamond and Rel. Mat. 12 (2003) 33.

[102] I. Turzo *et al.*, *Charge deep-level transient spectroscopy of Al/intrisinc diamond/ p^+ -Si Schottky diodes*, Semicond. Sci. Technol. 16 (2001) 527.

[103] D. V. Lang and L. C. Kimerling *et al.*, *Observation of Recombination-Enhanced Defect Reactions in Semiconductors*, Phys. Rev. Lett, Vol. 33, No 8, 19 August 1974.

[104] F. D. Auret and M. Nel, *Single scan defect identification by deep level transient spectroscopy using a two-phase lock in amplifier (IQ-DLTS)*, J.Appl. Phys. 63(3), 1 February 1988.

[105] D. K. Schroder, *Semiconductor Material and Device Characterization*, pp320 Second edition, Wiley-Interscience, 1998 U.S.A.

[106] A. Balduci *et al.*, *Extreme UV single crystal diamond photodetectors by chemical vapour deposition*, Diamond and Rel. Mat. 14 (2005)1980-1983.

[107] E. Vittone *et al.*, *Imaging of charge collection properties of a CVD diamond detector using X-ray-induced current microscopy*, Diamond Rel. Mat. 11 (2002) 1472.

[108] H. N. Alshareef *et al.*, *Temperature dependence of the work function of ruthenium-based gate electrodes*, Thin Solid Films 515 (2006) 1294.

[109] E-K. Souw, *Response of CVD diamond detectors to alpha radiation*, Nucl. Instr. Meth. Phys. Res. A 400 (1997) 69.

[110] Y. Y. Lau, *Simple Theory for the Two-Dimensional Child-Langmuir Law*, Phys. Rev. Lett, Vol. 87, No 27, 31 December 2001.

[111] X. Chen *et al.*, *Approximate analytical solution for the space-charge-limited current in one-dimensional and two-dimensional cylindrical diodes*, Physics of Plasmas, Vol. 11, No 6, June 2004. 3.

[112] A. BenMoussa, *et al.*, *Performance of diamond detector for VUV applications*, Nuclear Instruments and Methods in Physics Research A 568 (2006) 398.

[113] C. Tuv *et al.*, *Carrier dynamics in CVD diamond: electron and hole contributions*, Diamond Rel. Mat. 12 (2003) 499.

[114] P. J. Fallon, *Trapping levels in pulse-counting synthetic diamond detectors*, Diamond and Rel. Mat. 1 (1992) 1182.

[115] A. Balduci *et al.*, *Recent IBIC measurement on epitaxial CVD diamond*, Diamond and Rel. Mat. 14 (2005)1988.

[116] H. Amekura *et al.*, *Internal Electric Field Formation in insulators under High-Flux Negative-Ion Implantation*, Jpn. J. Appl. Phys. Vol. 40 (2001) p. 1091, Part 1, N0. 2B, February 2001.

[117] R. J. Keddy and T. L. Nam, *Diamond Radiation Detector.*, Radiat. Phys. Chem. Vol. 41, N0. 4/5, pp. 767, 1993.

[118] S. G. Wang *et al.*, *Diamond-based alpha particle detectors with coplanar geometry*, Diamond Relat. Mater. 12 (2003) 682.

[119] F. Foulon *et al.*, *Photodetecteurs ultra-rapides pour la metrologie d'impulsions*, UV-X, J. Phys. IV France 9 (1999).

[120] P. Moritz *et al.*, *Broadband electronics for CVD-diamond detectors*. Diamond Rel. Mat. 10(2001)1765.

[121] G. Caragheopol, M. Petris and M. Petrovici, *CVD-Diamond Detectors for MIP's: characterisation and processing electronics*, National Institute of Physics and Nuclear Engineering-Romenia.